A precision test of Lorentz Invariance using room-temperature high-finesse optical resonators

Inaugural-Dissertation

zur Erlangung des Doktorgrades
der Mathematisch-Naturwissenschaftlichen Fakultät
der Heinrich-Heine-Universität Düsseldorf

vorgelegt von

Christian Eisele
aus Freiburg im Breisgau

Düsseldorf, November 2009

Aus dem Institut für Experimentalphysik
der Heinrich-Heine-Universität Düsseldorf

Gedruckt mit Genehmigung der
Mathematisch-Naturwissenschaftlichen Fakultät der
Heinrich-Heine-Universität Düsseldorf

Referent: Prof. S. Schiller

Koreferent: Prof. A. Görlitz

Tag der mündlichen Prüfung: 28.10.2009

Im Andenken an meinen Großvater
†18.08.2006

Zusammenfassung

Im Zuge der vorliegenden Arbeit wurde eine Apparatur für die Überprüfung einer Grundaussage der Speziellen Relativitätstheorie, der Isotropie der Lichtgeschwindigkeit, entwickelt. Abweichungen von der Isotropie bedeuten eine Verletzung der Lorentz Invarianz, eine von allen etablierten Theorien der Grundkräfte angenommenen Symmetrie, und würden auf Physik jenseits der derzeit gültigen Theorien, der Allgemeinen Relativitätstheorie und des Standardmodells der Teilchenphysik, hindeuten.
Theoretiker versuchen seit langem alle Naturkräfte in einer einheitlichen Theorie zu vereinigen, was bisher trotz vielversprechender Ansätze (String-Theorien, loop quantum gravity, et cetera) nicht vollständig gelungen ist. Allerdings gibt es Hinweise darauf, dass die Invarianz unter Lorentz-Transformationen keine exakte Symmetrie darstellen sollte und geringfügige Abweichungen zu erwarten sind. Dies stellt eine starke Motivation für hochpräzise Tests der Lorentz-Invarianz dar, wie den in dieser Arbeit präsentierten.

Erstmalig werden in diesem Aufbau monolithische optische Resonatoren aus einer Glaskeramik mit extrem niedrigem thermischen Ausdehnungskoeffizienten (ULE) verwendet, um die Isotropie zu testen. Mit Hilfe eines monolitischen Nd:YAG Lasers ($\lambda = 1064nm$) werden die Resonanzfrequenzen von zwei orthogonal orientierten Resonatoren abgefragt und miteinander verglichen. Der niedrige thermische Ausdehnungskoeffizient reduziert den Einfluss von Temperaturschwankungen auf die Resonanzfrequenzen, die nur vom Abstand der Spiegel und der Geschwindigkeit des Lichts in den Resonatoren abhängen.
Um eine möglichst hohe Stabilität der Resonanzfrequenzen auf kurzen Zeitskalen zu erreichen wurde der gesamte optische Aufbau auf einer aktiven Vibrationsisolierung gelagert, die mechanische Vibrationen stark dämpft. Diese Technik wird erstmalig in einem Experiment zum Test der Isotropie der Lichtgeschwindigkeit eingesetzt. Desweiteren wurde eine auf elektromagnetischen Aktuatoren basierende Stabilisierung der Neigung der Trägerplatte implementiert. Diese ist nötig, da eine Neigung der Resonatoren gegenüber der lokalen Richtung der Gravitation die Resonanzfrequenzen verschiebt.
Desweiteren wurden Regelsysteme für die Stabilisierung der in den Resonatoren umlaufenden Leistung und der Temperatur des Aufbaus implementiert. Der gesamte Aufbau kann mit Hilfe eines luftgelagerten Rotationstisches aktiv rotiert werden. Dies ermöglicht eine deutlich erhöhte Datenaufnahmerate im Vergleich zu stationären Aufbauten, was zu einer raschen Reduktion statistischer Fehler führt. Desweiteren sinken die Anforderungen an die Langzeitstabilität des Systemes. Eine sehr hohe Frequenzstabilität ist auf der Zeitskala einer halben Rotation gefordert, was bei stationären Systemen hohe Stabilität über 12 Stunden, hier nur über 45 Sekunden erfordert.

Mit dem beschriebenen Aufbau wurden zwischen März 2008 und April 2009 wiederholt

Messungen durchgeführt, so dass insgesamt ca. 135 000 Rotationen verteilt über diese Zeit zur Analyse verwendet werden konnten. Diese Daten wurden im Rahmen von zwei verschiedenen Test-Theorien analysiert, der Robertson-Mansouri-Sexl Theorie (RMS) und der sogenannten Standard Model Extension (SME).
In der RMS Theorie beschreibt ein Parameter, $(\delta-\beta+1/2)$, eine mögliche Anisotropie. Wir konnten mit $(\delta - \beta + 1/2) \leq 8 \cdot 10^{-12}$ eine obere Grenze für diesen Parameter bestimmen, die mehr als eine Größenordnung unter den bisher besten Resultaten liegt und eine mögliche Anisotropie auf $\frac{1}{2}|\Delta c(\pi/2)/c| \leq 6 \cdot 10^{-18}$ einschränkt (1σ).
Im Rahmen der SME konnten mit dem hier vorgestellten Experiment acht Parameter der Theorie bestimmt werden, die Verletzungen der Lorentz-Invarianz für Photonen beschreiben. Obere Grenzen für diese Parameter konnten für alle Parameter gegenüber dem Vorgänger-Experiment und den Werten anderer Gruppen deutlich verbessert werden.Teile der Arbeit wurden bereits in Optics Communications veröffentlicht:
Ch. Eisele, M. Okhapkin, A. Yu. Nevsky and S. Schiller, Optics Communications **281**, 1189 (2008).
Die finalen Resultate der Arbeit wurden in Physical Review Letters publiziert:
Ch. Eisele, A. Yu. Nevsky, and S. Schiller, Physical Review Letters **103**, 090401 (2009).

Abstract

An apparatus for a test of a basic postulate of the theory of Special Relativity, the isotropy of the speed of light, has been developed. Deviations from the isotropy imply a violation of Lorentz invariance, a symmetry assumed by all established theories of the fundamental forces. Such a signal may provide a glimpse on physics beyond our current theories of the fundamental forces, the General Theory of Relativity and the Standard Modell of particle physics.
Since long theoreticians try to unify General Relativity and the Standard Modell within one theory, a grand unified theory (GUT). So far they did not succeed, although promising candidate theories have been developed, e.g. string theories or loop quantum gravity. However, there are hints that Lorentz invariance might not be an exact symmetry of nature, but that deviations are to be expected. This is a strong motivation for tests of Lorentz invariance with increased sensitivity as the one presented within this thesis.

We employ, for the first time for a test of the isotropy of the speed of light, monolithic optical resonators fabricated from a glass ceramic with ultra low expansion coefficient (ULE). By means of a monolithic Nd:YAG-laser ($\lambda = 1064$ nm) we measure the difference between the resonance frequencies of two orthogonally oriented resonators. The low thermal expansion coefficient reduces the influence of thermal fluctuations on the resonance frequencies, which are a function of the mirror spacing and the speed of light inside the resonators only. The complete optical setup has been put on top of active vibration isolation supports, which strongly damp mechanical vibrations. This improves the short-time stability of the resonators' resonance frequencies. This technique is used for the first time in a *Speed of Light Isotropy Test* (SLIT) experiment. Furthermore, a system for the stabilization of the tilt of the optics breadboard is implemented, based on electromagnetic actuators. This stabilization is necessary, since a tilt of the resonators with respect to the local direction of gravitation leads to a shift of the resonance frequencies.
Finally, servo systems have been implemented to stabilize the optical power circulating in the resonators and the temperature of the setup. The complete experiment can be actively rotated by means of an high precision air bearing rotation table, which allows for a considerable increase of the rate of data taking as compared to a stationary system. This allows for a comparatively fast reduction of statistical errors. Another advantage of the active rotation is the relaxation of stability demands for long timescales. A high frequency stability is needed on a timescale of half a rotation, here ≈ 45 s, while for stationary systems it would be 12 hours since one has to rely on the rotation of the earth.

With the setup just described we have performed measurements between march 2008 and may 2009 yielding ≈ 135000 rotations distributed over the entire timespan. This data was analyzed according to two different test theories, the Robertson-Mansouri-Sexl theory (RMS) and the Standard Modell extension (SME).

Within the RMS theory a single parameter combination $(\delta - \beta + 1/2)$ describes a possible anisotropy. For an isotropic speed of light it equals zero. We determined an upper limit of $(\delta - \beta + 1/2) \leq 8 \cdot 10^{-12}$ corresponding to a relative anisotropy of the speed of light below $\frac{1}{2}|\Delta c(\pi/2)/c| \leq 6 \cdot 10^{-18}$ (1σ bounds). This value is more than one order of magnitude smaller than the values published so far.
Within the framework of the SME we could determine 8 parameters describing a possible violation of the Lorentz invariance by photons. Upper limits for these parameters could be improved considerably compared to the experimental predecessor of the setup and to the values determined by other groups.
Parts of this thesis have already been published in Optics Communications:
Ch. Eisele, M. Okhapkin, A. Yu. Nevsky and S. Schiller, Optics Communications **281**, 1189 (2008).
The final results have been published in Physical Review Letters:
Ch. Eisele, A. Yu. Nevsky, and S. Schiller, Physical Review Letters **103**, 090401 (2009).

Contents

List of Figures

List of Tables

1. Introduction

More than 100 years have passed since the discovery of the theory of Special Relativity (TSR) during Einsteins *annus mirabilis* in 1905 [1]. Before its discovery physicists had to deal with contradictions between their main theories, namely Newtonian mechanics being invariant under Galilei transformations and the theory of electromagnetism developed by J.C. Maxwell being invariant under Lorentz transformations. It was expected that electromagnetic waves would propagate in a medium, the so called ether, which is at rest in a certain reference frame and thus defines a preferred system. However, the negative outcome of one of the most famous experiments in physics, the Michelson-Morley experiment [2], which was designed to prove the existence of an ether, raised serious doubts about the assumed fundamental structure of space and time.
Einstein solved these problems when he realized, that the transformation behaviour of Newtonian Mechanics, the invariance under Galilei transformations, is only an approximation for low velocities. Instead one has to use Lorentz transformations, under which Maxwell's theory of electrodynamics is invariant. Following these ideas he developed the theory of special relativity (TSR). Later he extended the ideas of the TSR and developed in 1914 the General Theory of Relativity (GTR) [3].

The theory of Special Relativity is built upon two main assumptions/postulates:

- The Einstein principle of relativity
- The universality of the speed of light

The principle of relativity states that all laws describing the change of physical states should not depend on which of two coordinate systems is used to describe the change of the physical state. All coordinate systems moving relatively towards each other with a constant velocity can be used. This means that every physical law should be invariant under the same group of transformations.
The universality of the speed of light states, that light propagates in every inertial system with the same velocity and that this velocity is independent of the state of motion of the emitting source. These two postulates are fulfilled if physical laws are invariant under the transformations discovered by Lorentz and Poincaré in 1904 [4, 5]. The symmetry implied by the theory of Special Relativity is therefore called Lorentz invariance.

Since the time of its development, TSR has withstood all tests and the invariance under Lorentz transformations has become one of the leitmotifs to be accounted for during

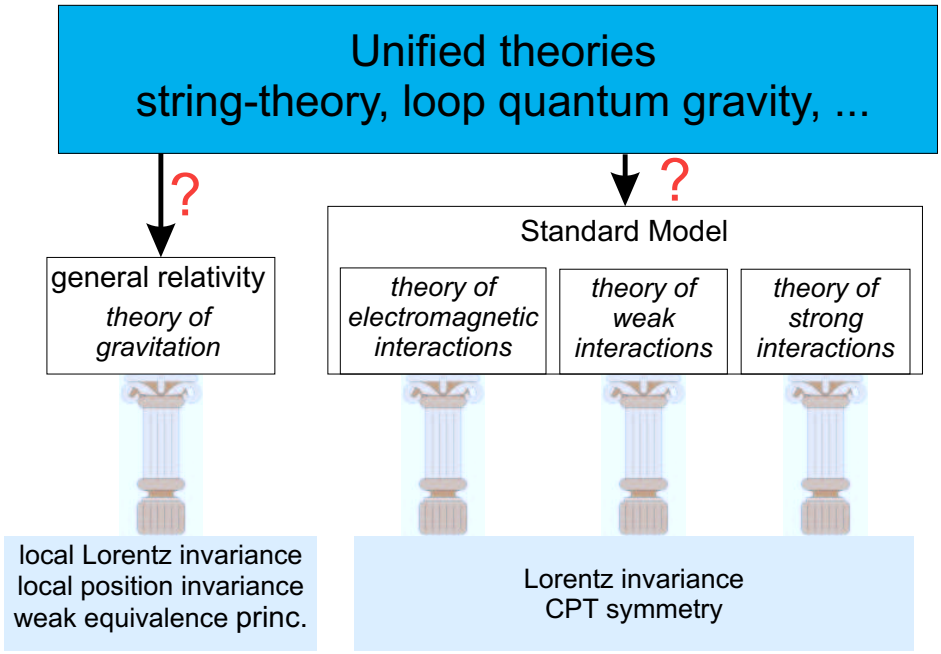

Figure 1.1.: *General Relativity, as well as the Standard Model, assume the validity of (local) Lorentz invariance. Both theories might be only limits of a more fundamental theory unifying all fundamental forces, which is not necessarily Lorentz invariant.*

the construction of new physical theories. The transformation behaviour implied by the TSR is one of the fundamental symmetries incorporated in all our established theories of the fundamental forces, be it as a local or a global symmetry.
This fundamental importance of Lorentz invariance alone is already a strong motivation for experimentalists to put it to the test with an ever increasing precision. Another reason is that theoretical physics is in a situation comparable to the situation at the end of the 19th century. Two different theories describe extremely successfully different parts of the physical reality (see fig. 1.1).

- The theory of General Relativity describes gravitational interactions and explains effects on large scales and at high energy densities, while it fails to give a quantum description of gravity.

- The Standard Model of particle physics on the other hand precisely describes the electromagnetic, weak and strong interactions down to the quantum level, but it is not possible to incorporate gravity into its formalism.

Therefore theoreticians are searching for a way to unify all the fundamental forces within one theory, a so called Grand Unified Theory (GUT). Several candidate theories have already been developed as e.g. string theories[1] [6], loop quantum gravity [7], and many more, but all of them are facing severe difficulties.
However, these developments over the last decades lead to the insight, that the invariance of physical laws under the Lorentz transformation might only be an approximate symmetry of nature, and that at extremely high energies comparable to the Planck mass $m_{Pl} = \sqrt{(\hbar c/G)}$ Lorentz invariance might be broken. In fact in the formalism of string theories some processes can lead to spontaneous breaking of the Lorentz symmetry although the general dynamics of the theory stays Lorentz invariant [8].
These deviations are strongly suppressed in our low energy world, but still they may be detectable in high precision measurements. This hypothesis stimulated new work in the field of tests of the Theory of Special Relativity and of other fundamental symmetries like Local Position Invariance or the CPT symmetry.

In order to test the validity of TSR a single experiment is not sufficient. Robertson stated in 1949 [9], that three experiments are necessary to test the TSR, respectively to replace Einstein's second postulate of the universality of the speed of light c by measurements. All of them are measurements of effects of second order in the speed of light.
The first of these experiments is the so called Ives-Stillwell experiment [10, 11]. This experiment, first performed in 1938, is a measurement of the time dilation predicted by the TSR. In the original setup measurements of the spectrum of the H_β lines ($\lambda = 486.1$ nm) have been performed on a beam of fast hydrogen ions (H_2^+, H_3^{2+}) to derive the associated Doppler shift of the frequency of the light emitted by the excited hydrogen atoms. In first order in the velocity of the beam the result is equal to the classical Doppler shift, predicted as well by TSR. To be able to measure the second order effect, Ives and Stillwell measured the shift of the mean of the frequencies of the light emitted in forward and backward direction of the beam, thus averaging out the first order Doppler effect. The Doppler shift predicted by Special Relativity is given by

$$\nu' = \frac{1 - (v/c)\cos\theta}{\sqrt{1 - (v/c)^2}} \cdot \nu_0, \tag{1.1}$$

where v is the velocity of the hydrogen beam, θ is the angle between the propagation directions of the beam and the emitted light, and ν_0 is the frequency of the respective transition in the rest frame of the atom. In case of validity of the TSR, the product of the frequencies of the light emitted in forward ($\nu_{||}$) and in backward ($\nu_{-||}$) direction should yield

$$\nu_{||} \cdot \nu_{-||} = \nu_0^2. \tag{1.2}$$

[1] The five existing superstring theories in 10 dimensions are proposed to be limits of a single theory in 11 dimensions, the so called M-theory

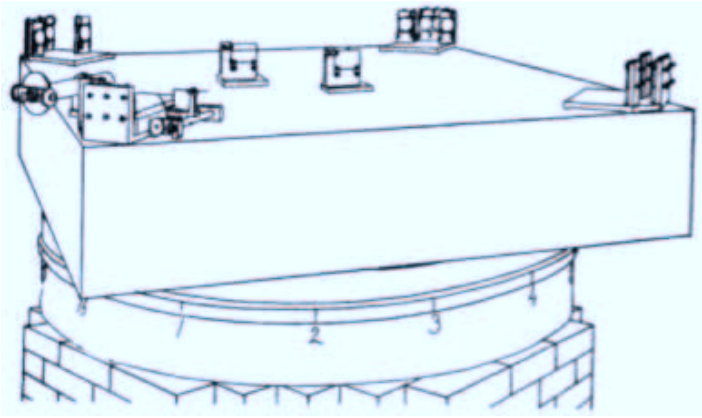

Figure 1.2.: *Original setup of the experiment performed by Michelson and Morley in 1887. The drawing has been taken from the original publication [2].*

Nowadays, Ives-Stillwell type experiments are performed on much faster ion beams in storage rings using collinear saturation spectroscopy of the atomic transition [12, 13] and frequency counting in the optical domain.

The second experiment necessary for a test of TSR is a measurement of the constancy of the speed of light. Such an experiment was performed for the first time by Kennedy and Thorndike in 1932 [14]. The principle on which the experiment is based is the simple proposition, that if a homogeneous light beam is split into two beams, which are overlapped again after traversing paths of different length, then the relative phase, and thus the interference fringes, will depend on the velocity of the apparatus unless the frequency of the light depends upon the velocity in the way required by special relativity [14]. In the experiment the modulation of the velocity of the apparatus, which was expected to shift the resonance fringes, occurs because of the rotation and the revolution of the earth. Modern versions of this experiment, e.g. [15], use a laser or a microwave generator frequency-locked to a highly stable cavity. The resonance frequency of this cavity is compared to the frequency of a stable atomic clock. The frequency difference should depend on the velocity of the apparatus towards some reference frame if Special Relativity is violated. As in the original version, the variation of the velocity occurs due to the rotation and the revolution of the earth. However, one could use as well high eccentricity orbits of a satellite for this measurement, as has been proposed by Lämmerzahl et al. [16] with the mission OPTIS. This would increase the detection sensitivity of the apparatus due to the higher velocity variations.

The third experiment necessary to prove the validity of the Theory of Special Relativity is a measurement of the isotropy of space, respectively of the speed of light. The famous experiment by Michelson and Morley [2], performed more than 100 years ago, was the first to test whether a dependence of the two-way speed of light on the propagation direc-

tion exists. The setup consisted of an interferometer with two orthogonal arms of equal length (see fig. 1.2). A beam of light from a monochromatic source was split into two parts using a beam-splitter. The two parts then propagated in orthogonal directions being retroreflected by several mirrors to increase the optical path length, which is one of the relevant measures for the sensitivity of the interferometer. Then the beams were combined again using a second beam-splitter and the interference pattern of the beams was observed using a telescope. At that time physicists expected the interference pattern to depend on the orientation of the apparatus due to the motion of the earth relative to the ether. The null-result of the Michelson-Morley experiment showed that no such effect is present.
This type of experiment has been repeated very often and the precision of the measurement increased enormously over the past 120 years thanks to technological advances. A first big step was made possible by the development of the laser delivering coherent light. The first to use lasers for a Michelson-Morley type experiment were Jaseja et al. [17] in 1965. They used the cavities of two He-Ne lasers oriented under 90° instead of an interferometer and measured variations of the frequency difference of the two lasers upon rotation. Brillet and Hall [18] used for the first time a system with a highly stable external resonator. One He-Ne laser ($\lambda = 3.39$ μm) was stabilized to a resonance frequency of this resonator and was compared to a second He-Ne laser stabilized to a transition in CH_4. The first laser was rotated, while the second served as a stationary reference.

The design of our apparatus follows the tracks of Brillet and Hall and uses optical standing-wave resonators for the measurements. We use two cavities, as first done by Müller et al. in 2003 [19] in a stationary system, yielding a hypothetical signal twice as large as in the case of a single rotating resonator. However, our apparatus is actively rotated, as have been the setups of Antonini et al. [20] and Herrmann et al. [21], and additionally equipped with an active vibration isolation system. A detailed description of the experimental setup will be given in chapter 3.

2. Theoretical Background

In order to determine to which degree a certain theory is valid, one has to derive quantitative measures for the validity of the theory. In principle one could use the theory under consideration to calculate how the outcome of an experiment should be and compare it to the measured result, but this can only give qualitative estimates of the validity of the theory, and it is almost impossible to compare the outcome of different experiments. Furthermore it is often not so easy to distinguish for a specific experiment from which incorrect theoretical assumption a possible deviation from the theory under consideration might stem from. In quantum field theory, e.g., a deviation might either stem from a not exactly valid Lorentz symmetry or from effects of the quantization procedure.
To be able to distinguish between different influences and to compare the outcomes of experiments of different types one therefore needs so called test theories. These are generalizations of the theory under test and introduce new parameters, which can be determined by experiments. In this way different aspects of a deviation from the theory can be modeled and parameterized. The outcome of experiments of different type can be compared [22].
In general one can distinguish two different kinds of test theories for TSR, namely the class of kinematical test theories, e.g. the Robertson-Mansouri-Sexl formalism [9, 23] or the c^2-formalism [24, 25], and the class of dynamical test theories, e.g. the Standard Model Extension [26], the $TH\epsilon\mu$-formalism [27, 28], or even more general formalisms [29].

Kinematical test theories generalize the transformations to be used between different inertial systems. All physical laws are treated in the same way since these test theories are independent from any particle model and the interactions amongst them. Disadvantages are the need for a preferred frame, which might not be unique and in which furthermore a certain geometry is assumed. Kinematical test theories do depend only on the relative velocity of the coordinate system used to describe a process versus the preferred frame. However, a violation of Lorentz invariance might come into play due to cosmological vector or tensor fields. Such effects cannot be described within kinematical test theories, which are incomplete in this sense.

Dynamical test theories use generalized Lagrangians or equations of motion to account for possible violations of Lorentz invariance. The most conservative approach is that of an effective field theory (EFT) [30]. Within this framework a possible Lorentz invariance violation can easily be integrated by introducing extra tensors. Both the Standard Model and General Relativity can be considered to be an effective field theory. An advantage of dynamical test theories is, that they can be made complete by construction by adding all interactions violating Lorentz invariance to the Lagrangian

of the system. Furthermore there is in principle no need for a preferred system of reference, although one has to agree on one system of reference in order to make results of experiments comparable, since the parameters of the Lorentz invariance violating contributions to the Lagrangian do depend on the choice of the reference frame.

2.1. Kinematical Framework

In the theory of Special Relativity the transformations between two different inertial systems S and S' moving with a constant velocity $\vec{v}$ relative to each other[1] are given by

$$\begin{aligned} t' &= \frac{1}{\sqrt{1-v^2/c^2}} \cdot (t - \frac{1}{c^2}(\vec{v}\cdot\vec{x})) \\ \vec{x}' &= \frac{1}{\sqrt{1-v^2/c^2}} \cdot \left(\frac{\vec{v}(\vec{v}\cdot\vec{x})}{v^2} - \vec{v}t\right) + \vec{x} - \frac{\vec{v}(\vec{v}\cdot\vec{x})}{v^2}, \end{aligned}$$

where it is assumed, that the orientations of the axis are the same for S and S' and the origins coincide for $t = t' = 0$. These transformations lead to the known effects of time dilation $\Delta t = \gamma \Delta t'$ [2], the twins paradox, length contraction $l = \frac{1}{\gamma} l'$, the Sagnac effect etc., of which most have been confirmed in experiments.

For a kinematical test theory of Special Relativity (SRT) one generalizes the above transformations

$$t' = t'(t, \vec{x}) \qquad\qquad \vec{x}' = \vec{x}'(t, \vec{x}).$$

Three requirements based on physical reasons restrict the form of the transformations:

1. A force-free motion has to be transformed into a force-free motion (no accelerations).
2. The transformation has to be bijective (a one-to-one mapping).
3. The transformation should depend on the relative motion only.

These requirements lead to the general form

$$\begin{aligned} t' &= a(v)t + e(v)\vec{v}\cdot\vec{x} \\ \vec{x}' &= d(v)\vec{x} + b(v)\frac{\vec{v}\,(\vec{v}\cdot\vec{x})}{v^2} + f(v)\vec{v}t, \end{aligned}$$

where $\vec{v}$ is the velocity of the origin of S in S', thus $\vec{x} = 0$ giving $\vec{x}' = \vec{v}t'$. Here, only three of the unknown functions $a(v), b(v), d(v), e(v)$ and $f(v)$ are of truly physical nature, two of

[1] $\vec{v}$ is the velocity of the origin of S' in the system S.
[2] $\gamma = 1/\sqrt{1-v^2/c^2}$

them are determined by the synchronization procedure used (e.g. Einstein-synchronization or synchronization via slow clock transport) and by the relative velocity between the inertial systems. Since one wants to test Lorentz invariance, namely the non-existence of a preferred frame of reference, one assumes the existence of a preferred frame of reference Σ with coordinates $\{T, X, Y, Z\}$, which is usually assumed to be the system in which the cosmic microwave background is isotropic [31], although the choice of this system is not unique. There might be other cosmologically preferred systems defined by other background fields, e.g. a stochastical background of gravitational waves [22].However, in this preferred system the speed of light is assumed to be isotropic, resulting in the known light cone from Special Relativity

$$ds^2 = dT^2 - dX^2 - dY^2 - dZ^2 = 0.$$

Transforming this into the system S one can derive a general formula for the velocity of light in this system

$$c(\theta, v, e) = \frac{b(v)d(v)(1 - v^2/c^2)}{adv\cos\theta + bde(1 - v^2/c^2)cos\theta - a\sqrt{b^2(1 - v^2/c^2) + (d^2 - b^2(1 - v^2/c^2))cos\theta}}.$$

where the speed of light depends on the propagation direction, the relative velocity v and the chosen synchronization for clocks.

2.1.1. Robertson-Mansouri-Sexl Test Theory

This test theory is a combination of work done by H.P. Robertson in the late 1940's [9] and by R. Mansouri and R.U. Sexl in the late 1970's [23, 32, 33].

Robertson stated, that the outcomes of 3 experiments are sufficient to replace Einstein's second postulate, the universality of the speed of light c. These experiments are the Michelson-Morley-experiment [2] measuring the isotropy of the speed of light, the Kennedy-Thorndike-experiment [34] measuring the effect of a moving source on the speed of light (influence of boosts) and the Ives-Stillwell-experiment [10, 11] measuring the time-dilation. All of them are measuring effects of second order in v/c. One specific feature of Robertson's framework was the application of Einstein-synchronization.

Mansouri and Sexl developed a more elaborate test theory. A driving force for their research was as well the discovery of the cosmic microwave background in 1964 [35], for which A.A. Penzias and R.W. Wilson received the Nobel Prize in 1978. This showed that a cosmologically preferred frame might indeed exist.
The starting point of their analysis was the role of convention in different definitions of clock synchronizations and the simultaneity [23]. They introduced generalized transformations as outlined in the general section. The assumption was made, that a preferred system exists and that within this system light propagation is isotropic. Furthermore the speed of

light should not depend on the motion of the source and it is assumed, that no preferred direction should exist in Σ.
Restricting oneself to the case of Einstein-synchronization one can derive the transformation equations between the preferred frame Σ and a system S moving relatively to Σ to be

$$\begin{aligned} t &= a(v)T - \frac{\vec{v}\cdot\vec{x}}{c^2} \\ \vec{x} &= b(v)\left(\vec{v}\left(\vec{v}\cdot\vec{X}\right)/v^2 - vT\right) + d(v)\left(\vec{X} - \vec{v}\left(\vec{v}\cdot\vec{X}\right)/v^2\right). \end{aligned}$$

Since usually the speed of the laboratory versus the preferred frame is small compared to c one may continue by making a Taylor expansion of the introduced coefficients $a(v)$, $b(v)$ and $d(v)$

$$a(v) = 1 + \alpha\frac{v^2}{c^2} + ..., \qquad b(v) = 1 + \beta\frac{v^2}{c^2} + ..., \qquad d(v) = 1 + \delta\frac{v^2}{c^2} + ...$$

where only even powers of v can contribute due to the isotropy in the system Σ. In case of a strict validity of Special Relativity and Lorentz Invariance the parameters α, β and δ would have the values

$$\alpha = -\frac{1}{2} \qquad \beta = \frac{1}{2} \qquad \delta = 0.$$

Further calculations lead to a formula for the relative shift of the speed of light as compared to the value in the system Σ

$$\frac{c}{c(\theta, v)} = 1 + (\beta - \delta - \frac{1}{2})\frac{v^2}{c^2}\sin^2\theta + (\alpha - \beta + 1)\frac{v^2}{c^2}. \tag{2.1}$$

Since the modulation is expected to be very small one can approximate $c/(c + \Delta c) \approx 1 - \Delta c/c$ and obtains a fractional shift of the speed of light

$$\frac{\Delta c(\theta, v)}{c} = -(\beta - \delta - \frac{1}{2})\frac{v^2}{c^2}\sin^2\theta - (\alpha - \beta + 1)\frac{v^2}{c^2}. \tag{2.2}$$

The first term $(\beta - \delta - 1/2)$ describes an anisotropy of the speed of light, which can be measured by a Michelson-Morley type experiment, while the second term $(\alpha - \beta + 1)$ describes a pure boost dependence of c, which can be measured in a Kennedy-Thorndike experiment. Furthermore it is possible to determine the parameter α, which is modeling the time dilation, in experiments of the Ives-Stilwell type. The combined results of all three experiments make it possible to determine the three coefficients α, β and γ.

An overview of the currently most accurate values obtained for the three parameter combinations is given in table 2.1.

parameter combination	value/limit	reference
$\beta - \delta - 1/2$	$(0.5 \pm 3 \pm 0.7) \cdot 10^{-10}$	Antonini et al. [36] (2005)
$\beta - \delta - 1/2$	$(-2.1 \pm 1.9) \cdot 10^{-10}$	Herrmann et al. [21] (2005)
$\beta - \delta - 1/2$	$(-9.4 \pm 8.1) \cdot 10^{-11}$	Stanwix et al. [37] (2006)
$\alpha - \beta + 1$	$< 6.6 \cdot 10^{-5}$	Hills and Hall [38] (1990)
$\alpha - \beta + 1$	$(1.9 \pm 2.1) \cdot 10^{-5}$	Braxmaier et al. [15] (2001)
$\alpha - \beta + 1$	$(1.6 \pm 3.0) \cdot 10^{-7}$	Wolf et al. [39] (2004)
$\lvert\alpha + 1/2\rvert$	$< 1 \cdot 10^{-6}$	Wolf and Petit [41] (1997)
$\lvert\alpha + 1/2\rvert$	$< 2.2 \cdot 10^{-7}$	Saathoff et al. [12] (2003)
$\lvert\alpha + 1/2\rvert$	$< 8.4 \cdot 10^{-8}$	Reinhardt et al. [13] (2007)

Table 2.1.: *Overview of upper limits on the parameters in the RMS test theory.*

Michelson-Morley type experiments

Antonini et al. [36] used a setup with standing-wave sapphire resonators at cryogenic temperatures, probed with a Nd:YAG laser, while Herrmann et al. [21] used standing wave resonators made from fused silica, also probed with a Nd:YAG laser. In contrast to this, Stanwix et al. [37] used whispering gallery modes of cylindrical sapphire resonators at cryogenic temperatures, which were probed using microwave radiation.

Kennedy-Thorndike type experiments

Hils and Hall [38] compared the resonance frequency of an optical cavity with an iodine standard and searched for variations in the frequency difference originating from the modulation of $\vec{v}$ due to earth's rotation. Braxmaier et al. [15] used a comparison between a cryogenic optical resonator from sapphire and compared it as well to an iodine standard. Their measurement span was longer allowing a search for modulations due to the orbital motion of the earth. Wolf et al. [39] used cryogenic sapphire resonators in the microwave region and compared them to a hydrogen maser.

Ives-Stilwell type experiments

Measurements of the time-dilation factor α with Ives-Stillwell type experiments have been performed on fast ion beams [40, 12, 13]. Limits have as well been derived via an analysis of data of the global positioning system (GPS) [41]. Currently the best measurement has been reported by Reinhardt et al. [13] at the heavy ion storage ring of the MPI for nuclear physics in Heidelberg using Lithium ions ($^7Li^+$).

2.2. Standard Model Extension

Towards the end of the 1990's theoreticians around V.A. Kostelecký developed a dynamical framework, which is able to model violations of Lorentz invariance in a very general way. This work was strongly motivated by theoretical discoveries in the 1980's showing that mechanisms can occur in string theories and in super-symmetry (SUSY) which give rise to spontaneous breaking of the Lorentz symmetry [8] or the CP/CPT symmetry [42, 43].

The starting point for their development of a test theory was the Standard Model of particle physics and the theory of General Relativity. Since it is believed that both theories are the low-energy limit of a more fundamental theory unifying gravitation and quantum theory presumably above the Planck scale $m_{Pl} = \sqrt{\hbar c/G} \approx 10^{19} GeV/c^2$ [44] such a theory should include all possible higher-order couplings between the Standard Model and General Relativity. Still it should maintain coordinate (or observer) independence [45]. In full generality other geometries as compared to the Minkowski-space time of Special Relativity/Standard Model and the Riemann-space time of General Relativity should be possible as well, e.g. a space time of the Riemann-Cartan type.
The general effective field theory incorporating all these assumptions is called the Standard Model Extension (SME). Its Lagrangian contains in principle an infinite number of terms. Since the energy scale where the merging of the theories might happen is far beyond reach[3], one can only search for the low-energy remnants, which are strongly suppressed and can only be identified in high precision experiments. For the design and interpretation of these experiments it is advantageous to restrict oneself to a subset of the full SME with a finite number of terms. One subset commonly applied is the so called minimal SME, which just considers power-counting renormalizable and gauge-invariant terms, conserving the $SU(3) \times SU(2) \times U(1)$ symmetry of the Standard Model.
Since for our experiment we are only dealing with electromagnetic interactions we restrict ourselves to an even smaller subset of the SME called the minimal QED sector of the SME.

2.2.1. Photonic Sector of the Minimal SME

In this subset of the full SME the Lagrangian including the Lorentz violating terms is, for a freely propagating photon, given by [26]

$$L = -\frac{1}{4} F_{\mu\nu} F^{\mu\nu} - \frac{1}{4} \left(k_F\right)_{\kappa\lambda\mu\nu} F^{\kappa\lambda} F^{\mu\nu} + \frac{1}{2} \left(k_{AF}\right)^{\kappa} \epsilon_{\kappa\lambda\mu\nu} A^{\lambda} F^{\mu\nu}, \tag{2.3}$$

where $F_{\mu\nu} = \partial_\mu A_\nu - \partial_\nu A_\mu$ is the electromagnetic field strength tensor and A^λ is the electromagnetic potential. The first term $-\frac{1}{4} F_{\mu\nu} F^{\mu\nu}$ reproduces the Maxwell equations of

[3] The highest energies are currently attainable at the Large Hadron Collider at CERN, designed to give 14 $TeV = 1.4 \times 10^4$ GeV for proton collisions and 1150 $TeV \approx 1.2 \times 10^6$ GeV for lead ion collisions.

electrodynamics, while the two other terms violate Lorentz invariance.

The coefficient k_{AF} has the dimension of a mass and gives rise to terms in the Lagrangian which are odd under CPT transformation. It is associated with negative contributions to the energy density and leads to further problematic implications as has been shown in [46]. Furthermore the magnitude $m_{AF} = (k_{AF})_\kappa (k_{AF})^\kappa$ of the vector $(k_{AF})^\mu$ is restricted by astrophysical observations [47] of expected birefringence effects on the light of distant radio galaxies to $m_{AF} < 1.7 \times 10^{-41} h_0\ GeV$, h_0 being the Hubble constant. Other astrophysical observations [48, 49] support this limit. Therefore this term is neglected in our further analysis and we set $k_{AF} \equiv 0$, just keeping

$$L = -\frac{1}{4} F_{\mu\nu} F^{\mu\nu} - \frac{1}{4} \left(k_F\right)_{\kappa\lambda\mu\nu} F^{\kappa\lambda} F^{\mu\nu}$$

as the modified Lagrangian for a freely propagating photon. From the Lagrangian we derive the equation of motion to be [50]

$$\partial_\alpha F^\alpha_\mu + (k_F)_{\mu\alpha\beta\gamma} \partial^\alpha F^{\beta\gamma} = 0. \tag{2.4}$$

The coefficients of the tensor k_F, which is even under CPT and shows the same symmetry as the Riemann curvature tensor, are dimensionless. The symmetry of the tensor together with a normalization condition, the vanishing of the double trace[4], restricts the number of independent components of the tensor to 19.
To get more insight into the physical meaning of the equation above the following linear combinations of the components are formed:

$$\begin{aligned}
(\kappa_{DE})^{jk} &= -2(k_F)^{0j0k} \\
(\kappa_{HB})^{jk} &= \frac{1}{2} \epsilon^{jpq} \epsilon^{krs} (k_F)^{pqrs} \\
(\kappa_{DB})^{jk} &= (k_F)^{0jpq} \epsilon^{kpq} \\
(\kappa_{HE})^{jk} &= -(\kappa_{DB})^{kj}.
\end{aligned} \tag{2.5}$$

Furthermore, in analogy to the procedure in Maxwell's electrodynamics, new fields $\vec{D}$ and $\vec{H}$ are defined according to

$$\begin{pmatrix} \vec{D} \\ \vec{H} \end{pmatrix} = \begin{pmatrix} 1 + \kappa_{DE} & \kappa_{DB} \\ \kappa_{HE} & 1 + \kappa_{HB} \end{pmatrix} \cdot \begin{pmatrix} \vec{E} \\ \vec{B} \end{pmatrix} \tag{2.6}$$

[4]The double trace (dtrace) is defined as $\mathrm{dtrace}(k_F) = (k_F)_{\kappa\kappa\lambda\lambda}$ using Einsteins summing convention.

Then, from equation 2.4 together with equation 2.6 we get the usual form of Maxwell's equations in an anisotropic medium

$$\begin{aligned} \vec{\nabla} \times \vec{H} - \partial_0 \vec{D} &= 0 \\ \vec{\nabla} \times \vec{E} + \partial_0 \vec{B} &= 0 \\ \vec{\nabla} \cdot \vec{D} &= 0 \\ \vec{\nabla} \cdot \vec{B} &= 0. \end{aligned} \tag{2.7}$$

Note that the whole derivation has only been dealing with photons alone, therefore regarding the case of vacuum. The result of the calculation shows however, that the vacuum behaves like an anisotropic medium. Thus anisotropy of the speed of light and birefringence of the vacuum might occur. For ease of description of our experiment in this test theory we introduce the following linear combinations of the matrices κ_{DE}, κ_{HB}, κ_{DB} and κ_{HE}

$$\begin{aligned} (\tilde{\kappa}_{e+})^{jk} &= \frac{1}{2}\left(\kappa_{DE} + \kappa_{HB}\right)^{jk} \\ (\tilde{\kappa}_{e-})^{jk} &= \frac{1}{2}\left(\kappa_{DE} - \kappa_{HB}\right)^{jk} - \frac{1}{3}\delta^{jk}(\kappa_{DE})^{ll} \\ (\tilde{\kappa}_{o+})^{jk} &= \frac{1}{2}\left(\kappa_{DB} + \kappa_{HE}\right)^{jk} \\ (\tilde{\kappa}_{o-})^{jk} &= \frac{1}{2}\left(\kappa_{DB} - \kappa_{HB}\right)^{jk} \\ \tilde{\kappa}_{tr} &= \frac{1}{3}(\kappa_{DE})^{ll}, \end{aligned} \tag{2.8}$$

where the $(\tilde{\kappa}_e)$ matrices are even under parity operations while the $(\tilde{\kappa}_o)$ matrices are odd under parity operations. The sign $\pm$ specifies the linear combination and tr marks, that the scalar is a trace. Since $\tilde{\kappa}_{tr}$ is a scalar it is therefor invariant under rotations, the matrix $\tilde{\kappa}_{o+}$ is asymmetric and contains 3 independent coefficients. The three matrices $\tilde{\kappa}_{e-}$, $\tilde{\kappa}_{e+}$ and $\tilde{\kappa}_{o-}$ are symmetric and have a vanishing trace. Each of these has 5 independent coefficients. Using these new matrices and the scalar one can rewrite the Lagrangian using the $\vec{E}$ and $\vec{B}$ fields

$$\begin{aligned} L = \frac{1}{2}\left[\left(1 + \tilde{\kappa}_{tr}\right)\mathbf{E}^2 - \left(1 - \tilde{\kappa}_{tr}\right)\mathbf{B}^2\right] + \frac{1}{2}\mathbf{E} \cdot \left(\tilde{\kappa}_{e-} + \tilde{\kappa}_{e+}\right) \cdot \mathbf{E} \\ - \frac{1}{2}\mathbf{B} \cdot \left(\tilde{\kappa}_{e+} - \tilde{\kappa}_{e-}\right) \cdot \mathbf{B} + \mathbf{E} \cdot \left(\tilde{\kappa}_{o+} + \tilde{\kappa}_{o-}\right) \cdot \mathbf{B}. \end{aligned}$$

By comparison with the normal Lagrangian of the electromagnetic field in vacuum

$$L_{Max} = \frac{1}{2}(\vec{E}^2 - \vec{B}^2)$$

one can see that the coefficient $\tilde{\kappa}_{tr}$ shifts the effective permettivity ϵ and the effective permeability μ of the vacuum. Furthermore it can be seen that birefringence of the vacuum

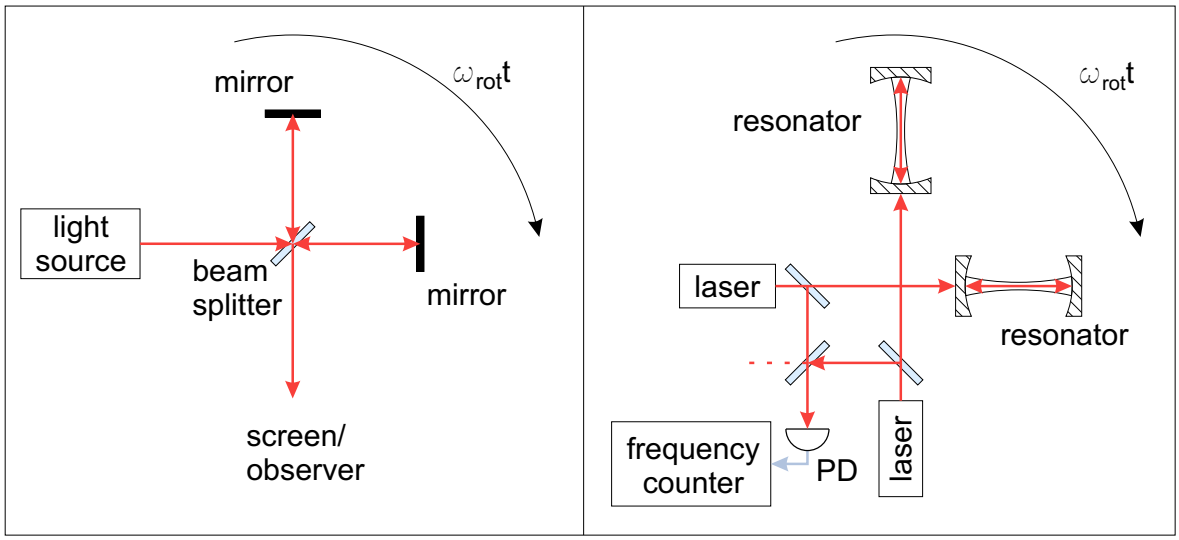

Figure 2.1.: *Basic layout of the original Michelson-Morley experiment using a Michelson interferometer (left) and the modern version using lasers and resonators (right). PD: photodiode*

is controlled by the matrices $(\tilde{\kappa}_{e+})$ and $(\tilde{\kappa}_{o-})$ [50, 51]. From astrophysical observations upper limits for the coefficients of these matrices have been derived ($< 2 \cdot 10^{-32}$) [47, 48], which are well below the sensitivity expected for our setup. Thus these coefficients will be considered to be zero in the further analysis.

2.3. Laboratory Test - The Michelson-Morley Type Experiment

To test whether an anisotropy of the speed of light might exist, we use a modern version of the Michelson-Morley setup with optical resonators representing the interferometer arms. Figure 2.1 shows the principal layout in comparison to the original work using a Michelson-interferometer.

In the experiment by Michelson and Morley [2] a beam of monochromatic light was split by a beam splitter and sent along two orthogonal arms, at whose ends the beams were retroreflected. Via the beam splitter the two beams were overlapped again, and in the output of the interferometer one observed interference fringes.These are expected to change upon rotation in case of an anisotropy of c.

In the modern version the coherent light of lasers is used to probe the resonance frequencies of optical resonators. Therefore the frequency of each laser output is stabilized to the resonance frequency of the respective resonator. A part of the light is split from the main beams and is made to overlap on a photodiode, resulting in a beat. Detection of the power of this beam via a photodiode yields an amplitude-modulated current with the frequency being

the difference of the resonance frequencies of the two resonators. Again, this measurement is performed as a function of the orientation of the apparatus. The resonance frequency of a resonator is (for plane mirrors) given by the mirror spacing L and the speed of light c

$$\begin{aligned} \nu_0 &= N \cdot \frac{c}{2L} \\ &= N \cdot \nu_{FSR}. \end{aligned} \tag{2.9}$$

Here N is the so called mode number, ν_{FSR} is the free spectral range of the resonator, which is hypothetically the lowest possible frequency of a standing wave which could be supported by the resonator[5]. Now in case of an anisotropy the resonance frequency will be shifted according to the directional dependence of the speed of light $c(\theta)$. Due to the symmetry of the resonator it is to be expected qualitatively, that the resonance frequency will be modulated at twice the rotation frequency upon rotation of the setup, hence the shift can be described via

$$\frac{\Delta\nu}{\nu_0} = B \sin 2\omega_{rot} t + C \cos 2\omega_{rot} t, \tag{2.10}$$

where $\nu_0 \approx 2.82 \cdot 10^{14}$ Hz for a Nd:YAG-laser operating at $\lambda = 1064$ nm.
Due to the rotation of the earth and the orbital motion one might expect an additional modulation to come into play, so the amplitudes B and C might be modulated according to

$$\begin{aligned} B &= B_0 + B_{s1} \sin \omega_\oplus T_\oplus + B_{c1} \cos \omega_\oplus T_\oplus + B_{s2} \sin 2\omega_\oplus T_\oplus + B_{c2} \cos 2\omega_\oplus T_\oplus \\ C &= C_0 + C_{s1} \sin \omega_\oplus T_\oplus + C_{c1} \cos \omega_\oplus T_\oplus + C_{s2} \sin 2\omega_\oplus T_\oplus + C_{c2} \cos 2\omega_\oplus T_\oplus, \end{aligned} \tag{2.11}$$

with coefficients B_i, C_i which are themselves modulated at an annular frequency.

2.3.1. Definition of the Reference Frame

As explained above, the Standard Model Extension (SME) does not require any preferred reference system, but the value of the coefficients describing Lorentz invariance violation or CPT violation do depend on the chosen coordinate system. Thus, to make experiments and values of different groups comparable one has to agree on a common reference frame for the data evaluation.
For the Robertson-Mansouri-Sexl (RMS) frame on the other hand a preferred system has to be chosen. It is assumed, that the frame in which the cosmic microwave background is isotropic might be a good candidate.
Kostelecký proposed for the SME test theory a sun centered celestial equatorial frame (SCCEF) [50] and this has been generally adopted as reference for the $\tilde{\kappa}$ matrices. For the

[5] In reality this is not the case since the mirrors are only reflective in a small wavelength range.

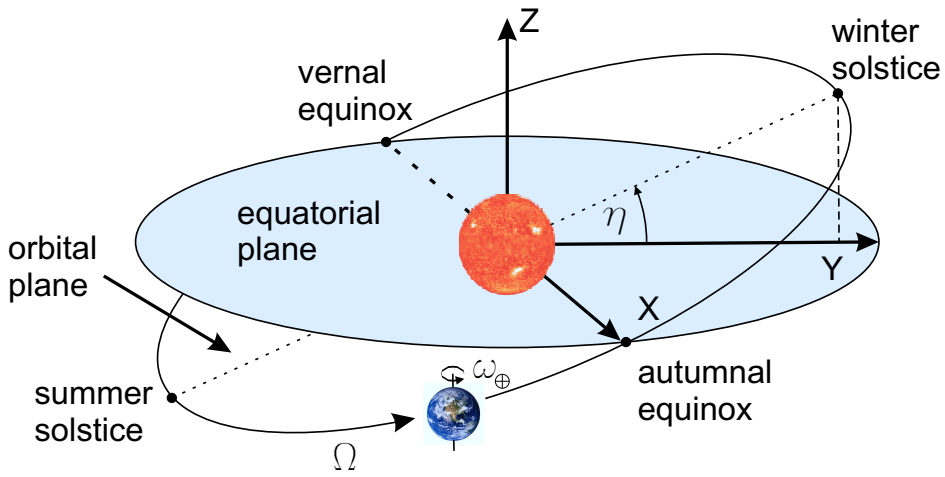

Figure 2.2.: *Definition of the sun centered celestial equatorial frame (SCCEF). The Z-axis is parallel to the axis of rotation of the earth and points in northern direction, the X-axis lies in the equatorial plane and points in the direction of the sun at the time of the vernal equinox. The Y-axis completes the right-handed coordinate system.*

typical timescale of experiments in this field (≈ 1 year of data) a sun centered coordinate system can be treated as being an inertial system. This coordinate system is as well useful for evaluating the data in the RMS-framework, since it is moving with a constant velocity and orientation versus the cosmic microwave background. In the following capital letters will be used for coordinates and coefficients in the SCCEF, small letters for coordinates in the laboratory frame.

The axes of the SCCEF (see figure 2.2) are defined in the following way [52, 50]:

- The origin of the system lies in the center of the sun.
- The Z-axis is oriented parallel to the rotation axis of the earth and is therefore normal to the equatorial plane of the earth. Thus the XY-plane corresponds to the equatorial plane of the earth shifted to the center of the sun.
- In the course of a tropical year the earth moves within the plane of the ecliptic. Twice a year the XY-plane defined above coincides with the equatorial plane of the earth, once in spring and once in autumn, defining the points of vernal and autumnal equinox, respectively. The X-axis is chosen to point from the position of the earth at the time of the vernal equinox towards the sun. Since this point is moving relative to the system of fixed stars one has to agree on an epoch to use as reference. In our case this is the year 2000.

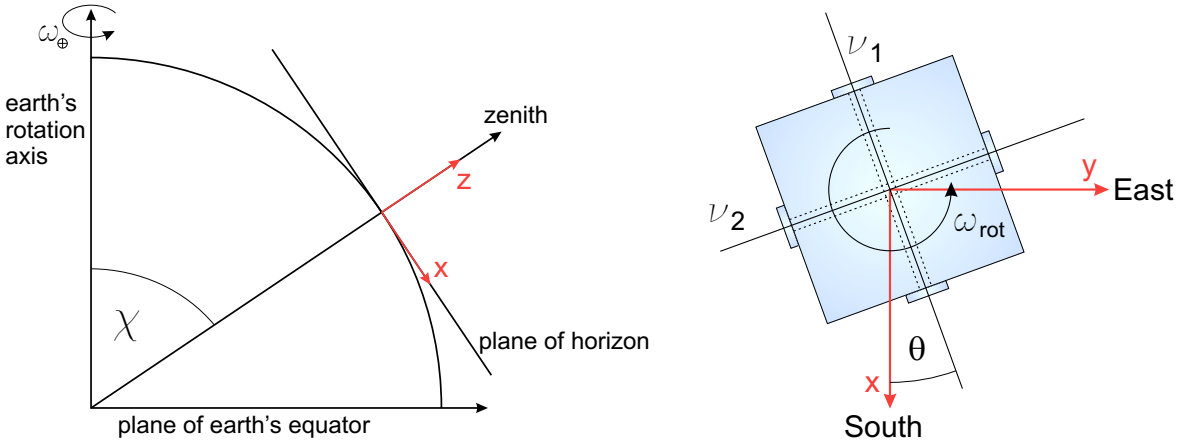

Figure 2.3.: *Orientation of the axes in the frame of the laboratory at a colatitude χ. The z-axis points upwards, while the x- and y-axes lie in the plane of the horizon. The x-axis points southwards, the y-axis eastwards.*

- The Y-axis is chosen to complete the right-handed coordinate system.

The coordinate system x, y, z for the laboratory frame is defined such that the x-axis points in southern direction (see figure 2.3), the y-axis points in eastern direction and the z-axis points vertically upwards. The x- and y-axis lie both in the plane of horizon. Since the laboratory frame is no inertial frame, the coefficients determined in the laboratory frame will show variations due to the orbital motion and the rotation of the earth.

2.3.2. Description in the SME

First we assume the nonexistence of an anisotropy. Then for a given resonator the angular frequency is $\omega_0 = 2\pi\nu_0$ and $\vec{E}_0, \vec{B}_0, \vec{D}_0$ and $\vec{H}_0$ are the fields associated with the mode resonant in the cavity. Now if anisotropy occurs as described by a non-vanishing tensor k_F, then the fields within the resonator will be perturbed and the angular frequency will be shifted. These perturbed fields may be identified by $\vec{E}, \vec{B}, \vec{D}$ and $\vec{H}$ and $\delta\nu$ is the shift of the resonance frequency. Then, according to [50], the fractional shift in the resonance frequency can be written as

$$\begin{aligned} \frac{\delta\nu}{\nu} &= -\left(\int_V d^3x(\vec{E}_0^* \cdot \vec{D} + \vec{H}_0^* \cdot \vec{B})\right)^{-1} \\ &\quad \times \int_V d^3x(\vec{E}_0^* \cdot \vec{D} - \vec{D}_0^* \cdot \vec{E} - \vec{B}_0^* \cdot \vec{H} + \vec{H}_0^* \cdot \vec{B} \\ &\quad -\frac{i\vec{\nabla}}{\omega_0} \cdot (\vec{H}_0^* \times \vec{E} - \vec{E}_0^* \cdot \vec{H})), \end{aligned} \tag{2.12}$$

with V being the volume of the resonator. Since we expect only tiny deviations we may neglect the last term with the derivative. Now we expand equation 2.12 in the coefficients of k_F using equation 2.7 and obtain for the resonator in vacuum with the substitution

$$\vec{D} - \vec{E} \cong (\kappa_{DE})_{lab} \cdot \vec{E}_0 + (\kappa_{DB})_{lab} \cdot \vec{B}_0$$
$$\vec{H} - \vec{B} \cong (\kappa_{HE}))_{lab} \cdot \vec{E}_0 + (\kappa_{HB})_{lab} \cdot \vec{B}_0$$

for the fractional frequency shift the term

$$\frac{\delta\nu}{\nu} = -\frac{\int_V d^3x(\vec{E}_0^*(\kappa_{DE})_{lab}\vec{E}_0 - \vec{B}_0^*(\kappa_{HB})_{lab}\vec{B}_0) + 2\Re(\vec{E}_0^*(\kappa_{DB})_{lab}\vec{B}_0)}{\int_V d^3x(\vec{E}_0 \cdot \vec{D}_0^* + \vec{B}_0^* \cdot \vec{H}_0^*)}. \tag{2.13}$$

For further evaluation we have to specify the electric and magnetic fields of our experimental setup. In general one can make the following ansatz for the unperturbed fields[6] [50]

$$\begin{aligned} \vec{E}_0(\vec{x}) &= \vec{e}_0 \cos(\omega_0 \hat{N} \cdot \vec{x} + \phi) e^{-i\omega_0 t} \\ \vec{B}_0(\vec{x}) &= i\hat{N} \times \vec{e}_0 \sin(\omega_0 \hat{N} \cdot \vec{x} + \phi) e^{-i\omega_0 t}, \end{aligned} \tag{2.14}$$

where $\hat{N}$ is a unit vector pointing along the axis of the respective resonator. The constant $\vec{e}_0$ specifies the magnitude and polarization of the field. Equation 2.13 can be simplified yielding

$$\frac{\delta\nu}{\nu} = -\frac{1}{2|\vec{e}_0|^2}\left[\vec{e}_0^*(\kappa_{DE})_{lab}\vec{e}_0 - (\hat{N} \times \vec{e}_0^*)(\kappa_{HB})_{lab}(\hat{N} \times \vec{e}_0)\right]. \tag{2.15}$$

It is obvious that the frequency shift is just a function of the orientation of the resonator and the polarization of the electromagnetic field.
For our experiment we use a monolithic construction of the resonators, which are embedded in one block under an angle of 90°, thus the vectors $\hat{N}_i$ for our two cavities are given by

$$\hat{N}_1 = \begin{pmatrix} \cos\theta(t) \\ \sin\theta(t) \\ 0 \end{pmatrix} \quad , \quad \hat{N}_2 = \begin{pmatrix} \sin\theta(t) \\ -\cos\theta(t) \\ 0 \end{pmatrix}, \tag{2.16}$$

where θ is the angle of the axis of resonator 1 with respect to the x-axis of the laboratory, which is oriented in southern direction. In contrast to the polarization direction chosen in [50] our polarization is not along the z-axis, but is lying perpendicular to the z-axis and the resonators axes[7], thus the polarization vectors are given by

$$\vec{e}_1 = e_1 \begin{pmatrix} -\sin\theta(t) \\ \cos\theta(t) \\ 0 \end{pmatrix} \quad , \quad \hat{e}_2 = e_2 \begin{pmatrix} \cos\theta(t) \\ \sin\theta(t) \\ 0 \end{pmatrix}. \tag{2.17}$$

[6] Cavities void of matter are assumed, thus the relative permettivity ϵ and permeability μ are 1 (natural units, $c = 1$).

[7] For the assumed circumstances $\epsilon = 1$, $\mu = 1$ and vanishing $(\tilde{\kappa}_{e+}), (\tilde{\kappa}_{o-})$ this yields the same results as in [50].

Substituting these vectors in the relation 2.15 for resonator 1 we obtain

$$\begin{aligned}\frac{\delta\nu_1}{\nu} &= -\frac{1}{4}\left[2(\kappa_{HB})^{33}_{lab} - (\kappa_{DE})^{11}_{lab} - (\kappa_{DE})^{22}_{lab}\right] \\ &\quad -\frac{1}{2}(\kappa_{DE})^{12}_{lab}\sin 2\theta(t) - \frac{1}{4}((\kappa_{DE})^{11}_{lab} - (\kappa_{DE})^{22}_{lab})\cos 2\theta(t) \\ &= A + B\sin 2\theta(t) + C\cos 2\theta(t)\end{aligned} \tag{2.18}$$

and exactly the same term for resonator 2, but with the angle θ replaced by $\theta - \pi/2$. Thus the difference of the resonance frequencies of the resonators $\nu_1 - \nu_2$ shows a frequency shift

$$\frac{\delta(\nu_1 - \nu_2)}{\nu} = 2B(t)\sin 2\theta(t) + 2C\cos 2\theta(t), \tag{2.19}$$

as already expected due to the symmetry of the system.
Since the rotating earth is no inertial system and therefore the determined coefficients κ_{lab} are not constant over time, we have to use an observer Lorentz transformation [50] to transform the result into the SCCEF, where the coefficients $\tilde{\kappa}$ are constant. The observer Lorentz transformation is given by

$$\Lambda^{\mu}_{\nu} = \begin{pmatrix} 1 & -\beta^1 & -\beta^2 & -\beta^3 \\ -(R\cdot\vec{\beta})^1 & R^{11} & R^{12} & R^{13} \\ -(R\cdot\vec{\beta})^2 & R^{21} & R^{22} & R^{23} \\ -(R\cdot\vec{\beta})^3 & R^{31} & R^{32} & R^{33} \end{pmatrix} \tag{2.20}$$

consisting of a Lorentz boost due to the velocity $\vec{\beta}$ of the laboratory versus the SCCEF

$$\vec{\beta} = \beta_{\oplus}\begin{pmatrix} \sin\Omega_{\oplus}T \\ -\cos\eta\cos\Omega_{\oplus}T \\ -\sin\eta\cos\Omega_{\oplus}T \end{pmatrix} + \beta_L\begin{pmatrix} -\sin\omega_{\oplus}T_{\oplus} \\ \cos\omega_{\oplus}T_{\oplus} \\ 0 \end{pmatrix} \tag{2.21}$$

and an ordinary rotation

$$R = \begin{pmatrix} \cos\chi\cos\omega_{\oplus}T_{\oplus} & \cos\chi\sin\omega_{\oplus}T_{\oplus} & -\sin\chi \\ -\sin\omega_{\oplus}T_{\oplus} & \cos\omega_{\oplus}T_{\oplus} & 0 \\ \sin\chi\cos\omega_{\oplus}T_{\oplus} & \sin\chi\sin\omega_{\oplus}T_{\oplus} & \cos\chi \end{pmatrix} \tag{2.22}$$

of the coordinate system. Here $\beta_{\oplus} = v_{\oplus}/c \approx 1{\cdot}10^{-4}$ is the speed of the orbital motion of the earth around the sun, $\Omega_{\oplus}$ is the corresponding angular frequency. $\beta_L = r_{\oplus}\omega_{\oplus}\sin\chi \approx 10^{-6}$ is the speed of the laboratory within the SCCEF due to the rotation of the earth, $\omega_{\oplus}$ is again the angular frequency of this rotation. χ is the colatitude of the laboratory. The angle $\eta = 23.4°$ is the angle between the XY celestial plane and the earth's orbital plane.

Two timescales have to be used in the description of the motion of the earth within the SCCEF. The timescale $T_\oplus$ used for the description of the rotation of the earth can be chosen to be zero at any instant when the y-axis of the laboratory system and the Y-axis of the SCCEF coincide[8]. The timescale T used for the orbital motion is set to zero at the time of the vernal equinox in the year 2000, i.e. when the earth crossed the equatorial plane of the SCCEF (compare figure 2.2) in spring 2000[9].
With the transformation matrix given above one can now relate the coefficients in the laboratory frame $(\kappa)_{lab}$ with the coefficients of the matrices in the SCCEF, yielding

$$\begin{aligned}
(\kappa_{DE})^{jk}_{lab} &= T_0^{jkJK}(\kappa_{DE})^{JK} - T_1^{(jk)JK}(\kappa_{DB})^{JK} \\
(\kappa_{HB})^{jk}_{lab} &= T_0^{jkJK}(\kappa_{HB})^{JK} - T_1^{(jk)KJ}(\kappa_{DB})^{JK} \\
(\kappa_{DB})^{jk}_{lab} &= T_0^{jkJK}(\kappa_{DB})^{JK} + T_1^{kjJK}(\kappa_{DE})^{JK} + T_1^{jkJK}(\kappa_{HB})^{JK},
\end{aligned} \tag{2.23}$$

where

$$T_0^{jkJK} = R^{jJ}R^{kK}, \qquad T_1^{jkJK} = R^{jP}\epsilon^{KPQ}\beta^Q. \tag{2.24}$$

T_0 is a rotation, T_1 is a leading order boost contribution.

The temporal behavior during active rotation is still given by equation 2.19, the coefficients $B(t), C(t)$ show now a specific temporal behavior due to the orbital motion and the rotation of the earth, which is given in the form

$$\begin{aligned}
B(t) &= B_0 + B_1 \sin\omega_\oplus T_\oplus + B_2 \cos\omega_\oplus T_\oplus \\
&\quad + B_3 \sin 2\omega_\oplus T_\oplus + B_4 \cos 2\omega_\oplus T_\oplus \\
C(t) &= C_0 + C_1 \sin\omega_\oplus T_\oplus + C_2 \cos\omega_\oplus T_\oplus \\
&\quad + C_3 \sin 2\omega_\oplus T_\oplus + C_4 \cos 2\omega_\oplus T_\oplus,
\end{aligned} \tag{2.25}$$

where the coefficients B_i, C_i are slowly time-varying functions due to the orbital motion. They contain different combinations of the $(\tilde{\kappa}_{e+}), (\tilde{\kappa}_{e-}), (\tilde{\kappa}_{o+})$ and $(\tilde{\kappa}_{o-})$ matrices. Their exact form as given in [50] can be found in appendix C. The different components of the $(\tilde{\kappa}_{e-})$-matrix are determined by constant offsets of the determined modulation coefficients B_i, C_i while the three independent components of the $(\tilde{\kappa}_{o+})$-matrix are determined by modulations of these coefficients with a period of one sidereal year.

2.3.3. Description in the RMS-frame

For the RMS framework the SCCEF described above is as well a suitable choice, since it almost realizes an inertial system with constant velocity versus the cosmic microwave

[8] This happens once every sidereal day, corresponding to 23h 55' 56".
[9] This was on march 20th 7:36 a.m. UTC according to the US Naval Observatory (USNO), http://www.usno.navy.mil/USNO/astronomical-applications/data-services/earth-seasons

background (CMB). The direction and magnitude of the velocity $\vec{v}_{solar}$ of the solar system versus the CMB can be derived from the anisotropy observed in the radiation of the CMB, which shows dipole character with a maximum deviation of $\approx 3mK$ from the mean temperature of the background. From the differences one can derive the magnitude of the relative velocity to be $v_{solar} \approx 370\frac{km}{s}$. The direction is in the celestial equatorial frame given by the declination $\Theta = -6°$ and the right ascension $\Phi = 168°$ [31].

In the RMS frame the speed of light is expected to vary according to equation 2.2. We have to calculate the shift of the resonance frequency for each resonator. The axis of the resonators may have the angles $\theta_1(t)$ and $\theta_2(t)$ with respect to the velocity towards the CMB. Since the relative shift of the resonance frequency is identical to the relative shift in the speed of light, we can write

$$\frac{\Delta\nu_1 - \Delta\nu_2}{\nu_0} = -(\beta - \delta - \frac{1}{2})\frac{v^2}{c^2}\left[\sin^2\theta_1(t) - \sin^2\theta_2(t)\right]. \tag{2.26}$$

To derive the time dependence of this expression we may use the identity

$$\sin^2\theta_i(t) = 1 - \cos^2\theta_i(t) = 1 - (\vec{v}(t)\cdot\hat{e}_i)^2/v^2, \tag{2.27}$$

or alternatively

$$v^2\sin^2\theta_i(t) = |\vec{v}\times\hat{e}_i|^2, \tag{2.28}$$

$\hat{e}_i$ being a unit vector pointing along the axis of the respective resonator. For the actively rotating setup this means in the laboratory frame

$$\hat{e}_{1,lab}(t) = \begin{pmatrix}\cos\omega_{rot}t\\ \sin\omega_{rot}t\\ 0\end{pmatrix} \quad , \quad \hat{e}_{2,lab}(t) = \begin{pmatrix}\sin\omega_{rot}t\\ -\cos\omega_{rot}t\\ 0\end{pmatrix}. \tag{2.29}$$

Rotation of these unity vectors into the SCCEF frame and calculation of the velocity of the laboratory relative to the CMB,

$$\begin{aligned}\vec{v} &= \vec{v}_{solar} + \vec{v}_{orbital} + \vec{v}_{\oplus}\\ &= v_{solar}\begin{pmatrix}\cos\Phi\cos\Theta\\ \sin\Phi\cos\Theta\\ -\sin\Theta\end{pmatrix} + v_{orb}\begin{pmatrix}\sin\Omega T\\ -\cos\Omega T\cos\eta\\ -\cos\Omega T\sin\eta\end{pmatrix} + v_{\oplus}\begin{pmatrix}-\sin\omega_{\oplus}T_{\oplus}\\ \cos\omega_{\oplus}T_{\oplus}\\ 0\end{pmatrix},\end{aligned}$$

gives for the shift of the difference of the resonance frequencies a sum of terms, which can be arranged into coefficients comparable to the SME case,

$$\frac{\delta(\nu_1 - \nu_2)}{\nu} = 2B(t)\sin 2\theta(t) + 2C\cos 2\theta(t),$$

γ_0	$\frac{1}{4}\sin^2\chi(3\cos 2\Theta - 1)$		
γ_1	$-\frac{1}{2}\sin 2\Theta \sin 2\chi \cos\Phi$	σ_1	$-\frac{1}{2}\sin 2\Theta \sin 2\chi \sin\Phi$
γ_2	$-\frac{1}{4}\cos 2\Phi \cos^2\Theta(\cos 2\chi + 3)$	σ_2	$-\frac{1}{4}\sin 2\Phi \cos^2\Theta(\cos 2\chi + 3)$
γ_3	$-\sin\chi \sin 2\Theta \sin\Phi$	σ_3	$\cos\Phi \sin\chi \sin 2\Theta$
γ_4	$-\cos^2\Theta \cos\chi \sin 2\Phi$	σ_4	$\cos^2\Theta \cos\chi \cos 2\Phi$

Table 2.2.: *Values of the constants γ_i and σ_i in the fit function of the RMS model. Here terms occuring due to the modulation of the velocity because of the orbital motion and the rotational velocity of the earth have been neglected. The expression containing terms up to first order in the orbital velocity is given in appendix B.*

where the coefficients $2B(t)$ and $2C(t)$ are given by

$$\begin{aligned} 2B(t) &= (1/2 - \beta + \delta)(v_{solar}^2/c_0^2)(\gamma_3 \cos\omega_\oplus T_\oplus + \gamma_4 \cos 2\omega_\oplus T_\oplus + \sigma_3 \sin\omega_\oplus T_\oplus \\ &\quad + \sigma_4 \sin 2\omega_\oplus T_\oplus) \\ 2C(t) &= (1/2 - \beta + \delta)(v_{solar}^2/c_0^2)(\gamma_0 + \gamma_1 \cos\omega_\oplus T_\oplus + \gamma_2 \cos 2\omega_\oplus T_\oplus \\ &\quad + \sigma_1 \sin\omega_\oplus T_\oplus + \sigma_2 \sin 2\omega_\oplus T_\oplus). \end{aligned} \tag{2.30}$$

Table 2.2 lists the form of the coefficients γ_i, σ_i. Terms arising due to the modulation of the laboratory's velocity by the orbital ($v_{orb} \approx 30$ km/s) and the rotational motion ($v_\oplus = \omega_\oplus \cdot r_{earth} \approx 0.46$ km/s) of the Earth have been neglected and only modulations due to the variation of the orientation of the cavities have been considered. The expressions for the coefficients as obtained from the calculation without neglecting velocity modulations due to the orbital motion can be found in appendix B.

3. Experimental Setup

3.1. Overview

A schematic drawing of our "Speed of Light Isotropy Test" (SLIT) apparatus is shown in Fig. 3.1. Figure 3.2 shows a picture of the setup.

One important feature of the apparatus is the use of a monolithic resonator structure, where two high finesse optical resonators are embedded in a cross geometry in a block of ultra low expansion coefficient glass (ULE). In former experiments testing the Lorentz invariance for electromagnetic waves with resonators separate resonators made from sapphire [20, 53] were used. These resonators were operated around 3 K to take advantage of the fact that sapphire has an extremely low coefficient of thermal expansion at cryogenic temperatures, since quite in general for dielectric crystals the CTE at low temperatures behaves like $CTE \propto T^3$ (see e.g. [54]).
Our monolithic design allows for common mode rejection of certain disturbances, which reduces the noise level present in our measurements. The use of ULE allows the operation of the experiment at room temperature since ULE has an extremely small coefficient of thermal expansion at this temperature. The resonator block is placed inside a vacuum chamber ($p \approx 10^{-7}$ mbar) which is stabilized to a temperature of $\approx 30°$C.
The use of a sophisticated laser lock scheme consisting of a prestabilization scheme and fine locks in transmission allows the highly precise readout of the resonance frequencies of the resonators. With a frequency counter the difference between the resonance frequencies of the resonators is measured as a function of the orientation of the apparatus.
A strong reduction of measurement noise is enabled by the use of active vibration supports, which suppress mechanical vibrations of the optical setup and thus reduce the frequency noise of the laser system and the resonators. This results in a smaller line width of the beat between the two resonators frequencies.
Another highlight of the experimental setup is the use of a high precision air bearing rotation table for the active rotation of the experiment. This table exhibits a very small wobble of the rotation axis and a high stability of the angular velocity. This reduces systematic effects occurring due to a tilt of the resonator structure or due to varying centrifugal forces. As has been shown in chapter 1, active rotation of the experiment is necessary to extract a value for the coefficient $(\tilde{\kappa}_{e-})^{ZZ}$ of the SME. Furthermore active rotation has the advantage, that the timescale on which the system has to be extremely stable is shifted from half a day to half a period of rotation, which is typically on the order of a minute. In this way systematic effects occurring with a daily period can be removed to a big extent from

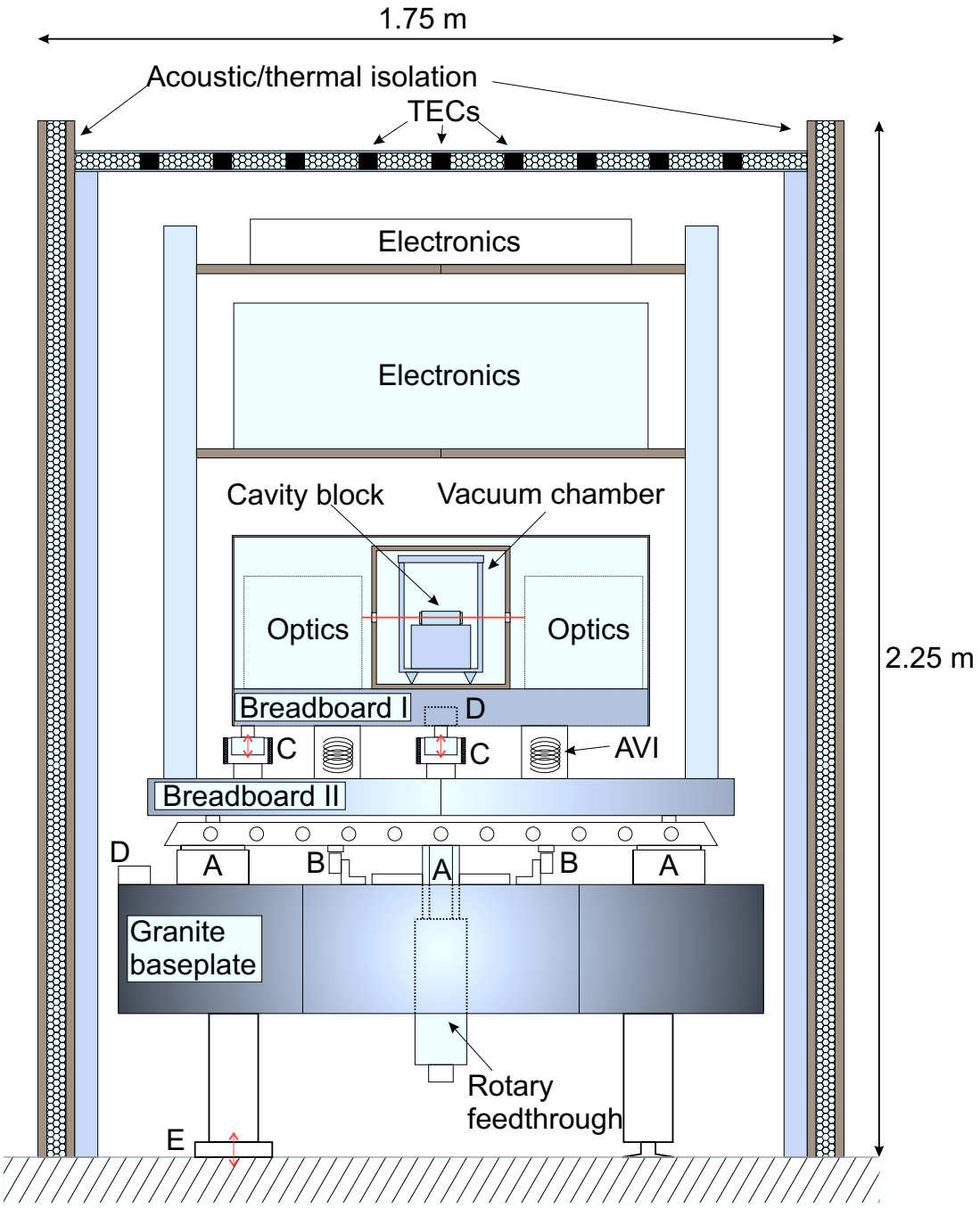

Figure 3.1.: *Cross section of the experimental setup. A: air bearings, B: piezo motors, C: voice coil actuators, D: tilt sensors, E: air spring system, AVI's: active vibration isolation supports*

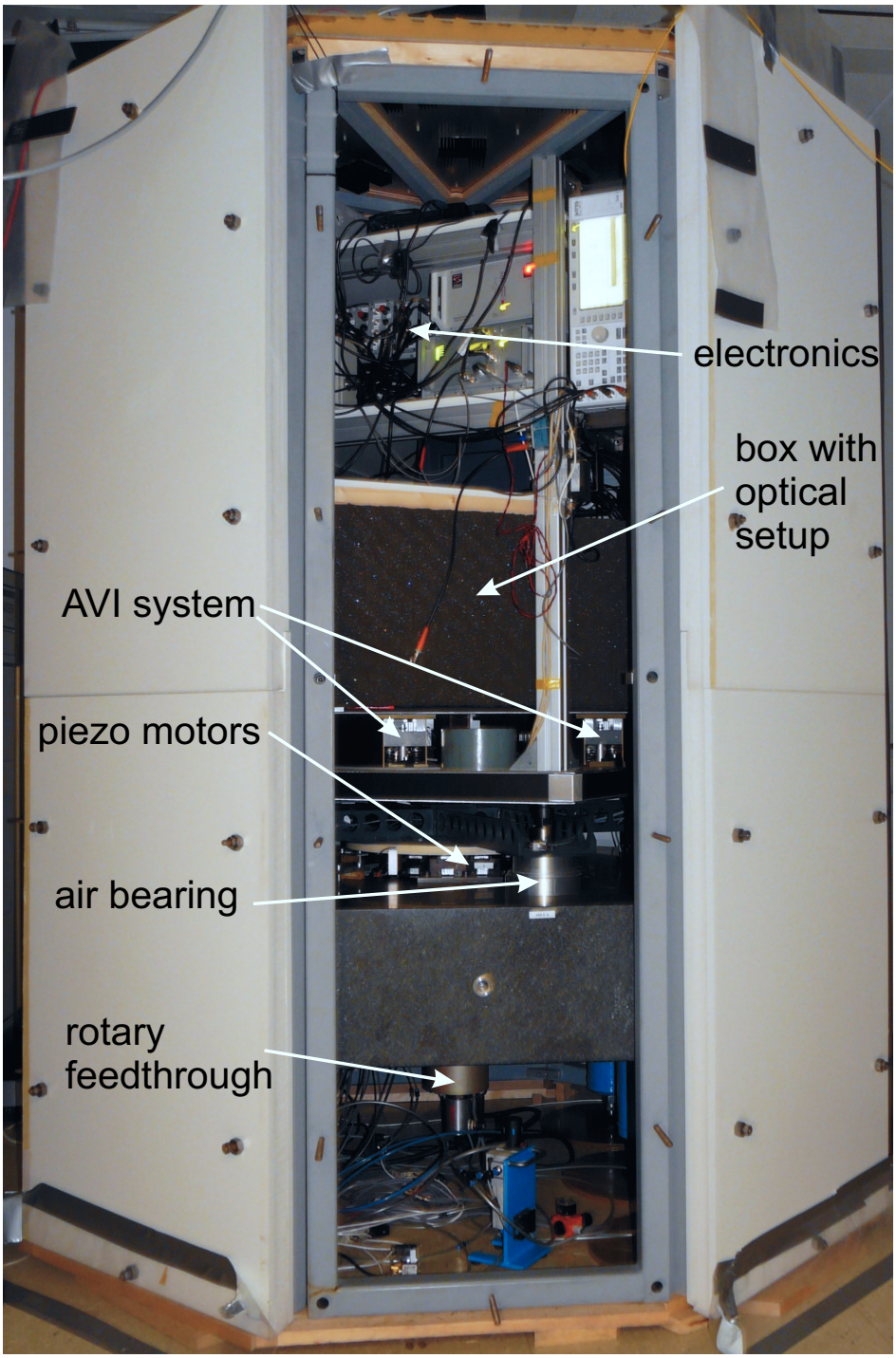

Figure 3.2.: *Picture of the experimental setup.*

the data during the evaluation process. Additionally the number of data points is enhanced by a factor of ≈ 900, allowing to decrease the statistical uncertainty by a factor of 30 as compared to a non-rotating setup (in the same timespan).
Important for the prevention of systematic effects are two systems for the stabilization of the tilt of the experimental setup. One system uses air springs and stabilizes the tilt of the rotation table baseplate to minimize the variations of the tilt of the optical system upon rotation. The second system stabilizes directly the tilt of the optical setup resting on breadboard I using electromagnetic actuators.
To avoid systematic effects occurring due to air circulation through the optics and due to strong temperature variations we have set up a tower around the whole setup (diameter 1.75 m, height 2.25 m). The sides of the tower consist of multilayer elements carried by an octagonal steel structure. The top of the tower is closed by eight triangular elements which include thermoelectric coolers (TEC's) to remove heat from the tower, which is produced by the electronical equipment. Additionally we have constructed a foam padded box around the optical setup alone.

In the following sections the main components of the experimental setup will be described in more detail.

3.2. The Optical ULE Resonators

We utilize for the first time a monolithic structure with crossed resonators made from ultra low expansion coefficient glass (ULE) for a SLIT experiment. These have, due to the design of the material, which is a of mixture of glass and polycrystalline structures, the advantage of a very small CTE at temperatures close to room temperature. Indeed the material exhibits a vanishing CTE at a particular temperature value. Keeping the resonator at this temperature would mean to decouple the resonator length from temperature changes (for small temperature fluctuations).
Since the setup can be operated completely around room temperature and doesn't need sophisticated cryogenic equipment anymore, it is a lot easier to realize a system which can be continuously rotated and acquires data at a much higher rate.
As already mentioned we use a monolithic resonator design, in which the two resonators necessary for our measurements are embedded in a single block of ULE in a crossed geometry (see fig. 3.3) allowing for a certain amount of common noise rejection, especially for thermal and vibrational noise. The block has a rectangular shape with a length and width $L_x = L_y = 84$ mm and a height of $h = 30$ mm. Cylindrical holes have been drilled through the block in a crossed shape. The block serves as spacer for the standing wave resonators which are made up by highly reflective dielectric mirrors ($\lambda_{center} = 1064$ nm, $\nu_0 = 282$ THz) with a radius of curvature of $R_{curv} = 0.5$ m and a diameter of $d = 25.4$ mm. These are optically contacted to the sides of the block, the substrate material is as well

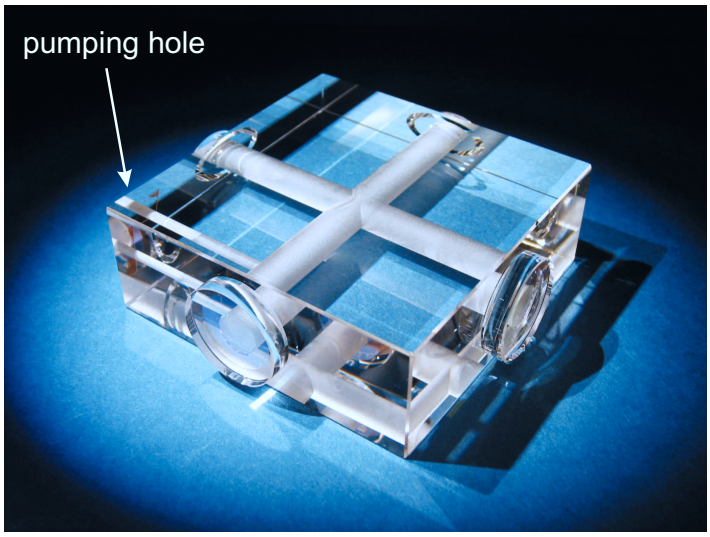

Figure 3.3.: *The dual-cavity ULE block with optically contacted mirrors and a hole for the evacuation of the block (left corner at the front). The dimensions are* $8.4 \times 8.4 \times 3.0$ *cm.*

ULE. To evacuate the cylindrical through-bores of the resonator block a small hole has been drilled (see fig. 3.3) from the side of the block, thus allowing operation of the resonators in vacuum conditions. In the case of an evacuated resonator, the resonance frequency is solely a function of the mirror distance L, its radii of curvature and the speed of light c within the resonator. For a TEM$_{lm}$-mode of the resonator it is given by

$$\nu_{res} = N \cdot \frac{c}{2L} + (l + m + 1) \cdot \frac{\Delta\zeta}{\pi} \frac{c}{2L}, \tag{3.1}$$

where N is the longitudinal mode number and the second term represents the additional curvature-dependent round trip phase shift for a Gaussian beam as compared to a plane wave (Gouy phase). The free spectral range ν_{FSR} of the cavity is given just by the mirror spacing

$$\nu_{FSR} = \frac{c}{2L} \approx 1.8 \text{ GHz}$$

and does not depend on the curvature of the mirrors. The spectral width of the resonators' resonances was measured at the very beginning of this work in spring 2005 using a frequency-doubled Nd:YAG-laser which was locked to an atomic transition in iodine via doubler free modulation transfer spectroscopy. Using an acousto-optical modulator (AOM) the laser frequency was scanned and the transmission signal was recorded. At that time the measurement showed a width of the transmission signal of $\delta\nu_{FWHM} \approx 9.5$ kHz, where a small fraction of the width is due to the linewidth of the laser locked to the transition in iodine. After the completion of the measurement cycle in spring 2009 the measurement was

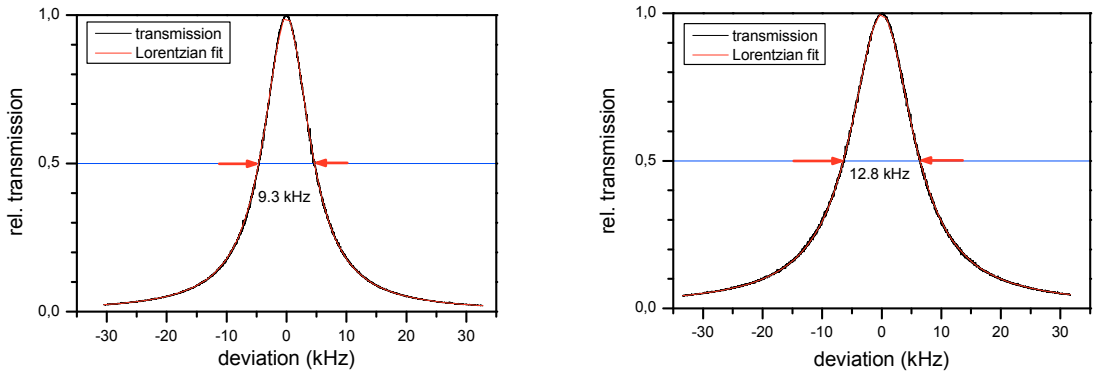

Figure 3.4.: *Transmission profiles of the resonances belonging to the TEM_{00} modes used for the measurements. Resonator 1 (left) shows a linewidth of 9.3 kHz while the linewidth of resonator 2 (right) is 12.8 kHz*

repeated. This time the laser was prestabilized to a TEM_{01} mode of a resonator and the TEM_{00} mode was scanned again by shifting the frequency of the laser beam with the help of an AOM. This new measurement (compare figure 3.4) shows a linewidth of $\delta\nu \approx 9.3$ kHz for one resonator and $\delta\nu \approx 12.8$ kHz for the other, thus indicating a slight degradation of the mirror coatings for one of the resonators. The most probable explanation for this is the accretion of material evaporated from the electrodes of the ion getter pump during late summer 2008, when a failure of the vacuum system caused a periodic switching of the ion getter pump with high currents for more than a day. After this event the throughput for the respective resonator became worse as well. However this slight degradation almost didn't influence the performance of the system. With the given linewidth values the finesses of the resonators are $F \approx 190000$, and $F \approx 141000$, respectively.

3.2.1. Thermal Expansion Coefficient

As already mentioned, ULE was chosen as material for the spacer and the substrates due to its very small thermal expansion coefficient $\alpha = L^{-1} \cdot (\partial L/\partial T)$ at room temperature and due to the fact that at a temperature T_{CTE} lying usually close to room temperature, the coefficient of thermal expansion is equal to zero. This means that any (infinitesimally) small variation of temperature does not lead to a change in the length of the spacer. For obvious reasons one would like to operate the resonators at this temperature so as to minimize systematic effects stemming from a varying temperature of the resonator block.

To determine the temperature at which the CTE equals zero we used a frequency doubled Nd:YAG-laser which was stabilized to a particular iodine line. This referenced radiation was

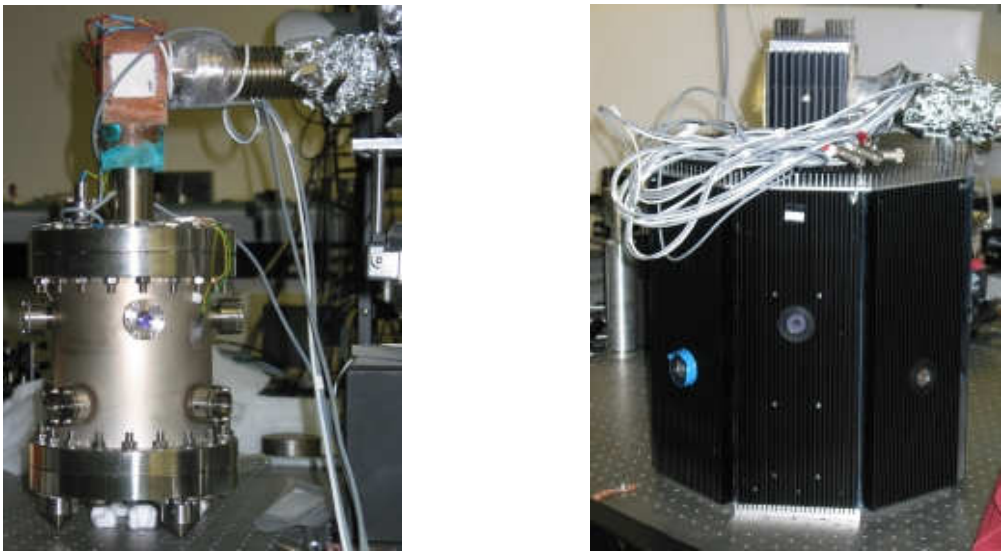

Figure 3.5.: *Left: vacuum chamber used for the measurements of the coefficient of thermal expansion. Right: the aluminum chamber, in which the vacuum chamber was placed to control the temperature of the resonators.*

coupled into the resonators with the help of an acousto-optical modulator (AOM) working as a frequency shifter. The AOM-frequency ν_{AOM} necessary to reach the resonance of the cavity is exactly the difference between the resonance frequency of the cavity and the frequency of the iodine transition. Measuring this AOM frequency as a function of the ULE-block temperature thus means to measure the resonance frequency of the cavity minus the frequency of the iodine line, which is a fixed value.

$$\nu_{res}(T_{ULE}) = \nu_{iodine} + \nu_{AOM}(T_{ULE})$$

Two ULE-blocks were tested. To control their temperature they were placed inside a vacuum chamber which was standing inside an aluminum chamber (see fig. 3.5). This chamber was made up of 8 mm thick aluminum plates, which were contacted to large heat sinks, which themselves formed a second closed chamber, via thermo-electric coolers (TEC's). Each plate could be individually stabilized in temperature. The temperature was measured with calibrated AD590 temperature sensors.
We performed this measurement for all resonators (4 resonators in 2 blocks). For each temperature the AOM frequency has been scanned and the transmission through the resonators has been recorded as a function of the frequency. Fitting a Lorentzian curve to the transmission yielded the central frequency of the resonances. The results for the shifts of these resonance frequencies as a function of temperature (relative to the starting value) are shown in figure 3.6. All resonators show first an increase in AOM frequency indicating that the length of the resonator is decreasing. The shift shows a maximum indicating that

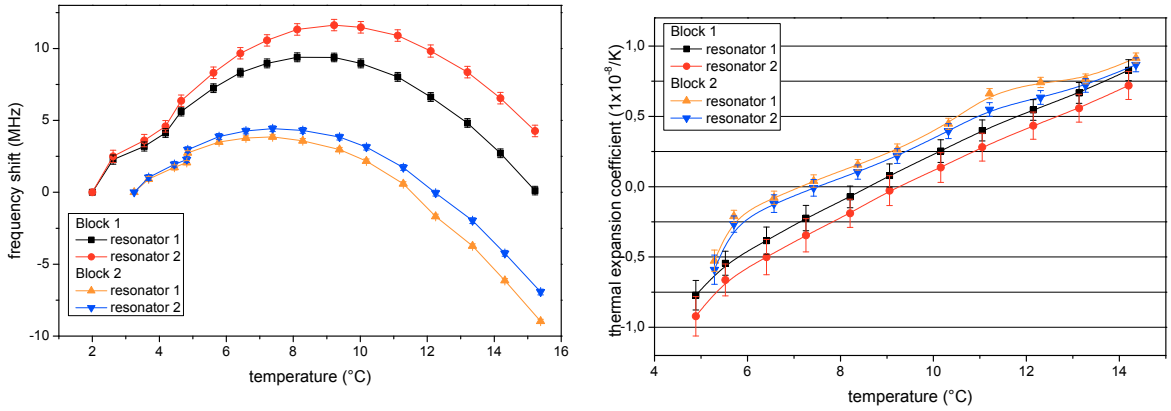

Figure 3.6.: *Left side: shift of the resonance frequencies due to variation of the resonator temperature. Right side: coefficient of thermal expansion of ULE close to the zero-crossing as derived from the measurement.*

at this temperature the resonator reached a minimal length and reflecting the vanishing of the coefficient of thermal expansion. A further increase of the temperature of the block leads to an expansion of the material and to a shift of the resonance frequencies to lower values.

From this measurement we can derive the coefficient of thermal expansion. The following relations hold:

$$\frac{\partial \nu}{\partial T} = \frac{\partial \nu_{AOM}}{\partial T} = \frac{\partial}{\partial T}\left(\frac{n \cdot c}{2L(T)}\right) = -\frac{n \cdot c}{2L^2(T)}\frac{\partial L(T)}{\partial T} = -\frac{n \cdot c}{2L(T)} \cdot L^{-1}(T)\frac{\partial L(T)}{\partial T}.$$

Simplification of these expressions yields

$$\frac{\Delta \nu}{\nu_0} = -\frac{\Delta L(T)}{L(T)}.$$

Thus the relative change in laser frequency is a direct measure for the relative change of the resonator length. Figure 3.6 shows the inferred coefficient of thermal expansion for each resonator. In the temperature range of the measurement, 4°C to 14°C, the CTE varies between $-1 \cdot 10^{-8}$ K^{-1} and $+1 \cdot 10^{-8}$ K^{-1}.

Unfortunately, the temperature for the zero CTE is not the same for the four resonators, meaning that the resonators cannot be operated simultaneously at this desired point (at least the two cavities of one block). Since our observable is the frequency difference between the resonance frequencies of two different resonators, we may calculate the shift of

the beat frequency between the resonators of one block to get more insight into the impact of this behavior on our measurements.

The differential expansion coefficient for the two cavities of one block is just the difference of the expansion coefficients of the respective resonators. The difference between the expansion coefficients is quite constant over the whole temperature range as can be seen in figure 3.6, thus within this range the differential expansion coefficient is almost constant. For one block this results in a differential shift of ≈ -320 kHz/K, for the other block it is ≈ -170 kHz/K. This means, that in fact there is no specific temperature with a minimal differential CTE we can take advantage of. Instead, for our measurement it doesn't actually matter at which temperature we operate the resonators [1]. We only have to care for a maximum stability of the block temperature to avoid huge drifts of the beat frequency due to temperature fluctuations.
Due to the fact of the rather constant differential CTE and problems with our early temperature stabilization scheme at low temperatures we decided to operate the resonators above room temperature instead, keeping their temperature at about 30°C.

3.2.2. Thermal Noise Limit

Due to thermal fluctuations in the spacer material of the cavity, in the substrates of the mirrors and in the coatings, the effective cavity length, and therefore the resonance frequency of the cavity, shows a certain amount of noise. This results in a limit for the precision, with which one can probe the resonance frequency of the cavities.
To estimate the amount of noise to be expected one can utilize the fluctuation-dissipation theorem [55], which connects the spectrum of random motion in a system with the mechanical losses. Such an analysis has been performed by Numata et al. [56]. To get information about the losses ϕ_L in different materials they performed a ring-down measurement of free oscillations to determine the quality factor $Q(= 1/\phi_L)$ of the material. For ULE their measurements yielded a value $Q = 6.1 \cdot 10^4$.
For a rough estimate of order the spacer and the mirrors with coatings are treated separately and the noise contributions are added afterwards assuming uncorrelated noise components. The contribution for the spacer is estimated to be

$$G_{Spacer}(f) = \frac{4k_BT}{2\pi f}\frac{L}{3\pi R^2 E}\phi_{Spacer},$$

where a cylindrical shape is assumed for the spacer. Although the shape does not exactly correspond to our case of a rectangular cross section, we may use this formula as an estimate and replace the cross section πR^2 of the cylinder by our cross section $A = w \times h$. This will

[1] For reasons of frequency stabilization it is still desirable to have only small excursions of the absolute frequency and thus a small CTE.

not falsify the final result too much since the contribution of the spacer material is only about 10-20% [56] for the ULE case. In the formula given $G(f)$ is the one-sided power spectrum of length fluctuations, k_B is the Boltzmann constant, T the temperature, ω the angular frequency of the fluctuation, L the length of the cavity and E is Young's modulus. Assuming a temperature $T = 300$ K $\cong 30°$C and using the ULE-values from [56] we get $\sqrt{G_{Spacer}} = 2.7 \cdot 10^{-18}$ m/$\sqrt{\text{Hz}}$ at 1 Hz.
For the mirrors one can derive an estimate for the power spectrum as [56]

$$G_{mirror}(f) = \frac{4k_BT}{2\pi f}\frac{1-\sigma^2}{\sqrt{\pi}Ew_0}\phi_{sub},$$

where σ is Poisson's ratio, w_0 the beam radius on the mirror and ϕ_{sub} is the loss of the substrate. For a decreasing beam radius the thermal noise is increasing, due to the fact that the effective surface on which thermal fluctuations might average out is decreasing. Since the coating of the mirror is introducing losses as well, one has to multiply this formula with a correction factor:

$$\left(1 + \frac{2}{\sqrt{\pi}}\frac{1-2\sigma}{1-\sigma}\frac{\phi_{coat}}{\phi_{sub}}\frac{d}{w_0}\right),$$

where d is the coating thickness and ϕ_{coat} are its losses. Using the parameters of our resonators we get a mirror contribution of $\sqrt{G_{mirror}} \approx 4 \cdot 10^{-17}$ m/$\sqrt{\text{Hz}}$ at 1 Hz. For one resonator the overall length fluctuations are thus given by $\sqrt{G_{tot}} = \sqrt{2 \cdot G_{mirror} + 2 \cdot G_{Spacer}} \approx 6 \cdot 10^{-17}$ m/$\sqrt{\text{Hz}}$. Since we are dealing with two resonators when measuring the frequency difference we have to multiply this value with $\sqrt{2}$. Then we can derive the amount of frequency noise in the beat, since

$$\sqrt{G_{L,tot}}/L = \sqrt{G_{\nu,tot}}/\nu_0.$$

This yields for our resonators a value of $\sqrt{G_{\nu,tot}} \approx 0.3$ Hz/$\sqrt{\text{Hz}}$ at 1 Hz. This spectral density of frequency fluctuations drops as $f^{-1/2}$ with increasing frequency of the fluctuations. From the spectral density we can derive a lower limit for the frequency stability of the beat frequency as described by the Allan deviation (see appendix A). For a constant Allan deviation σ_y the mathematical relation

$$\sqrt{G(f)} = \sigma_y\nu/\sqrt{2\ln 2 \cdot f}$$

holds and we can derive a lower limit of $\sigma_y \approx 1.3 \cdot 10^{-15}$ for the relative Allan deviation of the beat, corresponding to an absolute Allan deviation of approximately 0.4 Hz for radiation with a frequency $\nu = 2.82 \cdot 10^{14}$ Hz.

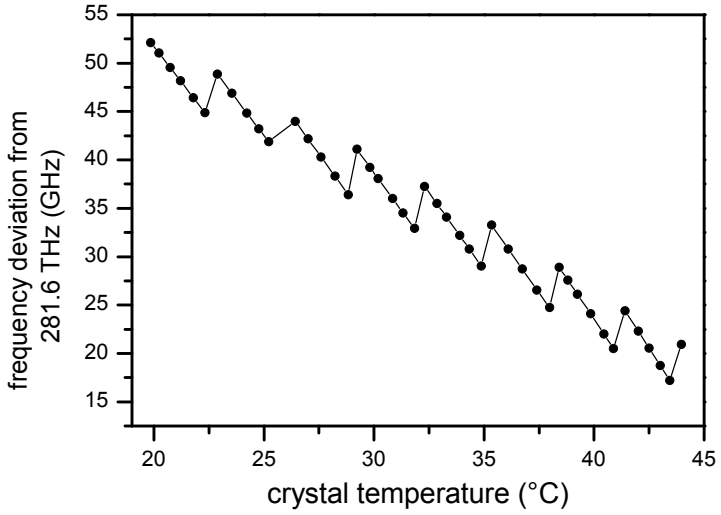

Figure 3.7.: *Dependence of the center frequency of the Nd:YAG laser output on the laser crystals temperature*

3.3. Frequency Stabilization

3.3.1. The Laser Source

To interrogate the resonance frequencies of the resonators a single Nd:YAG-laser is used. It is the commercially available diode-pumped monolithic non-planar ring oscillator Nd:YAG-laser [57] "Mephisto" produced by Innolight GmbH (Hannover).
It has a maximum output power of ≈ 100 mW emitted at a center wavelength of $\lambda_0 = 1064$ nm. For the free-running laser the linewidth of the emitted radiation is in the range of several kHz. The center frequency of the emitted radiation can be controlled via a piezoelectric crystal glued to one facet of the NPRO laser crystal and via its temperature. Via the piezo the frequency can be tuned by $\approx \pm 160$ MHz by applying voltages in the range of ± 100 V, the tuning coefficient is thus ≈ 1.6 MHz/V. The modehop-free tuning range for control via the temperature is ≈ 10 GHz with a tuning coefficient of ≈ 3.6 GHz/K and a sensitivity of the modulation input of 1 K/V. Tuning the crystal temperature between 20°C and 43°C yields a variation of the lasers frequency of ≈ 35 GHz as has been measured with a wavemeter (see figure 3.7).

Since we can use only one laser for two cavities we have to split the emitted radiation into two parts which can be independently locked to resonances of the resonators. It is obvious, that we can realize only one servo system via the piezo and the crystal tempera-

ture. To have almost identical servo systems for the two resonators we therefore decided to use a two-stage stabilization scheme. For this scheme we have to split the output of the laser into three beams. Two of the beams are used to interrogate the TEM_{00}-modes of the resonators, while the third beam is used to prestabilize the Nd:YAG-laser on a neighboring TEM_{01} mode of one of the resonators. The resonance frequency of this mode shows almost the same behavior as the ones of the TEM_{00} modes under variation of the temperature and under tilt of the resonator block. Thus locking to this mode strongly reduces the amount of noise which has to be canceled by the so called fine locks.

Figure 3.8 shows the complete optical scheme of the frequency stabilization system. The output of the Nd:YAG-laser at a frequency ν_L is split into three beams with shifted frequencies using the acousto-optical modulators AOM 1, AOM 2 and AOM 3. AOM 1 and AOM 2 are driven by frequency synthesizers (Hewlett-Packard E4420B) which allow for a varying RF-power and frequency, thus making it possible to control the frequency and power of the respective beams. AOM 1 shifts the frequency by $\approx +130$ MHz, AOM 2 by ≈ -112 MHz. AOM 3 is driven by a fixed frequency RF-driver with a base frequency of ≈ 370 MHz and a variable power output. It is operated in a double pass configuration, resulting in a total frequency shift for the laser beam of $\approx +740$ MHz. The frequency values for the AOM's have been chosen like this to reach the resonance frequencies of two TEM_{00} modes and a TEM_{01} mode of the resonators as shown in figure 3.9. The polarization of the two beams generated by AOM 1 and AOM 2 lies in the plane of the optical breadboard, while the polarization of the beam generated by AOM 3 is rotated by 90° and is normal to the plane of the breadboard.
Thus beams number 1 and 3 can be independently coupled into the same resonator via a polarizing beamsplitter cube (PBS) and can be stabilized to different modes of the resonator. The light of these two beams transmitted through the resonator is split again using a PBS and detected on two photodiodes. To fix the polarization of beam number 2 it is as well coupled into the second resonator via a PBS. Fixing the polarization via this procedure eliminates possible shifts of the resonance frequencies, which might occur due to birefringence of the mirrors and imperfections of their surfaces [58, 59].
For beam number 3, which serves for the prestabilization of the laser frequency, an electro-optical modulator is used for a modulation of the phase of the beam. This is necessary for the locking scheme applied for the prestabilization. After being frequency shifted by AOM 3 the beam is coupled into the resonator. Part of the beam is reflected back from the resonator and hits after reflection by a 50% beam splitter plate the fast photodiode P3 which is used for the derivation of the error signal for the prestabilization. The photodiodes P1, P2 and P4 behind the resonators detect the transmitted light and serve two purposes. For the beams 1 and 2 they are used for the frequency stabilization using a transmission lock scheme, where via an AC-component of the photocurrent an error signal is derived. Furthermore, the DC component of the photocurrent is used to stabilize the power circu-

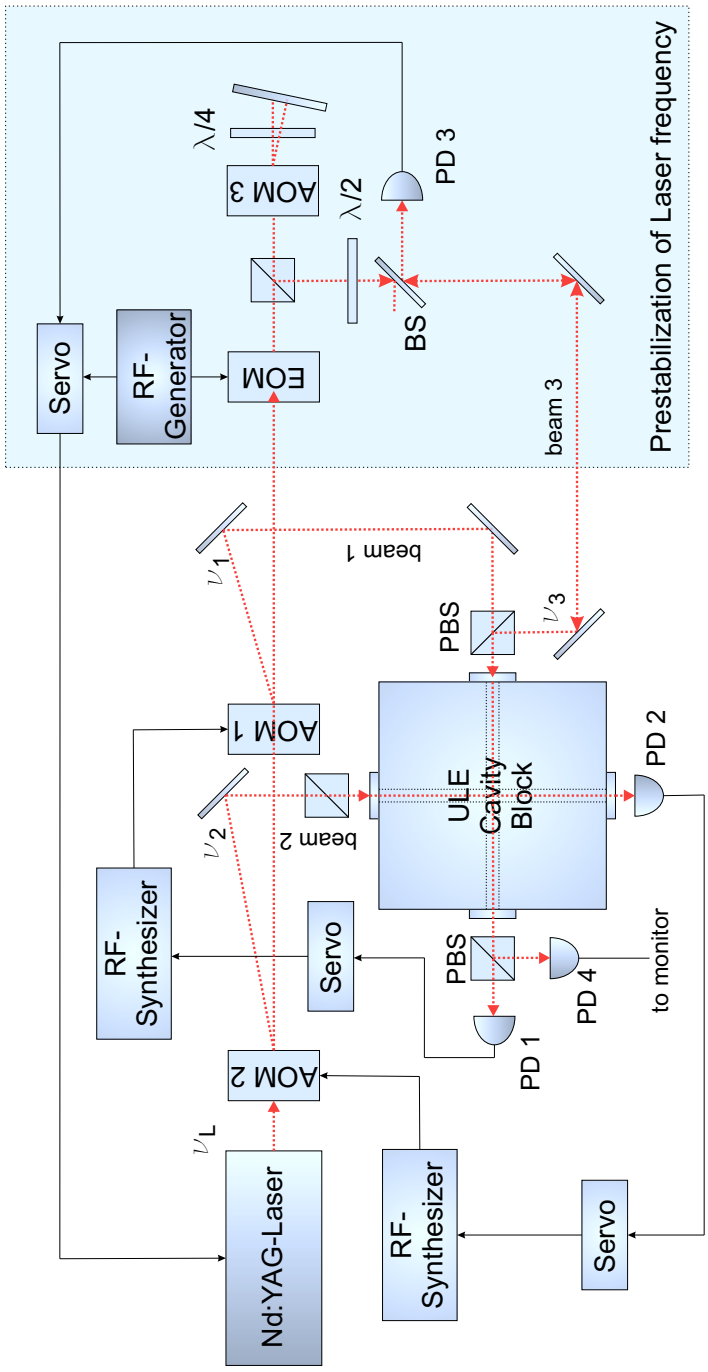

Figure 3.8.: *Optical scheme of the experimental setup. By means of AOMs the radiation of a single Nd:YAG-laser is split into 3 different beams, which are individually frequency stabilized to different modes of the resonators.*

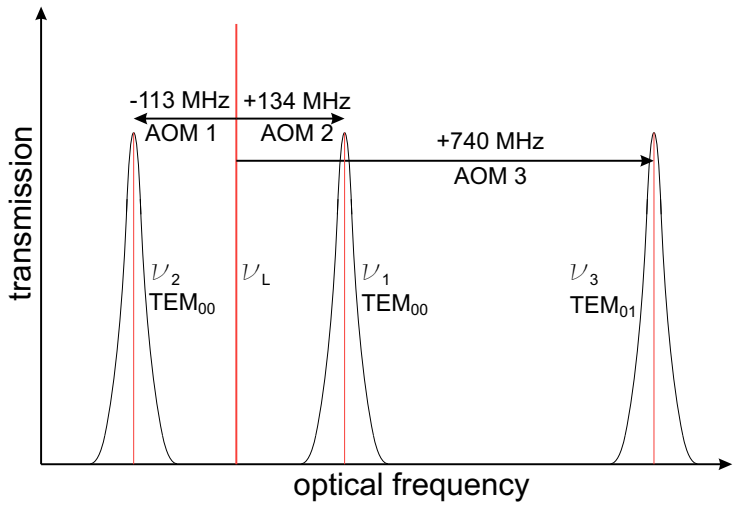

Figure 3.9.: *Shift of the optical frequency caused by the AOMs relative to the laser frequency.*

lating within the resonator.

To measure the frequency difference between the two TEM$_{00}$ modes it is necessary to produce a beat between the two beams on a fast photodiode, yielding directly $\nu_b = \nu_1 - \nu_2$. This has been done in an early stage of the development of the apparatus. However, as has just been shown, the frequency of beam 1 is $\nu_1 = \nu_L - \nu_{AOM1}$, and for beam 2 we have $\nu_2 = \nu_L + \nu_{AOM2}$. The optical beat frequency corresponds therefore to

$$\nu_b = \nu_1 - \nu_2 = (\nu_L + \nu_{AOM1}) - (\nu_L - \nu_{AOM2}) = \nu_{AOM1} + \nu_{AOM2}.$$

Thus instead of measuring the optical beat between beam 1 and 2 we can measure the sum of the driving frequencies of the corresponding AOM's, which can be realized very easily electronically. It has been verified at the beginning of our measurements that both ways yield the same result with the optical beat having the identical center frequency and an almost identical linewidth. Therefore for all further measurements we decided to use the electronic scheme.

3.3.2. Basics of Control Loops

The basic layout of a control loop for active frequency stabilization of a laser to a reference is shown in 3.10. The basic theory behind this feedback system can be found in [60] or in books about control theory. The frequency ν_L of the laser, which is disturbed by frequency noise with a spectral density $S_{f,L}$ $[Hz/\sqrt{Hz}]$, is the controlled variable. The frequency noise described by $S_{f,L}$ can have several sources: vibrations of the laser, temperature fluctuations inside the laser, fluctuations of the current of the pump diodes, et cetera. The

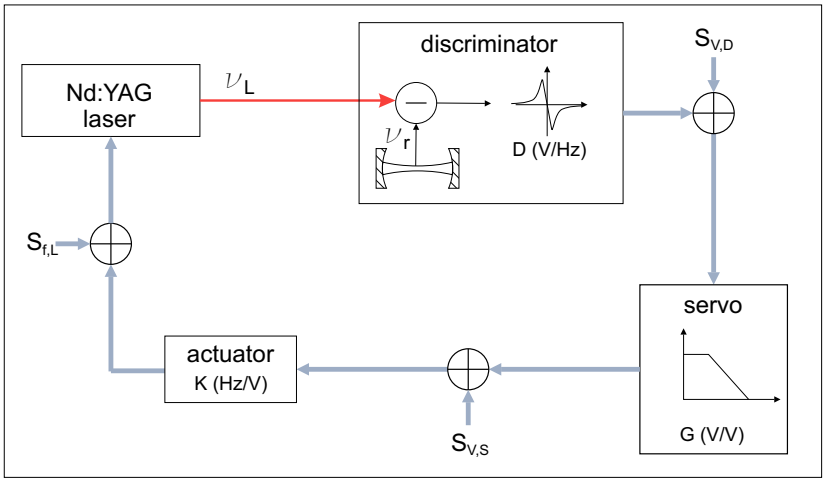

Figure 3.10.: *Block diagram of the control loop applied in the frequency stabilization of lasers*

laser frequency is continuously compared with the resonance frequency ν_r of the resonator, which serves as a frequency discriminator[2]. It converts frequency fluctuations of the laser, which lead to a deviation $\delta\nu = \nu_L - \nu_r$ from the resonance frequency of the resonator, into voltage fluctuations $x = D \cdot (\nu_L - \nu_r)$. Here the quantity D [V/Hz] is the slope of the discriminator, which is generally a function of the Fourier frequency of the frequency fluctuation, x is the so called error signal. Of course the discriminator itself can inherently inhibit some noise as well, leading to voltage noise with a spectral density $S_{V,D}$ $[V/\sqrt{Hz}]$, which adds to the error signal.

The error signal is fed into a servo system, where it is processed with a complex and frequency dependent transfer function G [V/V]. The servo itself is naturally not a perfect device, thus adding another voltage noise component $S_{V,S}$ to the total noise of the control loop. The output signal of the servo controls an actuator, which converts the given voltage fluctuations back into fluctuations of the laser frequency with a conversion factor K [Hz/V], pushing the frequency of the laser back towards the resonance frequency of the resonator. Elements which can be used as actuator are e.g. piezos glued to the laser crystal, temperature control of the laser crystal, AOM's in the beam path and EOM's inside the laser cavity.

Schawlow-Townes-Limit, Quantum Noise Limit As has been mentioned, the total noise in the feedback loop consists of contributions from the laser (including the noise from the actuators, which cannot be separated from the laser noise itself), from the discriminator and the servo system. The noise $S_{f,L}$ of the laser frequency can have several origins, but there exists a lower limit originating from the working principle of the laser. Though the laser

[2]Of course other frequency references can be used as a discriminator, e.g. atomic transitions.

works via the process of stimulated emission, spontaneous emission will always happen from time to time, adding incoherently photons to the laser field and thus randomly perturbing the phase of the carrier field. This process has been analyzed theoretically by Schawlow and Townes [61].
The spectral density of the frequency noise $S_{f,ST}$ associated with the described quantum noise process shows white behavior, meaning that the spectral density does not depend on the Fourier frequency of the fluctuation, and is given by

$$S_{f,ST} = \delta\nu_{LR} \cdot \sqrt{\frac{2h\nu_L}{P_{out}}}. \tag{3.2}$$

Here $\delta\nu_{LR}$ is the linewidth of the laser resonator in the absence of radiation and P is the output power of the laser. The strength of the effect clearly depends on the amount of spontaneous photons relative to the number of coherent photons, thus the scaling with the square root of the inverse power.
For free-running lasers this limit is never reached over the complete spectral range, since especially in the range below 100 kHz technical noise dominates the noise spectral density. Fluctuations in the pump power of the diode lasers e.g. lead to a contribution proportional to $1/f^{\alpha}$ dominating the noise spectral density at low frequencies together with effects from mechanical vibrations induced from the surrounding and through acoustics.

Active Feedback If the loop is closed, active frequency control is applied and the spectral noise density can be suppressed over the bandwidth of the control loop, even below the Schawlow-Townes limit. However all the noise sources apparent in the loop are added to the frequency noise originating from the laser, resulting in a total closed loop noise spectral density of frequency fluctuations [60]

$$S_{f,cl} = \frac{\sqrt{S_{f,L}^2 + |K \cdot S_{V,S}|^2 + |KG \cdot S_{V,D}|^2}}{|1 + KGD|}. \tag{3.3}$$

Obviously, for very large gain of the servo system it is possible to almost eliminate the effect of the contributions from $S_{f,L}$ (laser) and $S_{V,S}$ (servo) and one is left with the effect of the discriminator noise directly determining the spectral noise of the laser frequency,

$$S_{f,cl\ min} = \frac{S_{V,D}}{D}. \tag{3.4}$$

This means that the laser is perfectly tracking the reference defined by the discriminator for a sufficiently high gain and bandwidth of the servo system. Still, the discriminator can define a somewhat noisy reference since technical noise associated with the discrimination technique and of the amplifiers used for the production of the error signal are included in

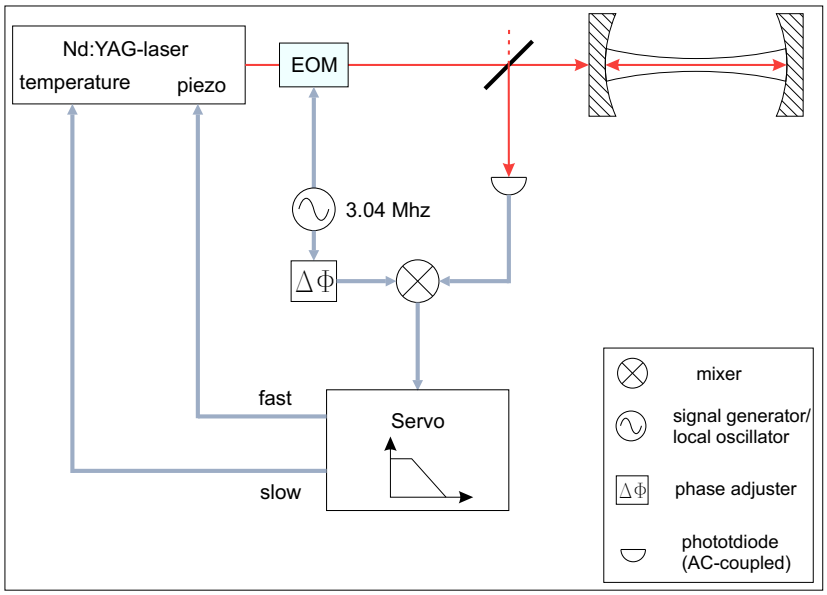

Figure 3.11.: *Principal optical layout of the Pound-Drever-Hall frequency stabilization system.*

the error signal. This can be minimized by making the slope of the discriminator as steep as possible, which for resonators implies a linewidth $\Delta\nu_r$ as narrow as possible, and by minimizing the electronical noise by using the appropriate components.

3.3.3. Prestabilization, Pound-Drever-Hall-Lock

As already mentioned earlier, we use a two stage scheme for the locking of the lasers frequency to the resonance frequencies of the resonators. For the prestabilization we use a scheme, which was developed for microwave applications by R.V. Pound [62] and was later applied as well in the optical range of the electromagnetic spectrum by R. Drever, J.L. Hall and others [63]. Therefore this scheme is commonly referred to as Pound-Drever-Hall scheme (PDH). A sketch of the principal optical layout is given in figure 3.11, for an theoretical introduction to the technique and some applications one may consult e.g. [64, 65, 66, 60, 67]. Here only a short description of the technique will be given.

The output of the Nd:YAG laser with an angular frequency ω_L is phase-modulated

$$\Delta\phi(t) = \beta \sin \Omega t$$

by means of an electrooptical modulator (EOM) with a modulation frequency $\Omega = 2\pi \cdot 3.04$ MHz. After the EOM the beam can be written as a linear superposition of an infinite number

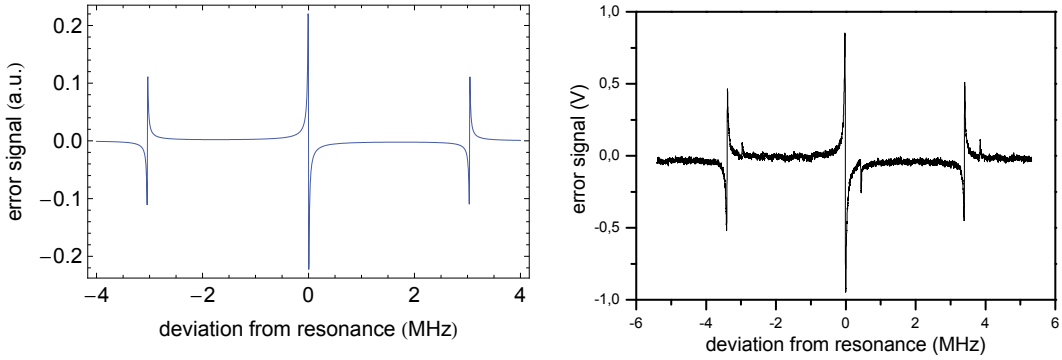

Figure 3.12.: *Error signal of the Pound-Drever-Hall frequency stabilization scheme when scanning over the resonance. Left side: calculated error signal. Right side: error signal as measured in our experimental setup for the prestabilization to a TEM_{01} mode. The additional peaks arise due to the TEM_{10} mode, which is separated by ≈500 kHz.*

of beams

$$\begin{aligned} E_{inc}(t) &= E_0 e^{-i(\omega_L t+\beta\sin\Omega t)} \\ &= E_0 \sum_{k=-\infty}^{\infty} J_k(\beta) e^{-i(\omega_L+k\Omega)t} \\ &\approx E_0[J_0(\beta)e^{i\omega t} + J_1(\beta)e^{i(\omega+\Omega)t} - J_1(\beta)e^{i(\omega-\Omega)t}], \end{aligned} \tag{3.5}$$

where usually only the terms of first order in Ω contribute significantly to the total power of the beam. The terms $J_n(\beta)$ are the n-th order Bessel functions[3] of the first kind. Thus the phase modulation produces sidebands to the carrier frequency at $\omega_L \pm \Omega$ with the amplitude depending on the quantity β known as the modulation index. Now if this beam impinges on the resonator each frequency component can be treated independently and has to be multiplied with the corresponding amplitude reflection coefficient $F(\omega)$, $F(\omega \pm \Omega)$ to derive the reflected beam. The amplitude reflection coefficient for a symmetric cavity without (intracavity) losses can be written as

$$F(\omega) = \frac{r(e^{i\phi} - 1)}{1 - r^2 e^{i\phi}} \tag{3.6}$$

where r is the amplitude reflection coefficient of the cavity's mirrors (≈ 1 in our case) and ϕ is the phase shift of the beam acquired during one round trip in the cavity $\phi = 2\pi\nu_L/\nu_{FSR}$.

[3] $J_n(\beta) = \sum_{k=0}^{\infty} \frac{(-1)^k(\beta/2)^{n+2k}}{k!\Gamma(n+k+1)}$ with $\Gamma(n+k+1) = \int_0^{\infty} x^{n+k+1}e^{-x}dx$.

The reflected beam is then detected on a fast photodetector (bandwidth $>$ modulation frequency), where beating between the sidebands with power P_S and the carrier with power P_C will occur, resulting in a signal which is amplitude modulated at the frequency of the original phase modulation (and other components) with the amplitude and the phase relative to the original modulation depending on the detuning from the cavities resonance frequency. The AC-output of the fast photodetector is fed into the RF-input of a double-balanced mixer (ZAD-3A) and is mixed with the signal which has been used for the production of the sidebands. The output of the mixer will show a DC-signal that vanishes exactly for the laser frequency on resonance, $\nu_L = \nu_r$, and has opposite polarity for the two sides of the resonance[4].

$$\epsilon = 2\sqrt{P_C P_S}\Im\left[F(\omega)F^*(\omega+\Omega) - F^*(\omega)F(\omega-\Omega)\right] \tag{3.7}$$

The form of this resulting "error signal" is shown in 3.12. On the left side a calculation of the error signal is shown, while the right graph displays the error signal as measured in our setup. The central feature of the error signal has a steep slope D_V ≈2V/10kHz=100 μV/Hz close to the resonance of the resonator. In our case an additional peak arises (see fig. 3.12) due to the TEM_{10} mode, which due to imperfections of the mirror substrate is not degenerate as described by equation 3.1, but separated by ≈ 500 kHz. By alignment it can be almost completely supressed. Since this lock is only used for prestabilization, potential shifts of the lock point, which might arise due to a varying alignment or laser power, will not lead to systematic effects as the finelocks keep the respective laser frequency on resonance. The output of the mixer is amplified by the servo system with a complex and frequency dependent gain $G(\omega)$. The bandwidth of the fast output of the servo system driving the piezo actuator is limited to about 30 kHz to avoid the excitation of mechanical resonances of the piezo. The bandwidth of the slow output controlling the temperature of the laser crystal has been set to 0.1 Hz. Furthermore the possible bandwidth of the system is limited by the resonators, since these realize a low pass filter with the cutoff frequency on the order of the linewidth.

3.3.4. Finelocks in Transmission

For fine locking of the two measurement beams we choose a transmission locking scheme. As already mentioned earlier, the resonance of the cavities can be described by a Lorentzian lineshape (see fig. 3.13)

$$\begin{aligned} L(\omega_L) &= \frac{(\Delta\omega/2)^2}{((\omega_0-\omega_L)^2+(\Delta\omega/2)^2} \\ &= \frac{1}{1+\frac{(\omega_0-\omega_L)^2}{(\Delta\omega/2)^2}}. \end{aligned} \tag{3.8}$$

[4]Additionally AC components arise which are removed by means of a lowpass filter.

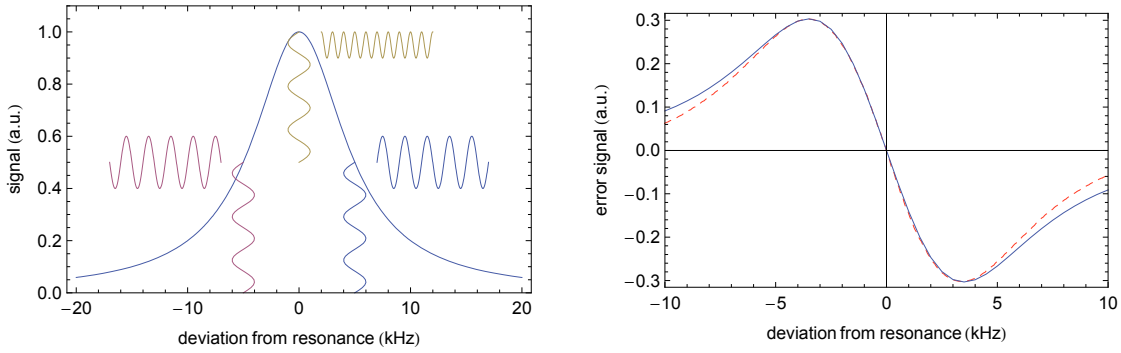

Figure 3.13.: *Working principle of the transmission lock (left). On resonance the frequency modulation leads to intensity modulation at 2Ω, while off resonance the modulation is primarily at Ω. Right: calculated error signal (intensity modulation amplitude at Ω in the approximation of small frequency modulation amplitudes) and measured error signal (dashed). The amplitudes were scaled to yield the same maximum.*

In a simplified treatment one could think of the lock working like shown in figure 3.13. A modulation of the laser frequency $\omega_L = \omega_{L0} + \delta\omega_L \sin \Omega t$ will lead, neglecting effects due to the long lifetime of the photons in the resonator compared to the period of modulation, to a modulation of the intensity of the transmitted light according to

$$\begin{aligned} I(t) &= I_0 \cdot L(\omega_L(t)) \\ &= \frac{1}{1 + \frac{(\omega_0 - \omega_{L0} - \delta\omega_L \sin \Omega t)^2}{(\Delta\omega/2)^2}}. \end{aligned} \tag{3.9}$$

If the mean laser frequency ω_{L0} equals the resonance frequency of the resonator the transmitted intensity will be modulated primarily at twice the modulation frequency, though higher (even) harmonics of the modulation frequency appear as well. The situation is different when the laser frequency is probing one of the wings of the transmission profile. Then the transmitted intensity will show a modulation primarily at the modulation frequency itself since the wings exhibit an almost linear slope for small modulations. Figure 3.13 illustrates this behavior. On the two wings of the resonance one obtains a modulation of the intensity at Ω. The phase of the intensity modulation relative to the frequency modulation depends on which wing is probed and differs by 180° for the two cases. Thus, a phase sensitive detection of the intensity modulation at the modulation frequency can be used to derive an error signal. This is shown on the right side of figure 3.13, where the magnitude of the component in phase with the modulation frequency is given as a function of the detuning of the laser. Close to the resonance the agreement between the calculation (solid) and the measured signal (dashed) is very good. However, for deviations bigger than ≈ 4 kHz from the resonance the measured signal drops faster than the calculated one.

A more detailed analysis follows the same route as the discussion of the Pound-Drever-Hall lock. For the frequency modulation of the laser beam we use a sinusoidal signal. Thus, our frequency modulation scheme is equivalent to the phase modulation of the PDH lock, since

$$\begin{aligned} E(t) &= E_0 \cdot e^{i\int_0^t(\omega_{L0}+\delta\omega\cos\Omega t')dt'} && (3.10)\\ &= E_0 \cdot e^{i\omega_{L0}t+\beta\sin\Omega t}. && (3.11)\end{aligned}$$

Here $\beta = \frac{\delta\omega}{\Omega}$ is again the modulation index, which in our case is approximately 1.2. Again one can use the expansion of the electric field already given in section 3.3.3. For our transmission locking scheme we now have to use the complex transmission coefficient of the cavity to derive the electric field after the resonator. This transmission coefficient is, assuming again a symmetric cavity without losses, given by

$$T(\nu_L) = \frac{(1-r^2)e^{i\pi\nu_L/\nu_{FSR}}}{1-r^2e^{2i\pi\nu_L/\nu_{FSR}}}. \quad (3.12)$$

The phase factor $\frac{2\pi\nu_L}{\nu_{FSR}}$ is the round-trip phase shift for a laser beam with frequency ν_L circulating in the resonator. Using the expansion of the electric field and the given transmission coefficient, the transmitted field can be derived as

$$\begin{aligned} E_{trans}(t) &= E_0\sum_{k=-\infty}^{\infty} J_k(\frac{\delta\omega}{\Omega})e^{-i(\omega_{L0}+k\Omega)t}\cdot\frac{(1-r^2)e^{i(\omega_{L0}+k\cdot\Omega)/2\nu_{FSR}}}{1-r^2e^{i(\omega_{L0}+k\cdot\Omega)/\nu_{FSR}}}\\ &\approx E_0\cdot[J_0(\frac{\delta\omega}{\Omega})\cdot\frac{(1-r^2)e^{i\omega_{L0}/2\nu_{FSR}}}{1-r^2e^{i\omega_{L0}/\nu_{FSR}}}+J_1(\frac{\delta\omega}{\Omega})\cdot\frac{(1-r^2)e^{i(\omega_{L0}+\Omega)/2\nu_{FSR}}}{1-r^2e^{i(\omega_{L0}+\Omega)/\nu_{FSR}}}\\ &\quad +J_{-1}(\frac{\delta\omega}{\Omega})\cdot\frac{(1-r^2)e^{i(\omega_{L0}-\Omega)/2\nu_{FSR}}}{1-r^2e^{i(\omega_{L0}-\Omega)/\nu_{FSR}}}+.....]. \quad (3.13)\end{aligned}$$

Here the first three sidebands contribute considerably to the overall power. Their amplitude is given by the value of the Bessel functions of first kind: $J_0(1.2) = 0.67$, $J_1(1.2) = 0.50$, $J_2(1.2) = 0.16$ and $J_3(1.2) = 0.03$. A photodiode positioned behind the resonator detects the power transmitted through the resonator. Thus, again we have to square the calculated electric field $E_{trans}(t)$ to derive the current produced by the phodiode. We get constant terms giving the average power detected by the photodiode and additional terms at the modulation frequency due to the beating between the sidebands and the carrier. Furthermore, we get terms due to the beating of the sidebands with each other at a frequency of 2Ω and 3Ω.
From the signal at Ω we derive, as in the case of the Pound-Drever-Hall lock, the error signal used for the stabilization of the laser to the resonance frequency of the cavity. Figure 3.14 shows the error signal using all terms containing sidebands up to the third order

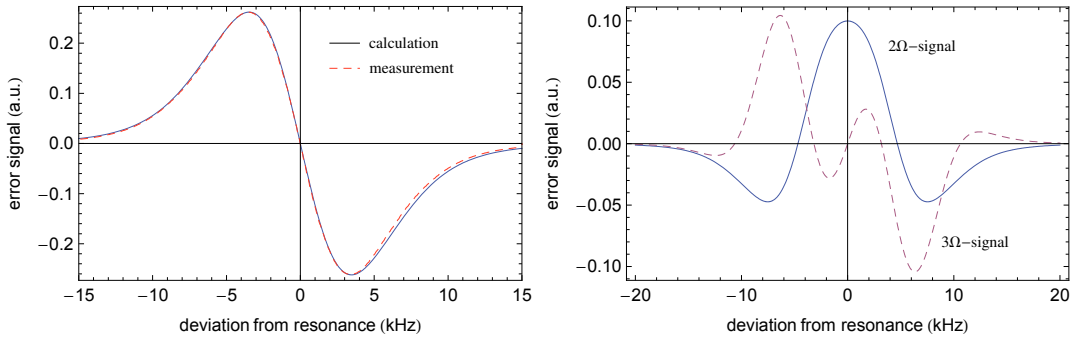

Figure 3.14.: *Left: Error signal calculated using all contributions up to the third order sideband. The measured error signal (dashed) matches the calculated curve well after scaling of the amplitudes. Right: Calculated signals at higher harmonics of the modulation frequency Ω. The signal at 3Ω has been multiplied by a factor of 6 to enable a better display.*

together with the measured error signal in our setup, where the amplitude has been scaled to the same maximum. The measured signal almost perfectly fits the calculated shape.

The servo system developed for the finelocks synchronously detects the modulations which are in phase with the modulation signal yielding the shown error signal. To be able to compensate for phase shifts within the loop the relative phase between the reference signal (signal used for frequency modulation) and the intensity modulation can be adjusted to yield a maximum discriminator slope. To avoid any parasitic influence of the second harmonic on the locking system a notch filter with small width of the stop band has been installed within the lockbox to remove this component of the intensity modulation. The signal at 2Ω has its maximum amplitude directly on resonance and falls off to the sides of the resonance. Furthermore a lowpass filter removes higher harmonics of the modulation frequency, especially the third harmonic, which vanishes directly on resonance (see fig. 3.14), but could give a oscillating contribution to the error signal when being off resonance, thus disturbing the frequency lock.

It has already been mentioned, that the resonators act like lowpass filters with a cut-off frequency in the range of the linewidth, which is in our case about 10 kHz. Thus we choose modulation frequencies for our finelocks below this limit. To avoid a possible cross-contamination between the two locking systems we choose two different modulation frequencies in the audio range. The lock to resonator A uses $\Omega = 2\pi \cdot 3.4$ kHz, while the lock to resonator B uses $\Omega = 2\pi \cdot 4.08$ kHz.
For obvious reasons the bandwidth of the servo system for the finelocks should be smaller than the modulation frequency itself. In our case the bandwidth is ≈ 500 Hz.

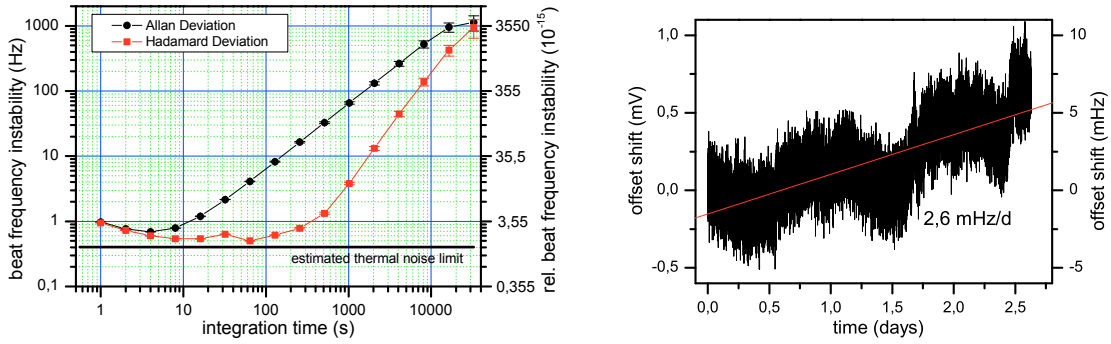

Figure 3.15.: *Left: Allan deviation and Hadamard deviation of the beat frequency between the resonators for the rotating setup. Results for the stationary setup are almost identical, except the non-existence of the bump at approximately half the rotation period (32 s). Right: Drift of the lock offset over the course of a few days. The drift is on the order of 2.6 mHz per day.*

As actuators for the stabilization of the optical frequency and for the frequency modulation we use AOM 1 and AOM 2. The servo systems control the frequency of the RF-output of the driving synthesizers via an integrated frequency modulation (FM) input. To the control voltage of the servo system, which keeps the laser frequency on resonance, we add the AC-signal leading to the frequency modulation. This signal is fed into the FM input of the synthesizer.

Figure 3.15 shows on the left the stability of the beat frequency resulting from the described frequency stabilization scheme upon rotation of the setup. The Allan deviation is at a level of 1 Hz at an integration time of 1 s. For longer integration times the instability first drops, then the effect of beat frequency drifts leads to an increase in the instability. Using the Hadamard deviation one can remove the effect of a linear drift. This measure of instability first drops, reaches a bottom of ≈ 0.6 Hz and rises again for integration times well above the period of rotation. However, the Hadamard deviation shows a bump at approximately half the period of rotation, indicating a residual modulation at the period of rotation. This is not the case for the nonrotating system. The minimum value of the Hadamard deviation is slightly above the thermal noise limit estimated for our resonators. The right side of figure 3.15 shows the drift of the lock offset leading to a shift of the lockpoint of the frequency stabilization system. The effect of the drift is on the order of a few mHz per day and thus negligible.

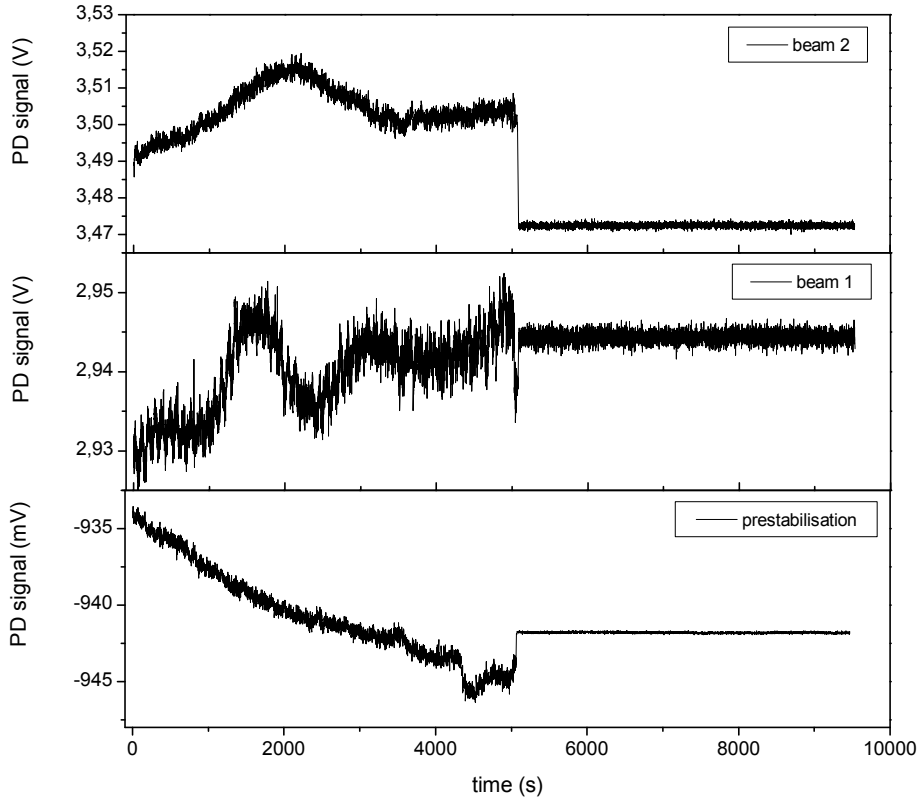

Figure 3.16.: *Effect of the active feedback on the stability of the laser power transmitted through the resonators. Short term fluctuations are slightly reduced, while long term drifts are almost completely removed.*

3.4. Power Stabilization

To avoid systematic effects occuring due to variations of the laser powers circulating inside the resonators we have to actively stabilize these powers. Therefore the powers transmitted through the resonators are detected with different photodetectors (PD1, PD2 and PD4; see figure 3.8).
The overall power of the beams impinging on the resonators can be controlled via the RF-power driving the respective AOM's. As already mentioned earlier, AOM 1 and AOM 2 are driven by a frequency synthesizer, which incorporates modulation inputs for frequency and amplitude of the produced radio frequency signal. We utilize the amplitude modulation inputs to stabilize the transmitted powers of beam 1 and beam 2 via a servo system with

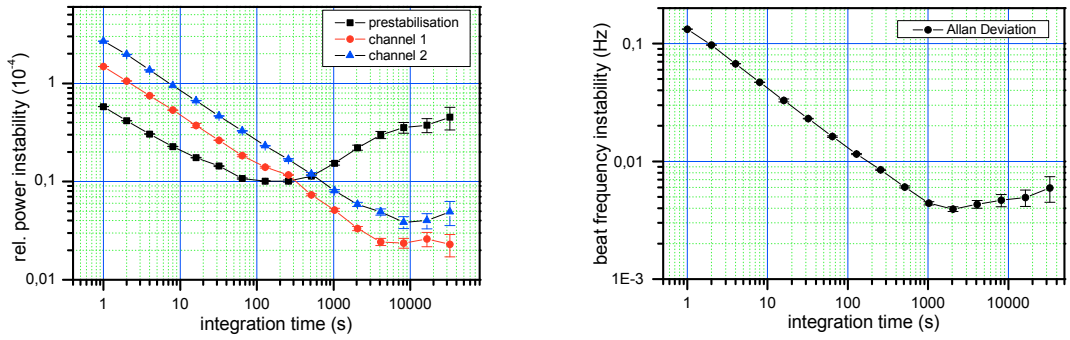

Figure 3.17.: *Residual instabilities of the transmitted laser powers upon rotation (left) and inferred instability of the beat frequency due to the power fluctuations (right).*

a bandwidth of approximately 2 kHz.
Via a variable offset voltage the servo system allows to set the desired DC power level.
AOM 3 is driven by a fixed frequency AOM driver. Within this driver, the RF-signal is produced by a local oscillator and is amplified by a broadband amplifier. To be able to control the RF power, a voltage variable attenuator (Minicircuits) has been added between the two stages and allows the stabilization of the power of beam 3.

Figure 3.16 shows the effect of the active stabilization on the laser powers transmitted through the resonators. Fluctuations of the laser power are strongly suppressed. Figure 3.17 shows on the left side the relative Allan deviation of the transmitted powers characterizing the residual instabilities. For the two channels of the finelocks the residual fluctuations show the behaviour of white noise, averaging out for longer integration times, till at ≈ 10000 s other noise types become dominant and lead to a slight increase in the instability.
The channel of the prestabilization lock is not so stable for longer times. However, this is no limiting factor for our measurements.

3.5. Rotation Table

As already mentioned earlier, it is in principle possible to utilize the natural rotation of the earth to determine the value of $(\beta - \delta - 1/2)$ in the Mansouri-Sexl frame and most of the coefficients in the standard model extension (SME). Restricting oneself to these values, one can use a stationary setup in the laboratory frame.
However, if one aims at determining also the coefficient $\tilde{\kappa}_{e-}^{ZZ}$ of the SME, one has to actively rotate the setup in the laboratory. Furthermore, for measurements with a stationary setup

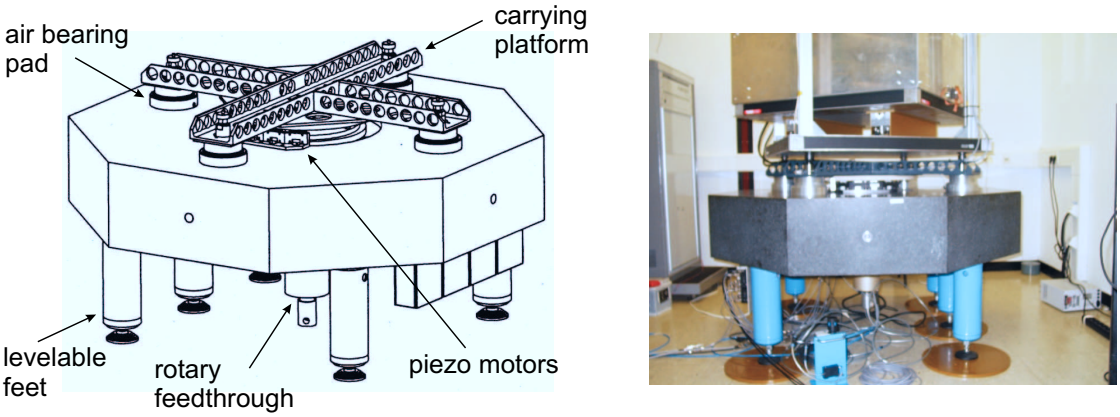

Figure 3.18.: *Left: Schematic drawing of the high precision air bearing rotation table with the main components. Right: Picture of the rotation table during the construction of the setup.*

parameter	value	parameter	value
baseplate diameter	152 cm	radial runout	$< 1\mu$m
rotor diameter	99 cm	axis wobble	< 2 μrad
weight	≈1300 kg	contouring error	< 0.7 μrad
maximum load	1200 kg	pressure axial bearing	typ. 1-2 bar
max. mass moment of inertia	192 kgm^2	pressure radial bearing	5-6 bar
max. tilting effect	300 Nm	max. velocity	5 rpm
planarity of baseplate	1 μm	angular resolution	0.01" ≅ 34 nrad

Table 3.1.: *Specifications of the high precision air bearing rotation table*

one needs a very good stability of the system on the timescale of half a day to a day, which is not so easy to realize, whilst for an actively rotating setup it is sufficient to have a very good stability on the timescale of the active rotation.
In the course of our measurements and the development of the setup, two different rotation tables have been used to actively rotate the setup. For first measurements a mechanical ball bearing rotation table was taken from the preceding experiment with cryogenic resonators [20], first results obtained with this table were reported in [68]. This was replaced at a later stage by a high precision rotation table with axial and radial air bearings. Some specifications are given in table 3.1, a drawing of the rotation table is shown in figure 3.18.

The rotation table consists of a baseplate of octagonal shape fabricated from granite and has a mass of ≈1300 kg. It has a surface flatness of ≤ 1 μm over the entire surface. Integrated within the baseplate is a rotary feedthrough system for electrical connections (power and signal lines) and for compressed air. The resistance noise of the electrical feedthrough

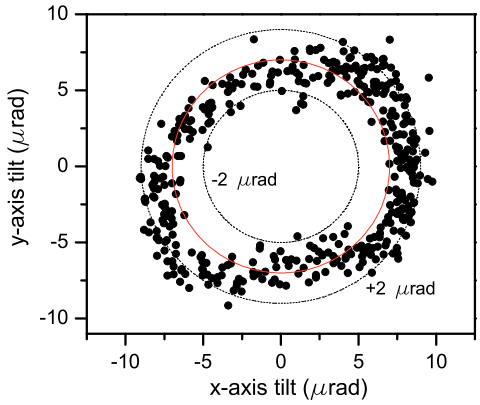

Figure 3.19.: *XY-plot of the two tilts of breadboard I upon rotation of the system. In absence of wobble of the axis the points should lie on a circle, as indicated by the red line. The dashed circles bound the tilts allowed by the specifications.*

is specified to be below 0.001 Ω. Furthermore, an angle encoder system is included to determine the angular position of the table. The angle encoder (with 90000 lines etched on a glass plate) works according to an interferential scheme and produces 180 000 signal periods per round. The output of the angle encoder is a $1V_{pp}$ signal varying sinusoidally upon rotation. Readout of the angle encoder is accomplished by a commercial servo system, which drives as well the motors for rotation of the table. The servo system interpolates the reading of the angle encoder output 1024 times, yielding $1024 \cdot 180000 = 1.8432 \cdot 10^8$ increments per round, resulting in an angular resolution of $\approx 34 \cdot 10^{-9}$ rad. Additionally an inductive sensor has been fixed to the ground plate, detecting the transit of a metal screw fixed to the rotor. The sensor switches from logical low to logical high during the transit and can be used to define the zero position of the table and to count the number of performed rotations. The zero position of the rotation table ($\theta = 0$) is such, that the orientation of one resonator is in north-south direction, while the other resonator is oriented in east-west direction with an error of few degrees.

On the same axis inside the baseplate sits a radial air bearing (typ. pressure 5.5 bar) with the rotor being connected to a cross-shaped platform carrying the experimental setup. At the outer end of the cross sit 4 air bearing pads (typ. pressure 1-2 bar) carrying the weight of the experiment. On the lower side of the carrying plate a ceramic driving ring with an outer diameter of ≈ 0.5 m and an inner diameter of ≈ 0.36 m has been fixed, while on the baseplate of the table 8 piezomotors have been fixed. These contact the ceramic driving plate and rotate the table by moving the ceramic strip.

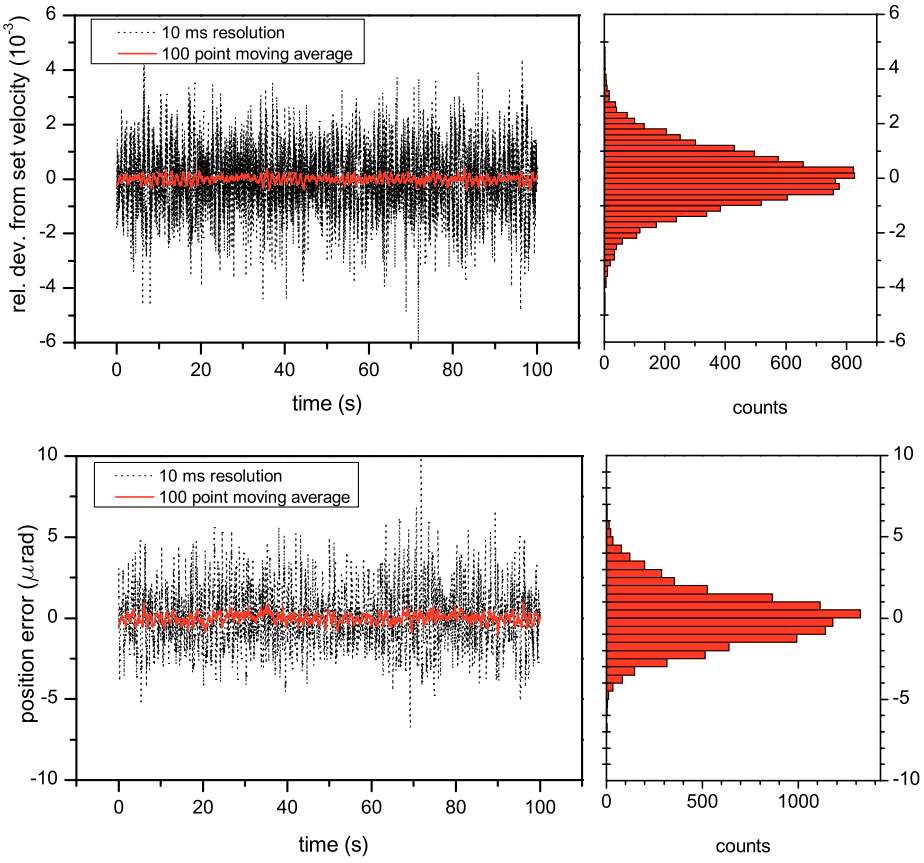

Figure 3.20.: *Fluctuations of the angular velocity (top) of the rotation table and the position error (bottom), measured with the servo system that controls the rotation.*

Characterization

With the components just described the table is specified to have a radial runout below $1\ \mu$m and a wobble of the rotation axis below $2\ \mu$rad. The wobble of the rotation axis was measured upon delivery of the table and is with few μrad within a small factor of the specified value. Figure 3.19 shows for one measurement the modulation of the tilts with rotation in an xy-plot. Without wobble of the axis the points should lie on a circle as indicated by the solid red circle. The dashed circles limit the region in which the tilt should

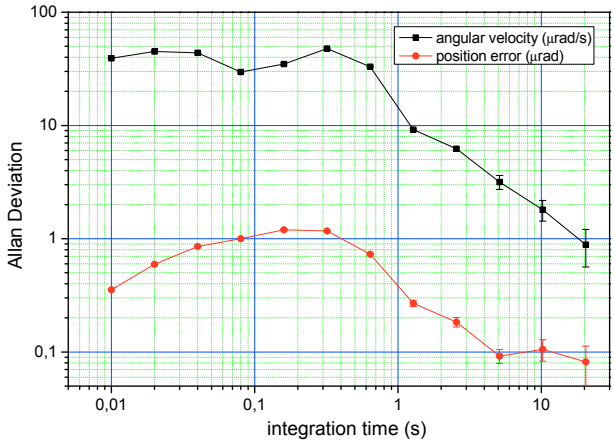

Figure 3.21.: *Absolute Allan Deviation of the angular velocity of the table (in μrad/s) and of the position error (in μrad).*

vary according to the specifications ($\pm 2\mu$rad). The measurement noise of the tilt sensors leads to a scatter of the datapoints of $\approx \pm 1$ μrad. As can be seen the specification is approximately satisfied. The radial runout has not been checked.
Figure 3.20 shows the typical fluctuations of the angular velocity of the rotation table on the timescale of several milliseconds, as it has been measured via the servo system that controls the rotation. The angular velocity was ≈ 70 mrad/s. From this data the overlapping Allan deviation as given in appendix A has been calculated (see fig. 3.21), characterizing the instability of the angular velocity. For integration times above 1 s, which corresponds to the gating time of our frequency measurements, the absolute instability is below 10 μrad/s. Thus, the relative instability of the angular velocity is below $2 \cdot 10^{-4}$.

3.6. Tilt Stabilization

One of the most severe systematic effects associated with Michelson-Morley experiments comes from variations of the tilt of the optical resonators with respect to the direction of gravitation. This is due to elastic deformations of the resonator block under the varying gravitational forces acting on the block.
For actively rotated experiments the axis of rotation therefore has to be aligned in such a way that it coincides exactly with the direction of gravity. Of course the rotation table as well as the laboratory environment are not perfect, so that one has to stabilize, or at least to record, the tilt of the resonators continuously.

Series 755 tilt sensor	
total range	$\pm 1^\circ \cong 17.5$ mrad
resolution	0.1 μrad
repeatability	1 μrad
linearity	0.1' within $\pm$10'
	0.5' within $\pm$20'
scale factor @ 20°C	7.2 mV/1'/1 V_{exc}
natural frequency	0.77 Hz
damping	45%
signal conditioning unit 781	
output voltage range	$\pm$8 VDC (single-ended)
	$\pm$16 VDC (differential)
gain range	$\times$1, $\times$10
temperature output	0.1°C/mV (single-ended), -40°C to +100°C
integrated lowpass filters	$\tau_{on} = 7.5s$, $f_{-3dB} = 1/(2\pi\tau) = 0.02$ Hz
	$\tau_{off} = 0.05s$, $f_{-3dB} = 1/(2\pi\tau) = 3.2$ Hz
filter roll-off	-6 dB/octave
scale factors	high gain: ≈ 0.1 μrad/mV (single-ended)
(with given sensor)	low gain: ≈ 1 μrad/mV (single-ended)

Table 3.2.: *Specifications of the electronic bubble level tilt sensors and the signal conditioning unit by Applied Geomechanics Inc.*

To do so we use a two-axes electronic bubble level tiltmeter[5] and two single-axis tiltmeters of the same type with a measurement resolution of approximately 1 μrad. Table 3.2 shows some of the specifications of the tilt sensors and the signal conditioning unit. Operating in the high gain mode, they deliver a voltage of 20 mV/μrad for a differential output configuration. The natural time constant of the tilt sensor is $\tau = 0.5\ s$. These signals are used to realize a servo system via a LabVIEW-program.

3.6.1. Building Movements and Baseplate Stabilization

One main contribution to a varying tilt of the whole setup comes from the variation of the ground floor tilt. Unfortunately our laboratory is situated on the second floor, where varying temperatures of the building have already a considerable effect on the tilt of the building. Figure 3.22 shows the variation of the tilt of the rotation table baseplate due to the night-day cycle of the building's tilt. To compensate for this effect we implemented an active stabilization of the tilt of the rotation table baseplate.
The baseplate is resting on 3 feet[6], 2 of which include air spring elements usually used as

[5] 755-series with signal conditioning unit model 781 by Applied Geomechanics
[6] Two further feet are additionally put for security purposes to avoid overturning of the baseplate

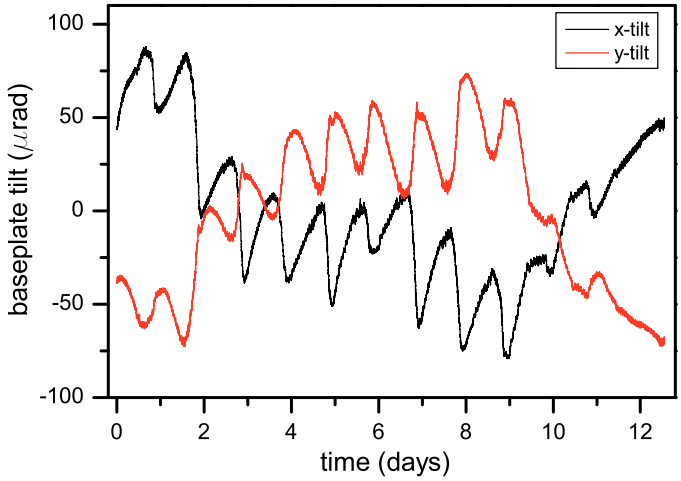

Figure 3.22.: *Drift of the tilt of the rotation table's baseplate over the course of several days.*

bearings for industrial machinery to damp oscillations and vibrations (see right side of figure 3.23). Each of these air springs is able to carry a maximum load of 1.3 t. The pressure will vary between 1 and 6 bar for loads between 200-1300 kg. The air springs act like a passive isolation system with a resonance frequency which depends on the given load and is in our case $\approx 4-5$ Hz. Oscillations occuring at this frequency are already damped by the active vibration isolation. A damping element integrated in the air spring limits the resonance gain of the air springs to ≈ 3.5. Regulating the amount of air inside the elements allows for changing their height by $\approx \pm 6$ mm according to the specifications. This corresponds to a tilt variation of several mrad.

To measure the tilt of the baseplate we use the two single-axis tilt sensors. This allows to measure the tilts of the baseplate with respect to two pivots which are not orthogonal to each other, as is the case for a 3-feet system with two adjustable feets. Thus a change of tilt on one axis should not influence the reading on the other axis. However, this independence is only given if the pivots are fixed. In our case the changing load distribution leads to some influence on the tilt of the second axis as well due to the finite stiffness of the air springs. To be able to control the height of the air springs we use a system of 2-way and 3-way solenoid valves. Figure 3.23 shows a sketch of the stabilization system for one channel. The pressurized air supplied by the university ($p > 6$ bar) is connected via a tee (not shown) to the inlet of a 3-way valve which can be controlled with TTL-signals via a small controller

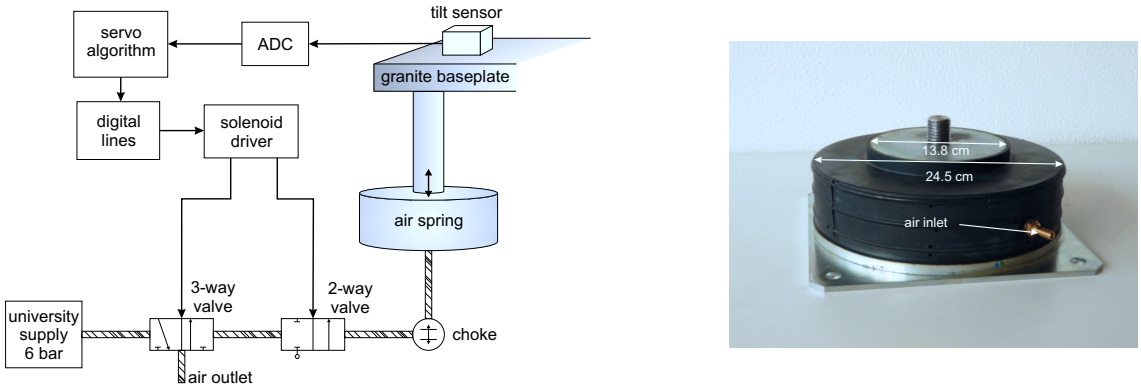

Figure 3.23.: *Left: Scheme of the stabilization system for the tilt of the rotation table baseplate, right: a picture of the air spring used for the stabilization.*

box. Logical high lets the air from the university supply float through the valve, while logical low will let the air of the air spring stream out into the laboratory. Since one wants to be able to hold a certain position as well, a 2-way valve has been placed between the 3-way valve and the airspring. Closing the valve by applying a logical low signal holds the position and no air is flowing at all. Opening the valve regulates the height of the actuator according to the setting of the 3-way valve.
To regulate the flux of air a choke has been placed at the inlet of the air spring. This can be adjusted manually to realize different time constants for the servo system. The specified range of the choke is 0-600 l/min at a pressure difference of 6 bar.

An undesirable effect uncovered after the implementation of this system is a modulation of the tilt reading of the two single-axis tilt sensors when the setup on top of the baseplate is rotated. Initially, this effect was as large as 100 μrad peak to peak. By changing the load distribution on the setup the effect could be reduced by a factor of 5 approximately. Still, the sensors on the optics breadboard show a residual modulation upon rotation of about 5 μrad_{pp} in best case (well aligned rotation axis). This residual modulation can be compensated by an additional regulation system.

The modulation of the baseplate tilt upon rotation measured by the sensors (≈ 20 μrad_{pp}) precludes the use of a simple PI-servo control. Therefore we used a different digital algorithm. The tilt sensor values are acquired at a rate of 1 Hz with a USB-DAQ-board (NI-6009) and the lowpass filter of the signal conditioning unit is switched on. The average over the last n readings is calculated, where n is the number of readings during one period of rotation. Thus the effect of the modulation averages out. Now if the deviation of the average from a set value is too large, the solenoid valves are switched accordingly until the average lies close enough to the set point. The minimum deviation which can be used as switching point is predefined by the rotation period (time used for averaging)

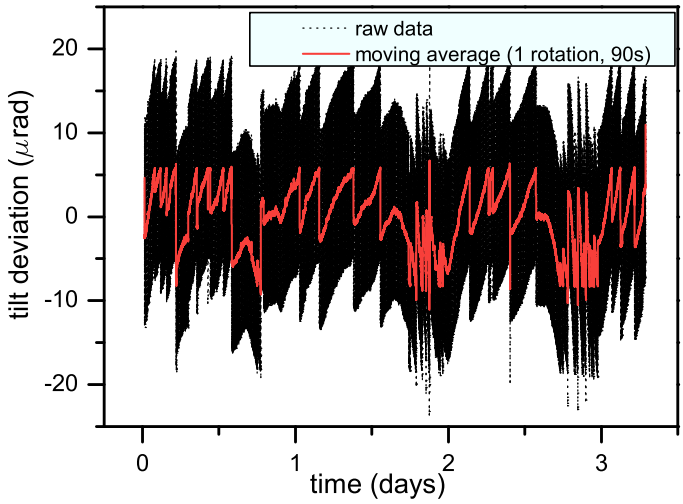

Figure 3.24.: *Residual modulations of the baseplate tilt after the implementation of active control (rotating system).*

and the setting of the choke controlling the air flux to/out of the air springs. Setting the switching point too close to the setpoint will result in oscillations of the system. A good setting for a rotation period of 90 s and the given setting of the choke is a deviation of ± 7 μrad from the setpoint. The setpoint is determined such that the modulation of the tilt of the experimental setup is minimized. Figure 3.24 shows the temporal behaviour of the baseplate tilt during one of our measurement runs with a rotation period of 90 s. The mean baseplate tilts are kept within a range of $\approx \pm 7$ μrad from the setpoint.

3.6.2. Stabilization of the Breadboard Tilt

The stabilization of the baseplate already strongly diminishes the slowly varying tilts of the setup in the nonrotating case. However, it does not keep the axis of rotation perfectly in the direction of local gravity. Deviations from this occur due to the imperfect stabilization of the baseplate and due to wobble of the rotation axis. This effect is on the order of several μrad and would produce a systematic effect on the beat frequency measurement upon rotation. Thus the tilt of the breadboard carrying the experiment has to be stabilized further.

For this purpose we use two voice coil actuators fixed at the sides of the optics breadboard (see fig. 3.1) and take advantage of the fact, that the optics breadboard is not

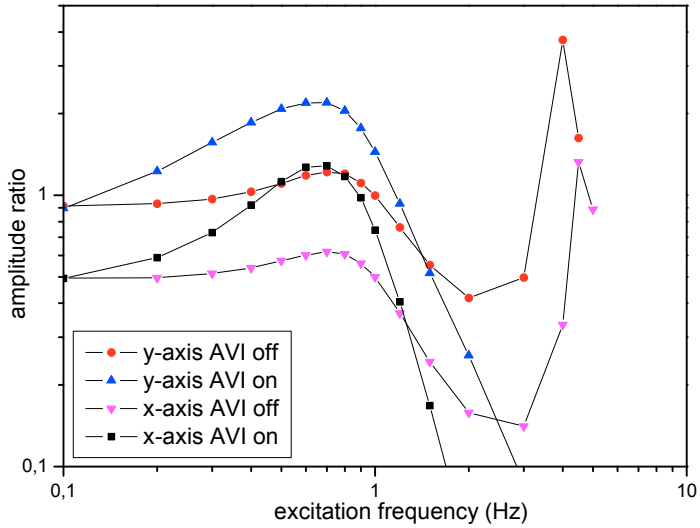

Figure 3.25.: *magnitude of the transfer function of the tilt stabilization system*

rigidly connected to the rotor of the rotation table, but is standing on two active vibration isolation supports (AVI), which are flexible and can be slightly tilted without greatly diminishing the vibration isolation. The voice coil actuators consist of a permanent magnet core with strong neodym magnets and copper coils.
The tilt of the breadboard is monitored with the two-axis tiltmeter fixed below the breadboard in a central position, so as to minimize effects of the centrifugal acceleration on the reading of the tilt sensors. To avoid damage of the voice coil actuators due to overheating the current through the coils is limited to below 5 A defining the maximum compensation range of the stabilization. The coils are driven by a power amplifier, which can be controlled via analog signals from the output of a DAQ-board. Analog signals between -5 and +5 V lead to a current through the coils of approximately ± 5 A and tilt the breadboard by $\approx \pm 170$ μrad in the x-axis and by $\approx \pm 280$ μrad in the y-axis. The difference is primarily due to the different stiffness of the AVI-system in the two directions.
Using the described components an active digital feedback system has been realized with the algorithm programmed in LabVIEW. For first measurements a simple PI-algorithm has been used, but the maximum possible gain and minimum possible update rate were limited by resonances of the combined system AVI - tilt sensors - voice coil actuators. To gain further information about the combined system the transfer function of the system has been determined by applying a modulation with varying frequency to the input of the power amplifier driving the actuators and monitoring the output of the tilt sensor. This has been

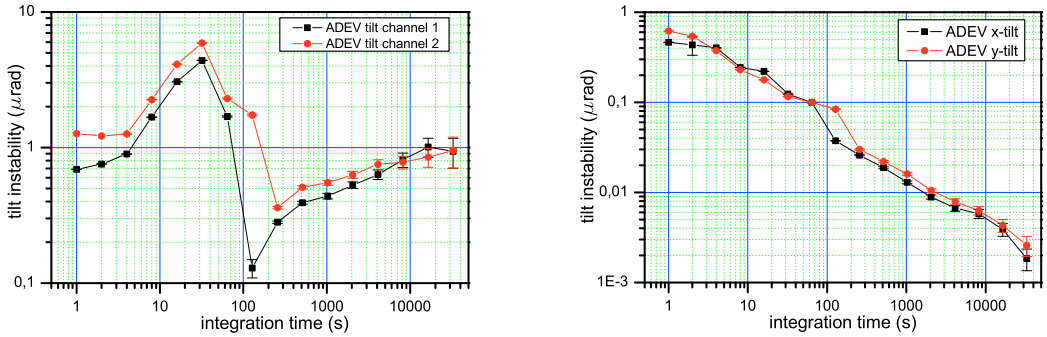

Figure 3.26.: *Residual instabilities of the tilt of the experimental setup under active control. Left: baseplate tilt. Right: residual breadboard tilts during rotation with a period of 90 s.*

done for the case of active vibration isolation and for the case of passive vibration isolation (AVI switched off). The result of the measurement is shown in figure 3.25. For both cases one finds resonances of the combined system with the (main) resonance frequency being shifted from $\approx 4-5$ Hz (AVI off) to ≈ 700 mHz (AVI on). The resonance at 4-5 Hz corresponds to the resonance of the springs inside the AVI, which are carrying the weight of the setup, while the resonance appearing at ≈700 mHz is given by the tilt sensor and the AVI (in active mode) together. The maximum gain and the update rate of the servo system are limited by this resonance.
However the update rate can be shifted to values beyond the resonance using a so called lead-lag-algorithm (see e.g. [69] or other books on feedback systems). The optimal parameters for this algorithm have been estimated using the *Control Design and Simulation* package of LabVIEW.

Figure 3.26 shows the residual instabilities of the tilt of the breadboard and the baseplate under active control calculated from a dataset with a length of approximately 1 day. At short integration times (few seconds) the instability is given by the measurement noise of the tilt sensors.
The baseplate tilt shows an increased instability at roughly half the period of rotation, corresponding to the modulations of the tilt reading mentioned in 3.6.1. This modulation averages out for integration times on the timescale of the rotation leading to the dip at 100-200 s. For larger integration times the slowly varying tilt of the building leads to an increase in the instability of the baseplate tilt.
The tilt of the breadboard carrying the optical setup averages down over the complete range of integration times and shows no distinct features. On the timescale of half a rotation

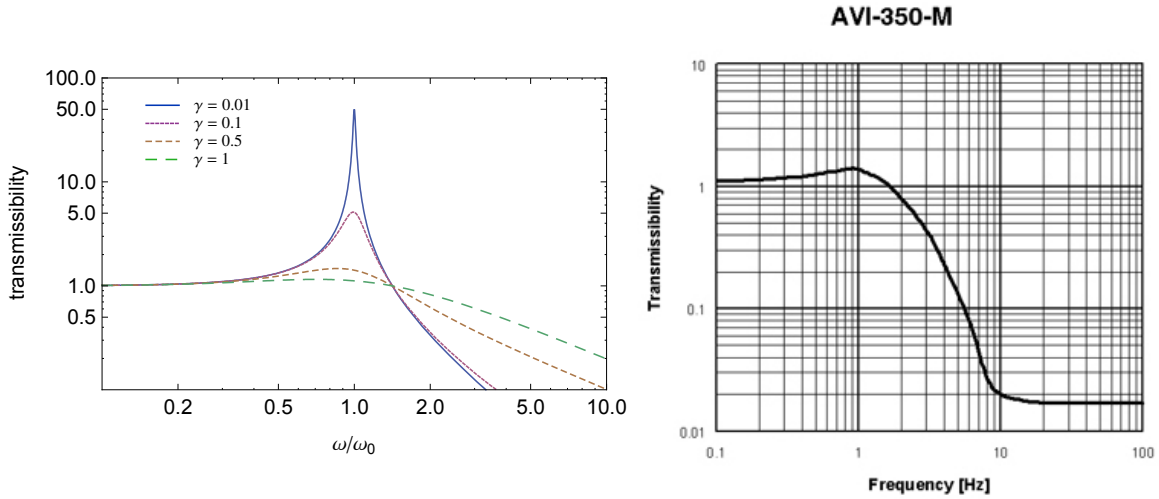

Figure 3.27.: *Left: The transfer function for a one stage passive isolation system for different values of the damping constant γ. Right: Transmission of vibrations through the AVI-system as function of the frequency.*

the instability is on the order of $0.1 - 0.2$ μrad. As will be shown in section 4.1 this is not purely statistical noise, but contains almost constant modulations of the tilt upon rotation (see fig. 4.4), which could not be further suppressed on this timescale by the stabilization system.

3.7. Active Vibration Isolation

Vibrational noise at low frequencies is one of the main contributions leading to an increase in the linewidth of a laser system and in the resonance width of a resonator. Therefore special caution has to be taken to properly isolate the setup against vibrational noise. The noise can have two different origins:

1. technical noise due to moving parts of the setup, e.g. fans in the control electronics etc. (high frequency range)

2. seismic noise and movements of the building and the laboratory ground (low frequency range)[7].

The latter are primarily limiting the short time stability [71]. In experiments aiming at the realization of ultra-narrow linewidth lasers one may therefore use long pendulas or spring

[7] See e.g. [70] for further discussion

Figure 3.28.: *Left: Schematic of an active vibration isolation support and its main components. Right: commercial AVI system*

systems with low resonance frequencies ω_0 and some damping γ for this purpose, serving as a passive isolation unit with a transfer function [72]

$$T(\omega) = \sqrt{\frac{1 + (2\gamma\frac{\omega}{\omega_0})^2}{(1 - \frac{\omega^2}{\omega_0^2})^2 + (2\gamma\frac{\omega}{\omega_0})^2}}. \tag{3.14}$$

Figure 3.27 shows the transfer function for different values of the damping. Below the resonance frequency a passive system is not isolating at all, directly on resonance one has a resonance enhancement depending on the damping γ and only for frequencies above $\sqrt{2}\cdot\omega_0$ the system starts to isolate. One main problem of passive systems is the fact, that it is very hard to bring ω_0 to low values, since the resonance frequency depends on the dimensions of the pendulum/spring[8].

Active vibration isolation systems (AVI's) have many advantages compared to the passive system described above. The dimensions of an active system can be very compact compared to a passive isolation, which is desirable especially in our case since the whole system has to be rotated. Furthermore an active system can as well partly suppress vibrations which are produced by the experiment itself.
A simplified scheme of such a system is shown in Figure 3.28. A sensor element (piezoelectric crystal) registers the acceleration of an inertial test mass relative to the surface which should be isolated against vibrations. This surface is supported by a system of springs, which already realize a passive isolation system. The registered accelerations are processed by an electronical feedback system, which drives several actuators (piezo-electric). These initiate a movement of the upper plate relative to the ground plate corresponding to an acceleration which is phase-shifted by 180° with respect to the original disturbance, thus they compensate the overall acceleration of the upper plate.
The lowest resonance frequency appearing in the system in closed loop operation depends on the gain of the feedback loop [70], setting a limit to the possible isolation band of the

[8] To obtain $\omega_0 = 1$ rad/s one would need a pendulum of 10 m length.

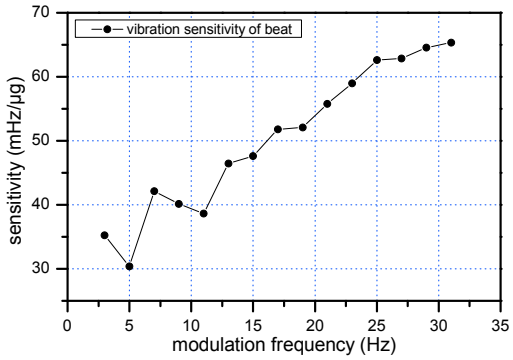

Figure 3.29.: *Sensitivity of the beat frequency measurement to accelerations in the vertical direction.*

system. Another limiting factor are passive resonances of the system and couplings between the different degrees of freedom (vertical/horizontal/rotational).
For this work the commercial system AVI-350M by HWL/TableStable (see right side of figure 3.28) has been used. This system suppresses vibrations in the frequency range of 2-100 Hz actively by more than 35 dB, above it works like a passive isolation system. The mass which can be put on top of the two supports is limited to ≈ 350 kg. With the two elements all six degrees of freedom (translation and rotation) can be isolated against vibrations. Another advantage of the system is the possibility to deliberately introduce accelerations via the included modulation input. Doing so one may determine the sensitivity of the system to accelerations. Applying signals in the range 2-100 Hz will result in a movement of the corresponding axis. The velocity amplitude is approximately constant over the frequency range, ≈ 15 μm/s for a signal of 1 V_{pp} at the input, the acceleration amplitude will behave like $a \approx \frac{15\mu\mathrm{m\cdot s^{-1}}}{\omega_{mod}}$. However for frequencies above 30 Hz no pure excitation will occur, but a mixed excitation of all the axes will result.
Figure 3.29 shows the results of such a measurement for vertical accelerations. The sensitivity of the beat frequency measurement is approximately 55 mHz/μg, corresponding to a fractional sensitivity (relative to the laser frequency ν_0) of $2 \cdot 10^{-11}$ $\mathrm{s^2m^{-1}}$. This value is only about a factor of 4 larger than the value reported by Nazarova et al. [73] for a single resonator with a special vibration insensitive mount.
Figure 3.30 shows the influence of the low frequency vibrations on the frequency noise of the beat frequency. Shown on the left is the spectrum of vibrations in the vertical direction as measured with an accelerometer from PCB Piezotronics Inc. (model 393A03) with a sensitivity of 1000 mV/g in a frequency range of 0.2-6000 Hz (-3dB). The use of the AVI system suppresses the vibrations to a level which is not detectable anymore with the given accelerometer and FFT analyzer. On the right is shown the effect of the vibrations on the

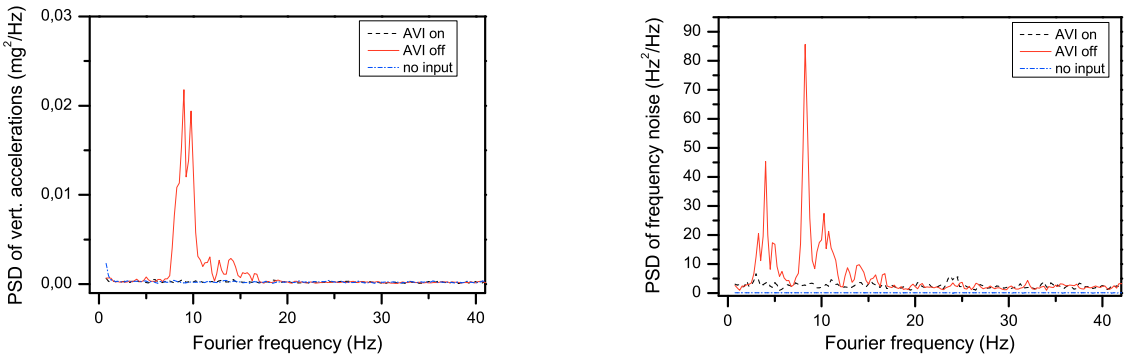

Figure 3.30.: *Left side: Fourier spectrum of the vertical accelerations present on the breadboard carrying the optics with and without the use of the AVI system. Right side: Suppression of frequency noise due to vibrations via the AVI.*

frequency noise of the beat frequency. To measure this, a frequency to voltage converter (FVC) with a discriminator slope of 10 V/100 kHz has been used to produce an electrical signal proportional to the instantaneous beat frequency. Additional peaks arise compared to the spectrum of the vertical accelerations, since the beat frequency is as well disturbed by accelerations in the horizontal directions. Clearly the use of the AVI strongly reduces the frequency noise by suppressing vibrations.
The effect becomes even more evident if one measures the linewidth of the beat between the two resonator frequencies. Figure 3.31 shows the positive influence of the AVI on the linewidth of the beat. With the AVI the line has a width of few Hertz, while without AVI the width of the line as determined via a Lorentz fit is increased to more than 30 Hz.

3.8. Temperature Stabilization

As already mentioned it is important to obtain a high dimensional stability of the resonator length, which makes a stable resonator temperature a necessity. Problematic for this purpose is the location of our laboratory. Although the laboratory has no windows, the temperature rises considerably on sunny days since starting from noon the sun is directly heating the outer (thin) wall of the laboratory. Therefore several means had to be incorporated into the setup to achieve a sufficient stability.
First of all it is important to achieve a high passive stability of the resonator temperature, requiring the damping of fluctuations of the ambient temperature. As a first isolation stage serves the vacuum chamber, where the mechanical contact between the resonator mounting and the vacuum chamber itself was minimized to obtain a large time constant for temper-

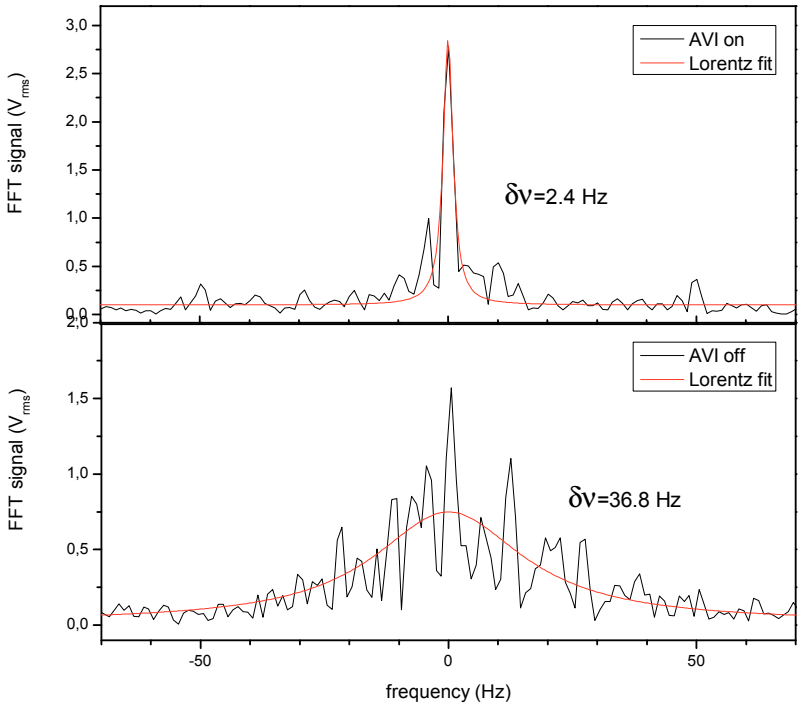

Figure 3.31.: *Linewidth (Full width at half maximum) of the beat frequency as measured with a FFT analyzer. The width increases considerably if the active vibration isolation is switched off.*

ature changes of the resonator due to external temperature changes. As already described, the vacuum chamber itself stands inside a wooden box. This box is foam padded from both sides to minimize the heat exchange with the surrounding.
The temperature of the laboratory can be controlled via two chillers distributed in the laboratory. One chiller is cooled by the cooling water supply of the university. However, during hot summer days this cooler is not sufficient to keep a stable temperature within the laboratory, since the cooling power is too low.Thus we added an electrical chiller with a cooling power of 2.6 kW.
The two chillers are operated in different modes. For the water cooled chiller we decided to switch off the control unit and to operate it with the full cooling power at all times. This mode was chosen since the air of this cooler is directly flowing on top of our tower around the experiment, thus cooling the upper part of our TEC elements, which are removing heat from the tower. Doing so we ensure good heat removal from the tower and avoid effects due to switching processes of the cooler observed in the beginning of our measurements.

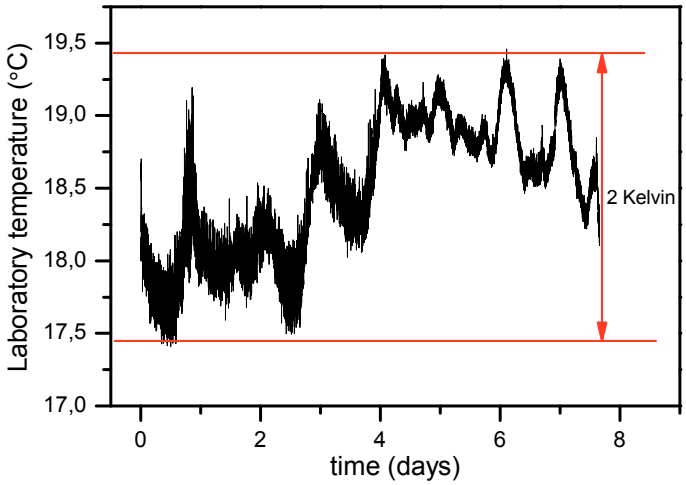

Figure 3.32.: *Variation of the laboratory temperature during an 8 day long measurement run on easter 2009*

For regulation of the temperature in the laboratory thus primarily the electrical chiller is used, which is set to the desired room temperature. To enable an active control of the temperature inside the tower, the top has been equipped with elements containing thermoelectric coolers. At the beginning of our measurements this system worked well. However, in the course of our measurements additional electronics has been placed inside the tower and the cooling power of the elements was not sufficient anymore to keep the temperature very stable.

Figure 3.32 shows the temperature in the laboratory during a measurement session of few days over easter 2009. Using the two chillers it is possible to keep the temperature of the laboratory within a range of $\pm 1°C$.
Figure 3.33 shows as an overview the variation of the temperature at several positions within the experimental setup, as well as the measured beat frequency (top left). Shown at the top right is the temperature inside and close to the top of the tower. It is measured with a sensor rotating with the experimental setup. Compared to the laboratory temperature the inside variations are reduced only by a factor of 2 to about ± 0.5 °C due to the fact, that the tower had to be kept slightly opened at the top to enable better heat removal.
The second row of figure 3.33 shows the temperature at a height of 1 m as measured with two stationary sensors on opposite sides of the tower. The fluctuations on the timescale of the rotation result from the electronics equipment, which rotates together with the optical

setup. This equipment emits heat, usually via fans within the housing, thus producing a non-isotropic flux of warm air, which leads to a periodic modulation of the measured temperature for the static temperature sensors.
However, the optical setup is shielded versus the temperature influence of the outside via a foam padded shielding. The temperature close to the optics is sensed with two sensors on different sides of breadboard I (see fig. 3.1). These should detect a possible effect of a gradient of the tower temperature on the optics temperature, since upon rotation a sinusoidal modulation of the temperature may be expected. This is not detected.
Additionally, the temperature within the wooden box surrounding the vacuum chamber with the resonators is sensed with two sensors. The corresponding temperature variations are shown in the bottom row of figure 3.33.

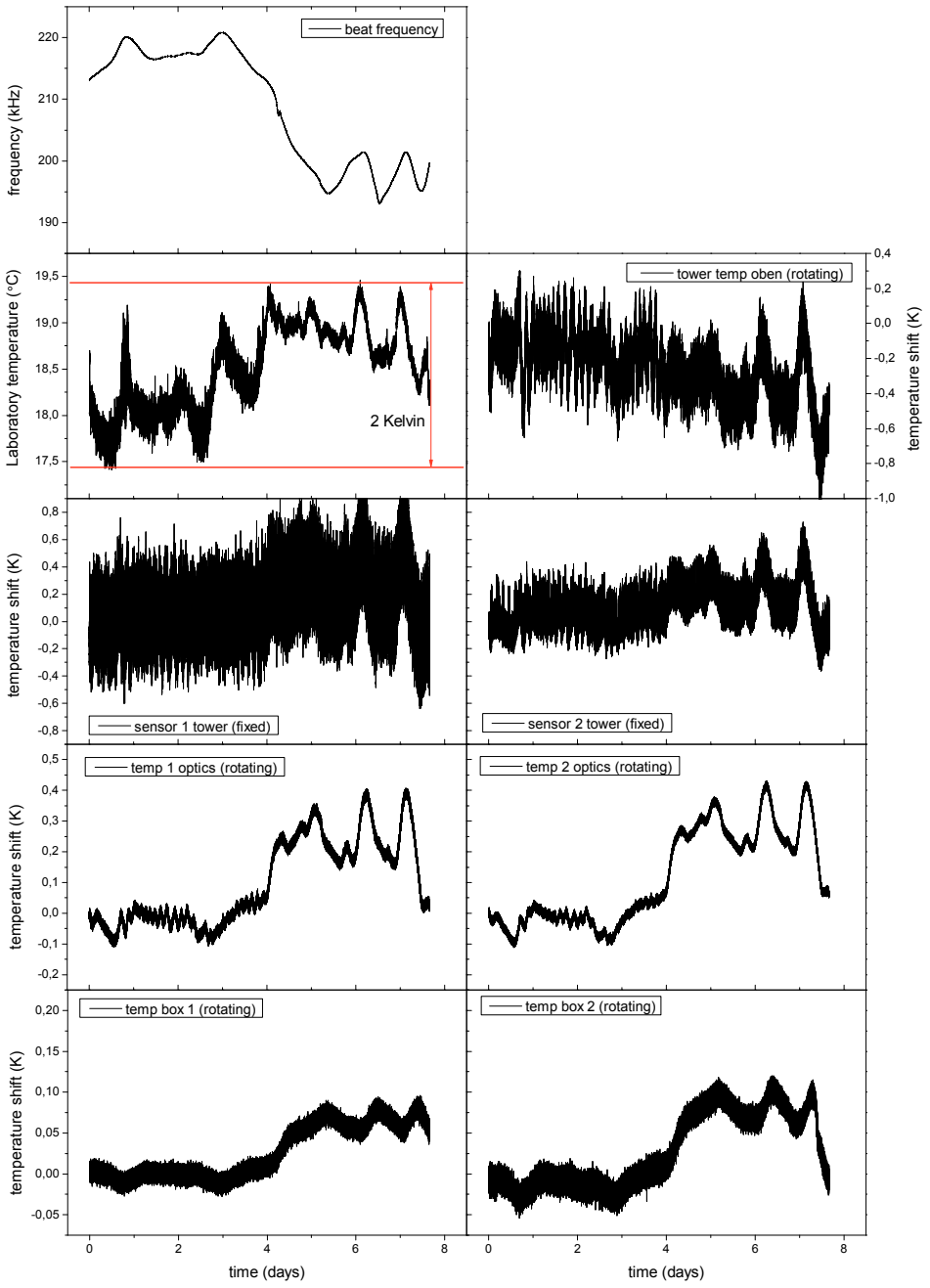

Figure 3.33.: *Overview of the temperature variations at different positions over the course of an eight day long measurement on easter 2009. Top left: beat frequency.*

4. Sources of Systematic Effects

Several different influences can disturb the resonance frequency of the resonators and may lead to systematic effects on the beat frequency $\nu_b = \nu_1 - \nu_2$. Some of these effects have already been mentioned partly in chapter 3. Here a detailed overview of the different sources and magnitudes of possible systematic errors will be given. Among the different sources are:

- variations of the resonator tilt relative to the direction of the gravitational force,
- variations in the speed of rotation leading to varying centrifugal forces,
- variations of the power of the laser light circulating inside the resonators,
- frequency drifts induced by temperature variations of the resonators and the optical setup.

Throughout all of our measurements the dominant systematic effect remaining on the beat frequency measurement was observed at the frequency of the table rotation ω_{rot} (magnitude ≈ 0.5 Hz), while the effects at $2\omega_{rot}$ were extremely small. These would compromise primarily the determined value for $(\tilde{\kappa}_{e-})^{ZZ}$, which is only influenced by constant modulations at $2\omega_{rot}$ and has no sidereal or annual component. All other coefficients are not influenced by a constant offset in the determined amplitudes, since they are determined by the sidereal and annual modulations of the amplitudes $B(t)$ and $C(t)$.

4.1. Tilt of the Rotation Axis

As has already been mentioned, it is important to keep the tilt of the optical setup relative to the direction of local gravitation as stable as possible to avoid systematic effects associated with varying gravitational forces acting on the system. A variation of these forces will result in two main effects:

- The structure of the resonator will deform according to the changing forces on the structure. This will lead to a varying spacing between the mirrors forming the resonator, thus shifting the resonance frequency. Furthermore the mirrors will be slightly tilted versus each other leading to an additional shift of the resonance frequency.
- Optical elements used for coupling the beam into the resonator will bend slightly and thus a small misalignment of the beam will result. This leads as well to a small shift

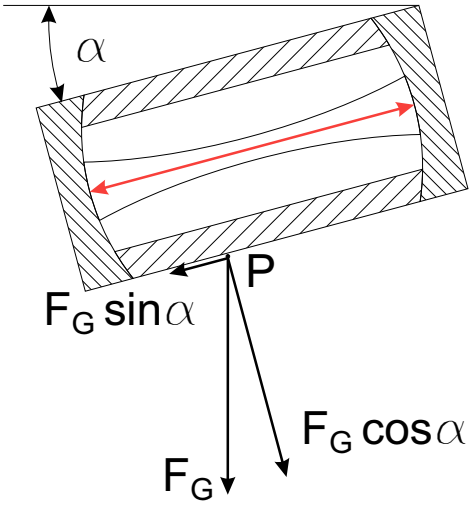

Figure 4.1.: *Forces acting on a resonator, which is tilted by an angle α with respect to gravity.*

of the resonance frequency. The size of this effect can hardly be estimated, but the magnitude of the combined effect can be measured, yielding a sensitivity coefficient.

For the deformation of the resonator a rough estimate of the effect can be found using simple mechanics. The only force acting on the resonator block in steady state conditions is the gravitational force of its own mass. This can be split in two components, a component normal to the plane in which the resonators lie, and a component pointing along the axis of the resonator. Figure 4.1 illustrates this. For simplicity we consider one resonator and simplify the geometry to a solid rod. For the situation where no forces act on this solid rod we assume it to have the height h (30 mm) and the length L (84 mm).

The component of the gravitational force acting normal to the resonator's axis, $F_n = F_G \cdot \cos\alpha$, compresses the resonator block, thus reduces its height according to Hooke's law

$$\frac{\Delta h}{h} = \frac{F_G \cdot \cos\alpha}{E \cdot S}, \tag{4.1}$$

where α is the tilt angle, E is Young's modulus ($67.6 \cdot 10^9$ Nm^{-2} for ULE) and S is the surface on which the force F_n acts. Due to the finite Poisson ratio η of the material (0.17 for ULE[1]), the length L of the rod will be increased by an amount

$$\frac{\Delta L}{L} = \eta \cdot \frac{\Delta h}{h} = \eta \cdot \frac{\rho g h \cos\alpha}{E}, \tag{4.2}$$

where $F_G = \rho g h S$ has been substituted for the gravitational force of the resonator block with ρ being the density of the rod ($2.21 \cdot 10^3$ kg/m^3 for ULE). This effect is on the order

[1] as given in the datasheet of the manufacturer

of $5 \cdot 10^{-9}$ for our resonator block as compared to a situation without gravitation. Thus, the sensitivity to vertical accelerations is on the order of $5 \cdot 10^{-10}$ s^2/m for a single resonator.

The force $F_p = F_G \sin\alpha$ acting in the direction of the resonator axis leads to an effect, which depends as well on the position of the point P where the resonator is fixed to the mount. In the case that the resonator is fixed exactly at its center this force will lead to no change of the resonator's length, since the effects on the two sides just cancel. However, if the resonator is not fixed in its center (see figure 4.1), one side of the block will be compressed in the axial direction, while the other side extends by a different amount in the same direction, thus effectively resulting in a change of the length of the resonator. Assuming the point P to be at a distance d from the center of the resonator, the change of the resonator length can be written as the sum of the compressed (ΔL_1) and the extended side (ΔL_2)

$$\begin{aligned} \Delta L &= \Delta L_1 + \Delta L_2 \\ &= -(L/2+d) \cdot \frac{\rho g (L/2+d) S \sin\alpha}{ES} + (L/2-d) \cdot \frac{\rho g (L/2-d) S \sin\alpha}{ES} \\ &= \frac{\rho g \sin\alpha}{E} \cdot [(L/2-d)^2 - (L/2+d)^2]. \end{aligned} \tag{4.3}$$

Using the parameter $\gamma = \frac{d}{L/2}$, $\gamma \in [-1, 1]$, the formula can be simplified yielding for the relative variation of the total resonator length

$$\frac{\Delta L}{L} = -\frac{\rho g L \gamma \sin\alpha}{E}. \tag{4.4}$$

The combined effect of the force acting normal and parallel to the resonator axis is thus given by

$$\frac{\Delta L}{L} = \frac{\gamma \rho L g}{E} \cdot \sin\alpha + \frac{\eta \rho h g}{E} \cdot \cos\alpha. \tag{4.5}$$

Now we can derive an estimate for the sensitivity of the resonance frequency to small tilt variations. If we assume that the resonator has a small offset tilt α, and that we change the tilt by a small angle $\delta\alpha$ only, then we may expand eq. 4.5 yielding

$$\frac{\Delta L}{L} = \frac{\rho L g}{E} \cdot [-\gamma \delta\alpha - \frac{\eta h}{L} \cdot (\alpha \delta\alpha + \frac{\delta\alpha^2}{2})].$$

The relative change of the resonator length is equal to the relative shift of the resonance frequency. Rearranging the last equation to describe linear and quadratic effects in $\delta\alpha$ gives

$$\begin{aligned} \frac{\Delta\nu}{\nu_0} &= -\frac{\rho L g}{E} \cdot [\gamma - \frac{\eta h \alpha}{L}]\delta\alpha + \frac{\eta \rho g h}{2E}\delta\alpha^2 \\ &= -A \cdot \delta\alpha - B \cdot \delta\alpha^2, \end{aligned} \tag{4.6}$$

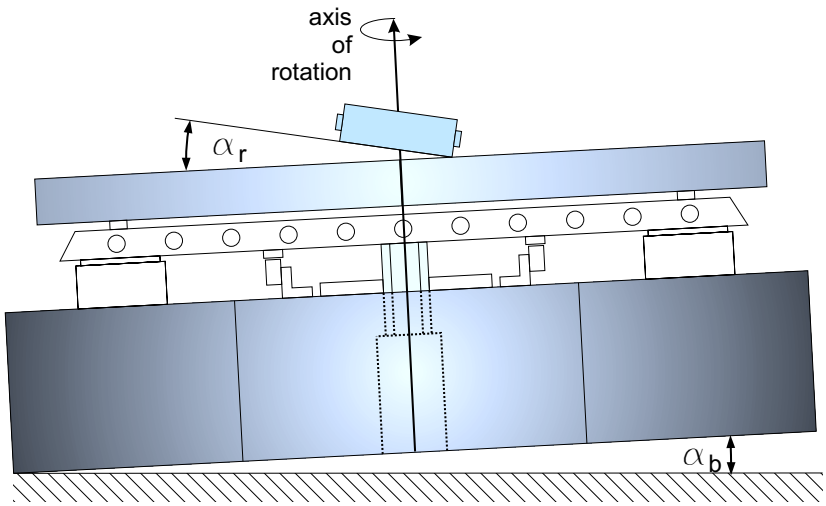

Figure 4.2.: *Influence of the tilt of the rotation axis on the orientation of the resonator with respect to gravity.*

thus $\nu_0 \cdot A$ and $\nu_0 \cdot B$ are the linear and quadratic sensitivities of the resonance frequency of a resonator with center frequency ν_0 to small tilt variations. As an example we consider a symmetry factor $\gamma = 0.02$ and a negligible offset tilt ($\alpha < 50$ mrad), obtaining

$$\begin{aligned} A\nu_0 &\approx 150 \text{ mHz}/\mu\text{rad} \\ B\nu_0 &\approx 0.2 \ \mu\text{Hz}/\mu\text{rad}^2. \end{aligned}$$

Thus, for small changes in the tilt α the quadratic term $B\nu_0$ is usually negligible and only linear frequency shifts are expected. Only for the case of almost perfectly symmetric fixing of the resonator the quadratic term will contribute considerably to the total effect, but remain very small in absolute terms.
The sensitivity of the beat frequency to tilts of the experimental setup has been determined experimentally. Therefore, breadboard I carrying the optics has been tilted using the voice coil actuators. The tilt has been varied in the direction of the axis of one resonator, while the tilt for the orthogonal direction was kept constant. Thus, the shift of the beat frequency is determined primarily by the shift of the resonance frequency of one resonator. The resulting sensitivities of the beat frequency were on the order of 140 mHz/μrad for the y-axis and 30 mHz/μrad for the x-axis. Thus, they are on the order of the estimate for the coefficient $A\nu_0$ and imply a symmetry factor of 0.018, respectively 0.004. However, a determination of the sensitivities in this way can be falsified by linear drifts. More precise is a determination of the sensitivities via the modulation of the tilt upon rotation.

Upon rotation of the experimental setup the tilt will usually be modulated. If the rotation axis is perfectly aligned parallel to the direction of gravity, then the overall tilt α of

the resonator versus the horizontal is equal to the tilt α_r of the resonator versus the plane of rotation and no modulation will occur. However, if the baseplate of the rotation table, and thus the axis of rotation, is tilted by an angle α_b (compare fig. 4.2), then the overall tilt of the resonator versus the horizontal is given by

$$\alpha(t) = \alpha_r + \alpha_b \cdot \sin \omega_{rot} t. \tag{4.7}$$

Therefore, the modulation of the beat frequency upon rotation of the setup due to a tilted rotation axis will be given by

$$\begin{aligned} \frac{\Delta\nu(t)}{\nu_0} &= A \cdot \alpha_b \sin \omega_{rot} t + B \cdot (\alpha_b \sin \omega_{rot} t)^2 \\ &= A \cdot \alpha_b \sin \omega_{rot} t + B \cdot \alpha_b^2 (\frac{1}{2} - \cos 2\omega_{rot} t). \end{aligned} \tag{4.8}$$

As has been shown the sensitivity coefficient B, describing a systematic effect at twice the rotation frequency, is extremely small and leads to negligible contributions, if we can ensure sufficiently small tilt modulations on the μrad scale via active control.

The influence of a varying tilt as described above on the beat frequency between the two resonators can be measured easily, and the sensitivity coefficients can be derived experimentally. Thus, upon evaluation of the raw data the influence of residual tilt variations as measured with the tilt sensors can then be subtracted from the frequency data using this sensitivity.

The determination of the sensitivity coefficient is performed before every measurement run almost automatically. Upon start of the measurement the baseplate of the rotation table has to be tilted by a sufficient amount (≈ 50 μrad) to allow for a detectable modulation of the frequency. Since the frequency shifts linear with a change of the tilt (neglecting B), one can use the determined sensitivity to calculate the effect of small residual tilt variations during the measurement. The baseplate of the rotation table is therefore tilted manually using the air springs of the stabilization system described in chapter 3.6.1. Then the main programs controlling the rotation table and reading the beat frequency and the tilt of the optical breadboard are started. The data of the first five rotations is stored in a file and is used to calculate the sensitivity coefficients. Figure 4.3 shows an example of the data obtained by this procedure.
In a first step the amplitudes of the beat frequency modulation and the tilt modulations are extracted by fitting the function

$$f(t) = f_0 + f_1 \cdot t + f_2 \sin \omega t + f_3 \cos \omega t + f_4 \sin 2\omega t + f_5 \cos 2\omega t \tag{4.9}$$

to the respective time series' yielding four amplitudes for every observable, two for ω_{rot} modulations and two for $2\omega_{rot}$ modulations. Furthermore a linear drift term is included in

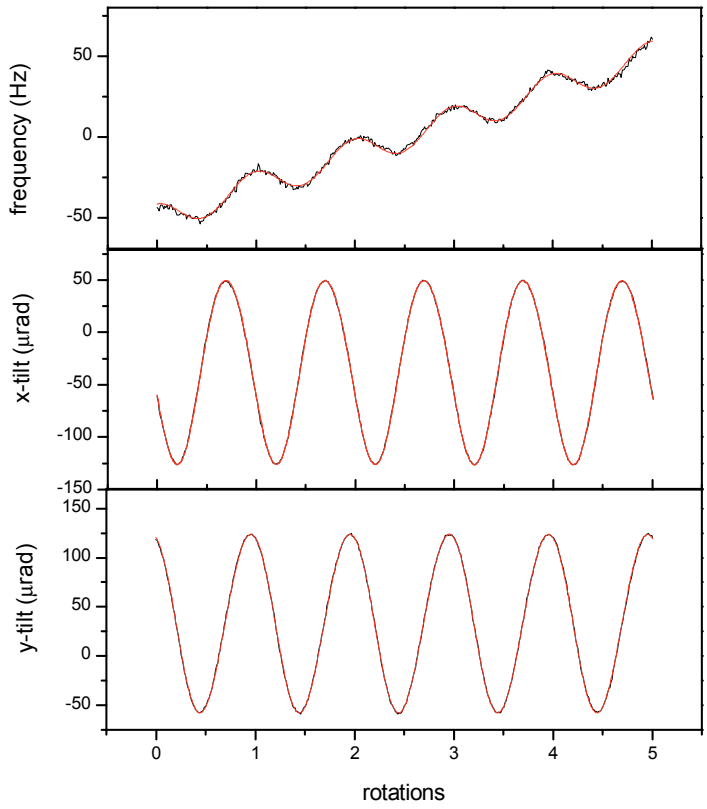

Figure 4.3.: *Modulation of the beat frequency resulting from modulated tilts in x and y direction.*

the fit to account for thermal drifts of the beat frequency.

The beat frequency modulations $\Delta\nu$ are connected to the modulations of the tilt $\Delta\alpha_x$, $\Delta\alpha_y$ via a system of linear equations, which can be arranged according to

$$\begin{pmatrix} \Delta\nu_{\sin\omega t} \\ \Delta\nu_{\cos\omega t} \\ \Delta\nu_{\sin 2\omega t} \\ \Delta\nu_{\cos 2\omega t} \end{pmatrix} = \begin{pmatrix} \Delta\alpha_{x,\sin\omega t} & \Delta\alpha_{y,\sin\omega t} & 0 & 0 \\ \Delta\alpha_{x,\cos\omega t} & \Delta\alpha_{y,\cos\omega t} & 0 & 0 \\ 0 & 0 & \Delta\alpha_{x,\sin 2\omega t} & \Delta\alpha_{y,\sin 2\omega t} \\ 0 & 0 & \Delta\alpha_{x,\cos 2\omega t} & \Delta\alpha_{y,\cos 2\omega t} \end{pmatrix} \cdot \begin{pmatrix} A_{x,\omega} \\ A_{y,\omega} \\ A_{x,2\omega} \\ A_{y,2\omega} \end{pmatrix}. \quad (4.10)$$

This system of equations has to be solved for the unknown sensitivity coefficients $A_{x,\omega}$,

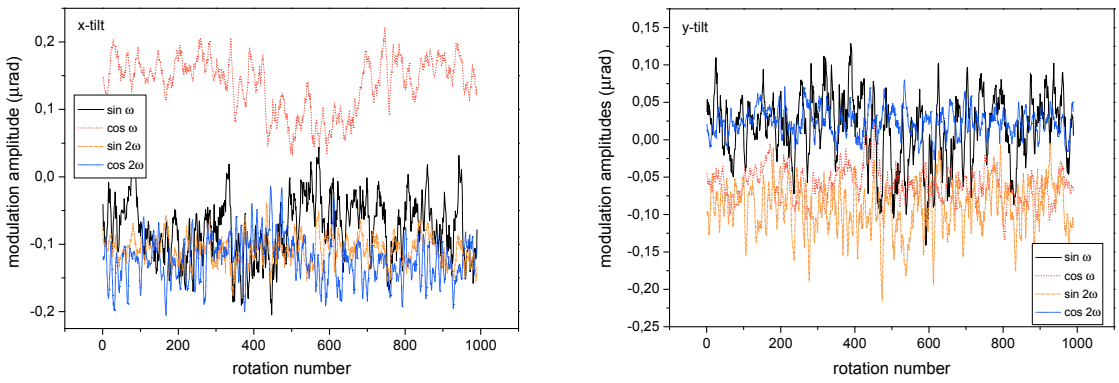

Figure 4.4.: *Residual modulations of the tilt of breadboard I carrying the optical system for x-axis tilt (left, $\Delta\alpha_x$) and y-axis tilt (right, $\Delta\alpha_y$). The maximum amplitude is about 0.2 μrad.*

$A_{y,\omega}$, $A_{x,2\omega}$ and $A_{y,2\omega}$. Generally, the sensitivity coefficients determined for the modulations at 2ω exhibit large error bars since the amplitudes of the modulation are very small. Therefore only the coefficients at ω are used for the decorrelation of possible tilt influences.

The values usually obtained for the sensitivity of the beat frequency to tilt modulations are about $A_{x,\omega} \approx 20$ Hz/mrad and $A_{y,\omega} \approx 120$ Hz/mrad, but from run to run (i.e. every 3-5 days) variations occur on a scale of $\approx \pm 15\%$. Since we determine the tilt coefficients only once at the beginning of a measurement run, and not repeatedly during the whole run, we take this typical variation as a systematic error in the tilt sensitivities. The effect of this systematic error on the beat frequency depends on the residual amount of tilt modulations during the measurement run, which are generally well below 1 μrad. Figure 4.4 shows the residual tilt modulation amplitudes during one measurement run. A moving average over 10 points has been used to smooth the data. On average the residual amplitudes at the different Fourier components are below 0.2 μrad, thus in worst case a systematic error of $\approx \pm(0.018\ \text{mHz}/\mu\text{rad} \cdot 0.2\ \mu\text{rad}) = \pm 3.6$ mHz will occur, which is $\approx \pm 1.3 \cdot 10^{-17}$ relative to the laser frequency. However, for different datasets the systematic error varies and one may assume partial cancellation of the effect.

4.2. Centrifugal Forces

Similar to the case of a varying tilt a varying angular velocity of the rotation can lead to systematic effects if the modulations are occuring at the period of rotation. This is due to the associated centrifugal forces acting on the resonator structure and on the optical

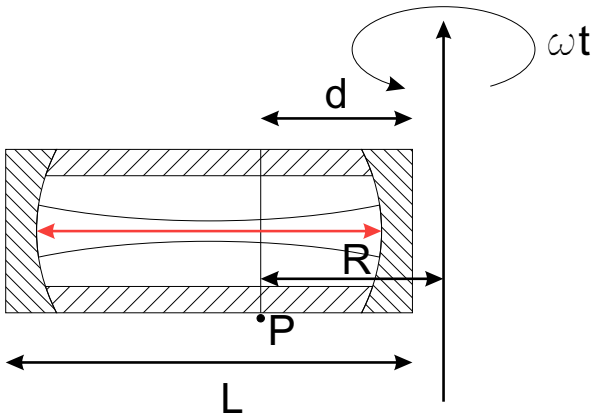

Figure 4.5.: *Schematic of the resonator block fixed at a distance d from the axis of rotation.*

elements of the system. The length of the resonator will be modulated according to the radial acceleration present, thus the resonance frequency will be modulated, too. Bending of the optical elements may cause a variation of the beam alignment, which can as well cause a shift of the resonance frequency.
Furthermore the reading of the tilt sensor used for the stabilization of the tilt of the optical setup can be affected by the varying radial accelerations present. This effect is however minimized in the current setup by the position of the tilt sensor, which is almost perfectly sitting on the axis of rotation.

For the resonator block a rough estimate for the size of the effect can be derived as a function of the angular velocity of the rotation. For simplicity we consider the case of a rectangular block without through bores and just consider one dimension as depicted in figure 4.5 and already done when discussing tilt effects. We assume the block of length L to be fixed in a single point P on the rotation table with the axis of the resonator being aligned in radial direction. The point P is located at a distance R from the axis of rotation. Effectively no force is acting on the block in this point, which is not necessarily located at the center of the resonator structure, but may be apart from it by the length $L/2 - d$. Thus the inner end of the block is at a distance $a = R - d$, the outer end at a distance $b = R + L - d$ from the axis of rotation. Let ρ be the density of the material ($2.21 \cdot 10^3$ kg/m^3 for ULE) and E Young's modulus ($67.7 \times 10^9 Nm^{-2}$), then for an angular velocity ω the deformation due to the centrifugal forces is for a layer of thickness dr at a position r given by

$$d\left(\frac{\Delta L}{L}\right) = \frac{\rho\omega^2}{E} r dr \tag{4.11}$$

Integration of the formula over the extension of the whole block yields the relative change of the resonator block. Two cases have to be distinguished:

- The center of the resonator block is shifted by more than $L/2$ from the axis of rotation ($R > d$).
- The center is shifted by less than L/2 from the axis of rotation ($R < d$).

For the first case the integration has to be split into two parts. The inner part of the resonator (closer to the axis of rotation) is compressed due to the centrifugal forces and the fixation in the point P, while the outer part of the resonator is elongated. The two parts of the integral are given by

$$\begin{aligned}
\frac{\Delta L_{in}}{L_{in}} &= -\int_{R-d}^{R} \frac{\rho\omega^2}{E} r dr \\
&= -\frac{\rho\omega^2}{2E} \cdot [2Rd - d^2], \qquad (4.12) \\
\frac{\Delta L_{out}}{L_{out}} &= +\int_{R}^{R+L-d} \frac{\rho\omega^2}{E} r dr \\
&= \frac{\rho\omega^2}{2E} \cdot [2R(L-d) + (L-d)^2]. \qquad (4.13)
\end{aligned}$$

The shift of the resonance frequency of the resonator is therefore for a fixed angular velocity ω given by

$$\Delta\nu = -\nu_0 \frac{\Delta L_{out} + \Delta L_{in}}{L} = -\nu_0 \cdot \frac{\rho\omega^2}{2E} \cdot [L^2 + 3d^2 - 4Rd - 4Rd + 2RL - 3Ld].$$

For the second case we may assume for simplicity that the point P is lying directly on the axis of rotation and that the center of the block is shifted by a distance D from the axis of rotation. Then both parts of the resonator will be elongated due to the centrifugal forces. The two contributions of the elongated parts are given by

$$\begin{aligned}
\frac{\Delta L_1}{L_1} &= +\int_{0}^{L-D} \frac{\rho\omega^2}{E} r dr \\
&= \frac{\rho\omega^2}{2E} \cdot (L-D)^2, \\
\frac{\Delta L_2}{L_2} &= +\int_{0}^{L+D} \frac{\rho\omega^2}{E} r dr \\
&= \frac{\rho\omega^2}{2E} \cdot (L+D)^2. \qquad (4.14)
\end{aligned}$$

Thus the total change of the resonator length is given by

$$\begin{aligned}
\frac{\Delta L}{L} &= \frac{\rho\omega^2}{2E} \cdot \frac{(L-D)^3 + (L+D)^3}{L} \\
&= \frac{\rho\omega^2}{E} \cdot [3D^2 + 2L^2]. \qquad (4.15)
\end{aligned}$$

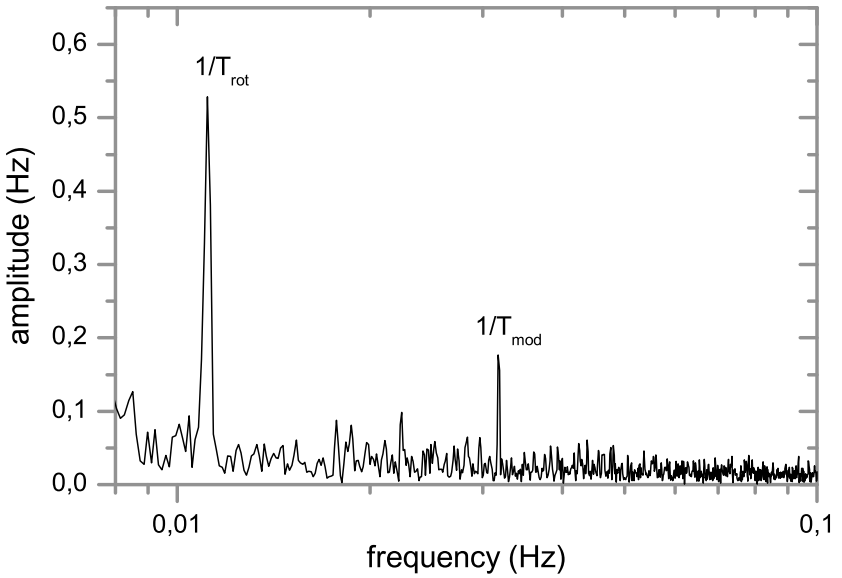

Figure 4.6.: *Fourier transform of frequency data from a dataset with modulated rotation speed. A linear drift has been subtracted. At the rotation frequency a residual systematic effect is on the order of 0.55 Hz, while the systematic effect due to the modulation of ω is on the order of 0.2 Hz.*

For a typical rotation period of 90 s and our resonators this effect is on the order of $2.5 \cdot 10^{-12}$, while a calculation for the first case would yield slightly smaller values.
The effect of a varying angular velocity on the beat frequency between the two resonators has been determined experimentally by modulating the rotational speed sinusoidally. Figure 4.6 shows the effect of a modulation on the frequency noise of the beat. The set mean angular velocity of $\omega = 2\pi/90s$ has been modulated by $\pm$10% of its value. The modulation period for this measurement was chosen to be 31 s to be able to separate the velocity modulation effect from other systematic influences (tilt etc.). The two models described above yield for a single resonator a value between ± 50 Hz and ± 70 Hz for this strong modulation. However, the similar positioning of the two resonators leads to a strong suppression of these centrifugal effects when measuring the beat frequency. The rather strong applied modulation led to a variation of the beat frequency on the order of 0.2 Hz, corresponding to a fractional variation of $7 \cdot 10^{-16}$.

Figure 4.7 shows the relative Allan deviation of the rotational velocity as derived from a dataset acquired via the servo controller of the rotation table. The relative instability is on a level of $1.5 \cdot 10^{-5}$ at an integration time of 24 s. Thus, with the derived sensitivity

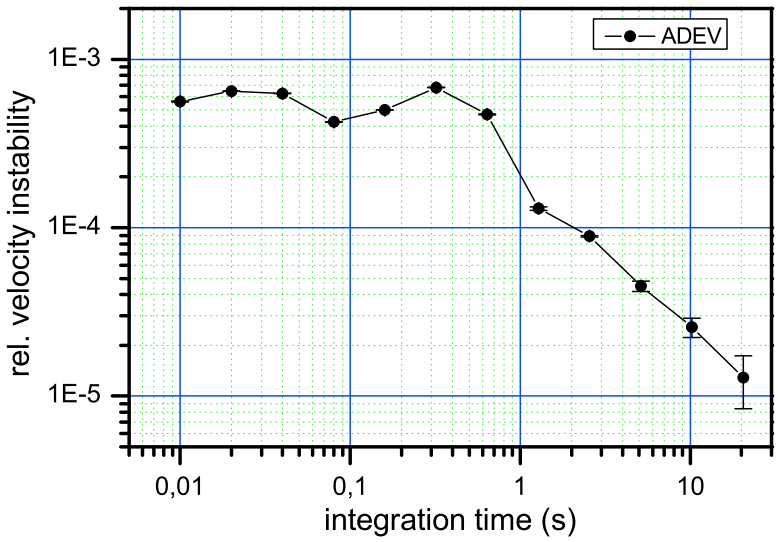

Figure 4.7.: *Relative instability (relative Allan deviation) of the angular velocity at a set period of 90 s. The raw data was acquired directly from the servo system.*

of $\approx 0.2\ Hz/10\%$ we can estimate the frequency instability due to the instability of the rotation rate to be $\approx 3 \cdot 10^{-4}$ Hz for $\tau = 24$ s. This corresponds to a fractional instability of $1.1 \cdot 10^{-18}$ on the timescale of interest. Thus, at the current state of the setup we consider effects stemming from a varying rotation rate to be completely negligible.

4.3. Power Fluctuations

A varying power of the laser light circulating inside the resonator can lead to shifts of the resonance frequency ν_0 of the resonator due to heating effects of the mirror coatings and the substrate. A measurement of the corresponding sensitivity of the beat frequency to fluctuations in the power of each resonator has been performed by varying the circulating power via a modulation of the RF power of the AOM's used as frequency shifters for the finelocks. The power transmitted through the resonators as well as the beat frequency were recorded. Figure 4.8 shows such a measurement.
At the very beginning of our measurements in 2008 this sensitivity coefficient was on the order of 30 Hz/μW for both resonators. However, as was already reported in chapter 3, a failure of the vacuum system occured late in summer 2008. After this failure the sensitivity

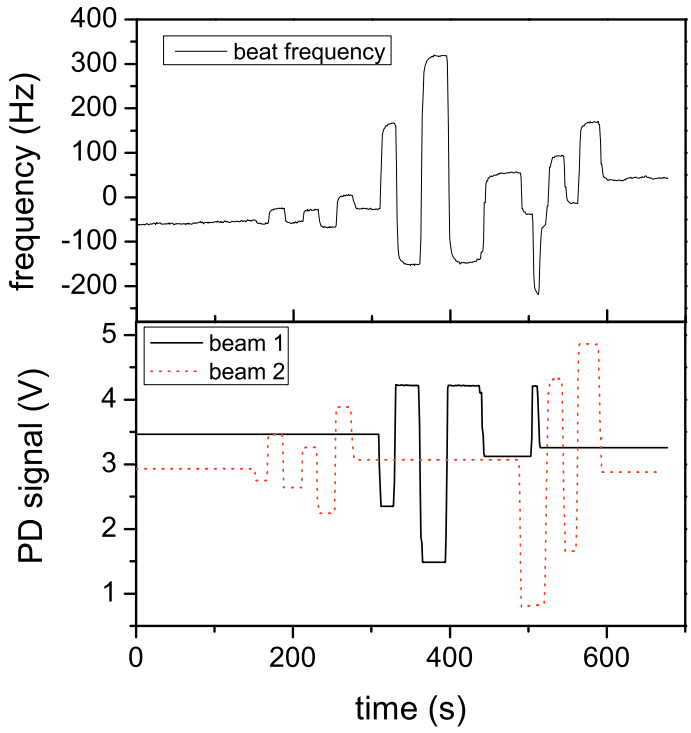

Figure 4.8.: *Determination of the sensitivity of the beat frequency to power changes by stepwise changes of the transmitted laser power. PD = photodiode*

to power fluctuations had increased for one resonator. From the applied modulations (see figure 4.8) one can derive a sensitivity of $(+54 \pm 5)$ Hz/V for resonator 2, respectively (-170 ± 10) Hz/V for resonator 1 (beam 1) to power fluctuations as measured with our photodiodes. The transmitted power through the resonators is approximately 5 μW resulting in photodiode signals of 3 V, thus the power sensitivity is on the order of 30 Hz/μW, respectively 100 Hz/μ W.

The power sensitivity of the beat frequency to modulations of the transmitted power of the prestabilization beam is hard to measure, since a decrease in the power leads to a smaller slope of the error signal, which increases the residual amount of frequency noise and can cause the laser frequency to be unlocked. However, a rough estimate can be derived by small power variations, yielding a sensitivity of $\approx (-150 \pm 50)$ Hz/V.

As has been described in chapter 3.4, the power is stabilized using the amplitude modulation input of the RF-synthesizers driving the AOM's, respectively the fixed frequency driver for the prestabilization beam. Figure 3.17 showed the residual instability of the transmitted

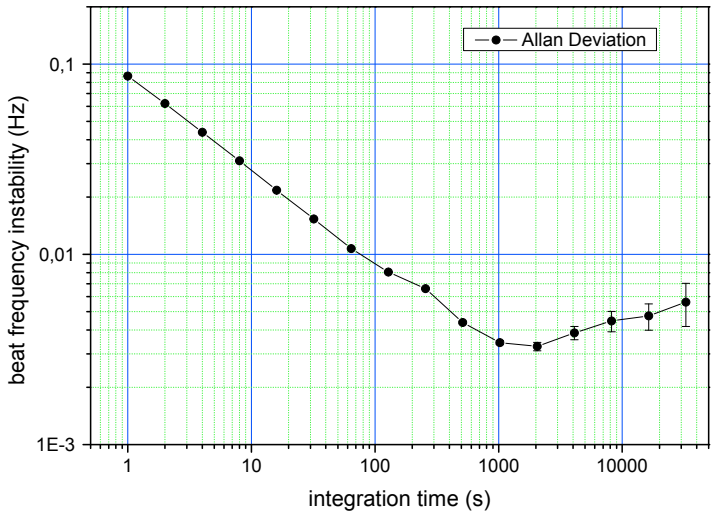

Figure 4.9.: *Instability of the beat frequency inferred from the power fluctuations of figure 3.17.*

laser powers. Figure 4.9 shows the inferred beat instability occuring due to these power fluctuations for this dataset. At an integration time of 1 s the power fluctuations cause an instability of the beat frequency of ≈ 0.14 Hz. On the timescale of half a rotation the instability averages down to a level of ≈ 0.02 Hz, corresponding to a relative instability of $7 \cdot 10^{-17}$.

The systematic effect of power fluctuations can be derived as has been done for the tilt modulations by analyzing the amplitudes of the sine and cosine modulations at an angular frequency of $2\omega_{rot}$. Figure 4.10 shows exemplarily for one dataset the power modulation amplitudes as obtained using the standard fit function.The determined amplitudes for beam 1 and beam 2 reach values of up to several times 10 μV. The derived effect on the beat frequency would thus be on the order of several mHz, or relative to the frequency ν_0 a few parts in 10^{17}. However, as can be seen from figure 4.10, the effect averages out already about the extent of a single dataset since the modulations have no preferred signature. The residual effect depends on the specific coefficient to be determined.

The coefficient $(\tilde{\kappa}_{e-})^{ZZ}$ is determined by an offset in the determined amplitude $2C\nu_0$, the error is thus given by the average amplitudes of the modulation. For the shown (typical) dataset this is on a level of 1 μV, corresponding to an effect on the average frequency modulation amplitude of ≈ 0.2 mHz, in relative numbers $6 \cdot 10^{-19}$. Thus it is negligible.

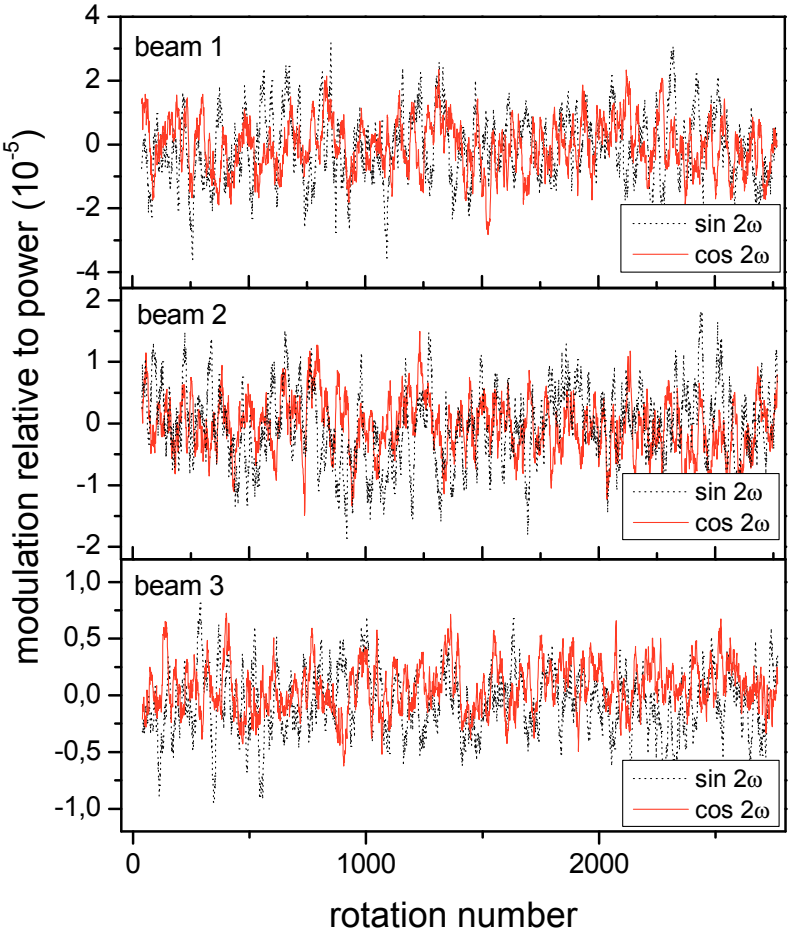

Figure 4.10.: *Amplitudes of the power modulation for all beams. Displayed are the* $\sin 2\omega$ *and the* $\cos 2\omega$ *amplitudes. The data was slightly smoothed to remove fluctuations on the order of the fit errors.*

For the coefficients determined via the sidereal day variation of the beat frequency the effect can be determined via the effect on the Fourier-amplitudes. This is for the given dataset on the order of 4 μV, corresponding to 0.7 mHz or $2.4 \cdot 10^{-18}$ in relative numbers.

4.4. Frequency Drifts

A possible source of systematic errors on the determined coefficients is the effect of long term drifts of the beat frequency. Clearly a purely linear drift will not influence in any way the determined amplitudes for the modulation, since it can be easily removed from the data for every single rotation. This is usually done in the analysis. However, this is not the situation one faces in the experiment.
Usually one faces a daily modulation of the beat frequency due to variations in the ambient temperature with a period which roughly corresponds to a solar day. The average value of the beat frequency stays almost the same from day to day, and a typical peak to peak variation is 20 kHz over the course of a day (see top left of figure 4.11).
To model which effect the nonlinearity of the drift will have on the data, we prepare a test dataset comparable to real measurement data, where a modulation of the beat with a period of one solar day, respectively one sidereal day, and an amplitude of 10 kHz is added. Thus we first produce a data list with 1 s spacing between adjacent datapoints. Then this list is split into intervals of 90 datapoints, corresponding to a full rotation of the table with usual settings. To each of these data intervals we fit the function

$$\nu(t) = \nu_0 + at + 2B\nu_0 \cdot \sin\frac{4\pi t}{90\text{ s}} + 2C\nu_0 \cdot \cos\frac{4\pi t}{90\text{ s}} + D\nu_0 \cdot \sin\frac{2\pi t}{90\text{ s}} + E\nu_0 \cdot \cos\frac{2\pi t}{90\text{ s}}, \quad (4.16)$$

yielding the amplitudes which would appear as a shift of the determined amplitudes in the normal data analysis. It has to be noted however, that this is a worst case scenario, since the daily modulation will vary over the course of the year and one can expect the effect to average out partly.

Figure 4.11 shows the used modulation and the determined values for all fit parameters over the course of one day. For the given modulation we get a drift modulation with an amplitude of 10 kHz$\cdot 2\pi/86400$ s≈ 0.7 Hz/s. For the modulation amplitudes at 2ω we get peak values of 5.4 mHz for the $\cos 2\omega$-amplitude ($2C\nu_0$) and -0.38 mHz for the $\sin 2\omega$-amplitude ($2B\nu_0$) corresponding to a fractional beat modulation of $\pm 1.9 \cdot 10^{-17}$, respectively $\pm 1.4 \cdot 10^{-18}$.

A phase shift in the assumed daily modulation will just shift the phase of the modulation of the fitted parameters accordingly. However, the influence on the final result, the RMS-parameter and the SME-parameters, might change strongly. Therefor we continue with the analysis and deduce the systematic shift of the final values by simulating measurement data with the shown behaviour over the course of a whole year. Since our data doesn't cover the whole year we only produce simulated data points at times where we have as well real data points. This simulated data is processed via a single step fit routine directly fitting the time variations predicted by the two test theories.
The effect of the simulated periodic beat frequency variation is summarized in table 4.1 for

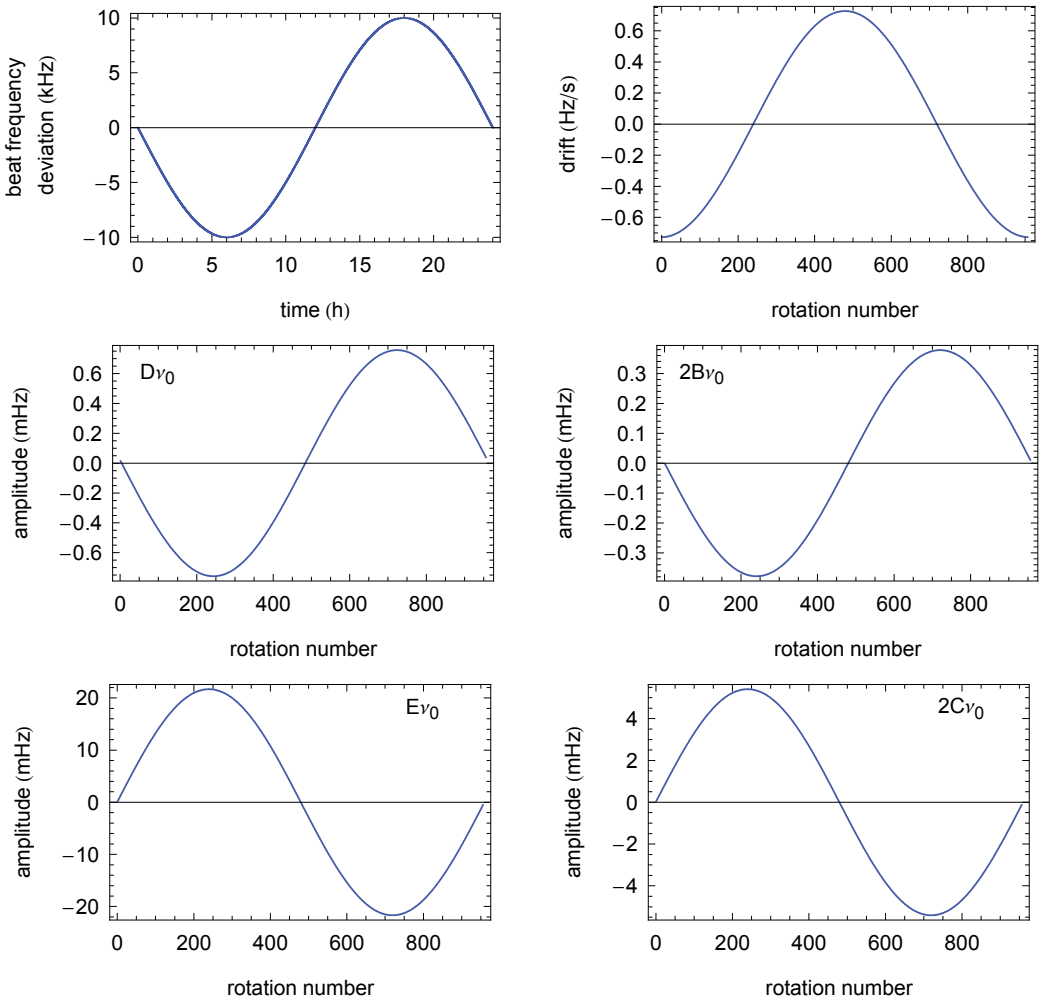

Figure 4.11.: *Estimation of the influence of a typical daily beat frequency modulation (top row) on the modulation amplitudes.*

different cases. For all cases we assumed the modulation of the $2B$ and $2C$ coefficients to be

$$\begin{aligned} 2B(t)\nu_0 &= -0.38 \times 10^{-3}\ \text{Hz} \cdot \sin \omega t \\ 2C(t)\nu_0 &= 5.5 \times 10^{-3}\ \text{Hz} \cdot \sin \omega t, \end{aligned}$$

The calculation has been performed for a periodic modulation at a solar period ($\omega = \omega_{solar}$), as should be the case for this type of systematic effect, and for a periodic modulation at the sidereal frequency ($\omega = \omega_{\oplus}$). This has been done since the two frequencies are almost identical and the systematic modulation might not exactly occur at a solar period. A systematic sidereal modulation however will have a stronger impact on the final results, as can

parameter	$\sin\omega_{solar}t$	$\cos\omega_{solar}t$	$\sin\omega_{\oplus}t$	$\cos\omega_{\oplus}t$
$(\tilde{\kappa}_{e-})^{ZZ}$	(2.5 ± 0.6)	(49 ± 1)	(-4.9 ± 0.5)	(-6.0 ± 0.5)
$(\tilde{\kappa}_{e-})^{XY}$	(0.35 ± 0.24)	(0.44 ± 0.32)	(-1.7 ± 0.2)	(-0.9 ± 0.2)
$(\tilde{\kappa}_{e-})^{XZ}$	(-2.9 ± 0.4)	(3.2 ± 0.5)	(11.3 ± 0.3)	(-182.3 ± 0.3)
$(\tilde{\kappa}_{e-})^{YZ}$	(-2.0 ± 0.3)	(-50 ± 1)	(-179 ± 0)	(-11.8 ± 0.3)
$(\tilde{\kappa}_{e-})^{XX} - (\tilde{\kappa}_{e-})^{YY}$	(-1.8 ± 0.5)	(-13 ± 1)	(2.1 ± 0.5)	(1.8 ± 0.5)
$\beta_{\oplus}(\tilde{\kappa}_{o+})^{XY}$	(-180 ± 4)	(12 ± 1)	(0.8 ± 0.3)	(-0.2 ± 0.4)
$\beta_{\oplus}(\tilde{\kappa}_{o+})^{XZ}$	(6.6 ± 0.2)	(-3.6 ± 0.3)	(-0.2 ± 0.2)	(2.4 ± 0.2)
$\beta_{\oplus}(\tilde{\kappa}_{o+})^{YZ}$	(-8.9 ± 0.2)	(-24 ± 0)	(3.6 ± 0.2)	(-0.7 ± 0.2)
$(\beta - \delta - 1/2)$	(3.9 ± 0.2)	(3.2 ± 0.2)	(0.7 ± 0.2)	(11.0 ± 0.2)

Table 4.1.: *SME and RMS model parameters for the case of a pure sinusoidal beat frequency modulation.* $(\tilde{\kappa})$*-values are in* 10^{-19}*, the RMS-parameter* $\beta - \delta - 1/2$ *in* 10^{-13}*.*

be seen from the values shown in table 4.1.

The values show that in worst case a shift in the parameter values as big as $1.8 \cdot 10^{-17}$ might occur for the $(\tilde{\kappa})$-matrices, while the shift for the RMS-parameter is in worst case $1 \cdot 10^{-12}$. These are values on the order of the expected sensitivity of the apparatus. However this resembles a worst case scenario and one might use half of the maximum value as additional systematic error bar for the determined coefficients.

Alternatively one may try to remove the influence of the longterm drift of the beat frequency on the determined modulation amplitudes at the frequency ω_{rot} of active rotation and its second harmonic $2\omega_{rot}$. Therefore in a first step all raw datasets have been smoothed using a lowpass filter. Then the resulting dataset is split into single rotations, as is done with the original dataset, and the model

$$\nu(t) = \nu_{off} + a \cdot t + 2C\nu_0 \cos 2\omega_{rot}t + 2B\nu_0 \sin 2\omega_{rot}t + D\nu_0 \cos\omega_{rot}t + E\nu_0 \sin\omega_{rot}t \quad (4.17)$$

is fitted to the respective time series yielding the modulation amplitudes at ω_{rot} and $2\omega_{rot}$. These amplitudes are now only due to the longterm drift of the frequency, and not connected to the modulation due to the active rotation. Therefore they may be subtracted from the modulation amplitudes obtained from the original dataset and the modified dataset may be used for further evaluation of the data.

type	sensitivity of beat frequency	typ. modulation ampl./instab.		syst. effect		syst. effect @$2\omega_{rot}$ rel. to ν_0
		@ω_{rot}	@$2\omega_{rot}$	@ω_{rot}	@$2\omega_{rot}$	
resonator tilt	120 mHz/μrad (y-axis)	0.2 μrad	0.2 μrad	24 mHz	24 mHz	$8.5 \cdot 10^{-17}$
	30 mHz/μrad (x-axis)	0.2 μrad	0.2 μrad	6 mHz	6 mHz	$2 \cdot 10^{-17}$
after decorr.				≈ 3.6 mHz	≈ 3.6 mHz	$1.3 \cdot 10^{-17}$
centrifugal forces	≈ 0.2 Hz/10% rot. vel. change	$8 \cdot 10^{-6}$	$1.5 \cdot 10^{-5}$	≈ 0.2 mHz	≈ 0.3 mHz	$\approx 1 \cdot 10^{-18}$
power variations	0.17 Hz/mV	$\leq 30\mu$V	$\leq 30\mu$V	≤ 5 mHz	≤ 5 mHz	$\leq 1.8 \cdot 10^{-17}$
	0.05 Hz/mV	$\leq 20\mu$V	$\leq 20\mu$V	≤ 1 mHz	≤ 1 mHz	$\leq 0.4 \cdot 10^{-17}$
	0.15 Hz/mV	$\leq 2\mu$V	$\leq 2\mu$V	≤ 0.3 mHz	≤ 0.3 mHz	$\leq 0.1 \cdot 10^{-17}$
observed effect (mean of $1.35 \cdot 10^5$ rotations)				0.55 Hz	$\leq (10 \pm 2)$ mHz	$(3.6 \pm 0.7) \cdot 10^{-17}$

Table 4.2.: *Overview over the size of different systematic influences perturbing the measurement of the beat frequency during a single rotation. The influence of tilt variations is decorrelated from the data during the analysis. An unidentified systematic effect is observed leading to an offset in the amplitudes $2B\nu_0$ at $2\omega_{rot}$ of $\approx (10 \pm 2)$ mHz (statistical error).*

4.5. Summary

Different systematic influences disturbing the measurement of the beat frequency have been discussed in the preceding sections. Here a short summary of the overall influence on the measurement is given. Table 4.2 lists the typical magnitude of the different effects on a timescale of one rotation. The main systematic influence is the variation of the breadboard tilt. It is decorrelated from the data using the sensitivity coefficients determined before every measurement run, but due to the uncertainty of the determined sensitivities a residual systematic error on the order 15% of the original value remains. The systematic effect averages out when many runs are included in the analysis.
Contrary is the situation for effects due to power fluctuations and the centrifugal forces. These average out quickly over the course of several rotations.
Additionally to these effects occuring on the timescale of rotation, a daily varying frequency drift may lead to an effect on some coefficients of the SME and on the RMS parameter, which are determined via sidereal modulation amplitudes. The effect of this on our data will be discussed in chapter 5.
Unfortunately, the systematic errors listed above do not account for all systematics observed in our measurements. The determined modulation amplitudes at the frequency ω_{rot} show a significant offset of 0.5 Hz, respectively -0.2 Hz. The origin of this systematic shift could

not be identified yet, but a thermal origin is suspected. The modulation amplitudes at $2\omega_{rot}$ however are only slightly affected by this systematic effect. The amplitudes $2C\nu_0$ show no significant offset from zero, the amplitudes $2B\nu_0$ show a small offset of 10 mHz.

5. Analysis and Results

5.1. Measurements

During the course of this work the experimental setup has been modified several times to improve the stability of the system and to reduce systematic effects. First work on the setup had started in November 2004, when nothing but the bare resonators and a first vacuum chamber were present in the laboratory. In the early stage of the experiment (before may 2007) we utilized a ball bearing rotation table, which was taken from the cryogenic setup of [20]. However, this was still in use in the cryogenic setup till late in 2005 and only then it could be implemented in our setup. Starting from the middle of 2006, when all servo systems necessary to suppress systematic effects were present, we performed first test measurements with the rotating setup. Till march 2007 we characterized the setup and took first data, which could be analyzed according to the SME and the RMS test theory. These first results and characterization measurements have been published in [68].

Generally for all our measurements the frequency difference between the two resonators is sampled with a gating time of 1 s using a frequency counter. At the same time several other data such as the rotation angle of the table, tilts of the setup and powers transmitted through the cavities, are recorded and stored in one file together with the beat frequency. In total, three computers control the apparatus and acquire the data, which is partly communicated between the computers via the local TCP/IP network. To ensure identical timestamps for the datapoints all these computers are synchronized to the time server provided by the university.
For the first measurements described above the whole setup was rotated with a period of 240 s. At this period a compromise between a short duration of a single rotation and a low vibration level of the ball bearing rotation table was found. In the time between October 2006 and December 2006 we have taken approximately 3000 rotations in five measurement sets. The data was analyzed according to equation 2.19. For every rotation the systematic influence induced by a varying tilt was subtracted according to the sensitivity determined before the measurement. Then for every rotation the function

$$\Delta\nu(\theta(t)) = \nu_{off} + a\cdot t + 2B\nu_0 \sin 2\theta(t) + 2C\nu_0 \cos 2\theta(t) + D\nu_0 \sin\theta(t) + E\nu_0 \cos\theta(t) \quad (5.1)$$

was least-squares-fitted to the measured data yielding the desired modulation amplitudes $2B\nu_0$ and $2C\nu_0$ at $2\omega_{rot}$. The histograms corresponding to the datasets are shown in figure 5.1. For both amplitudes the histograms exhibit a width of ≈ 2 Hz corresponding to a fractional 1σ uncertainty of $7\cdot 10^{-15}$, which represents approximately the level of sensitivity

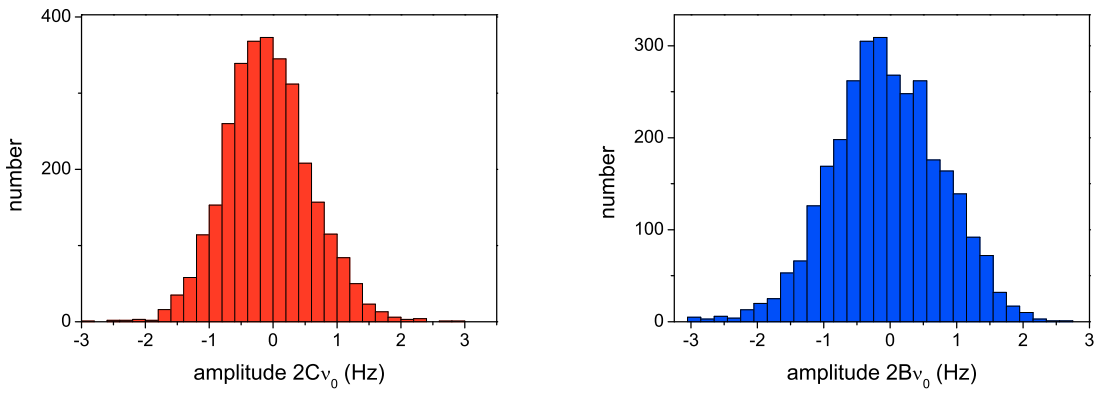

Figure 5.1.: *Histograms of the modulations amplitudes $2B\nu_0$ and $2C\nu_0$ for first measurements performed during autumn 2006.*

to an isotropy violation for a single rotation measurement.
From the described dataset we could derive a value for the SME coefficient $(\tilde{\kappa}_{e-})^{ZZ}$ under the assumption that all other coefficients vanish. For this case the determined value is

$$(\tilde{\kappa}_{e-})^{ZZ} = (-1.0 \pm 2.3) \cdot 10^{-15}, \tag{5.2}$$

giving an upper limit (1σ) for the magnitude of $(\tilde{\kappa}_{e-})^{ZZ}$ of

$$|(\tilde{\kappa}_{e-})^{ZZ}| \leq 3.3 \cdot 10^{-15}. \tag{5.3}$$

This value was already significantly better than previous results obtained in our group with a cryogenic setup.

5.1.1. Reconstruction

In April 2007 our new air bearing rotation table was delivered. During a phase of approximately half a year the setup was disassembled, the rotation table was set up, and then the whole setup was assembled again. To control the motion of the rotation table new software had to be written. In late 2007 we could start with measurements again, which were already better than with the old table. In spring 2008 we could slightly improve the quality of the data. Since then we took data of almost constant quality, which will be presented in the next sections. Only for the period may/june 2008 no data is available, since during this time the setup was equipped with an active stabilization system for the tilt of the rotation table baseplate as described in chapter 3.6.1. From the beginning of march 2008 till April 2009 we continuously collected data. For the determination of the coefficients describing a possible Lorentz Invariance violation, we can use 46 datasets longer

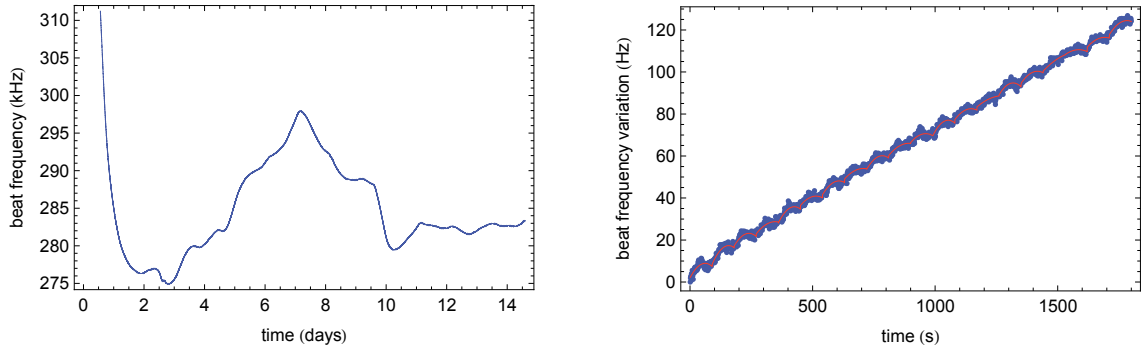

Figure 5.2.: *Left: Raw frequency data of a measurement run of 14 days performed during the Christmas break 2008 from December 19th, 2008 till January 2nd, 2009. The measurement run includes ≈12 000 rotations. At the time $t = 0$ the apparatus was closed after having been open for several days. Thus the temperature rises at the beginning leading to big drifts. Right: small fraction of the data together with the fitted modulations.*

than 24 hours. The raw data of one of the measurement runs is shown in figure 5.2 (left side) containing approximately 12000 rotations. The right side of the figure shows a small part of the data together with modulations fitted to the data.

5.2. Fit Procedures

The analysis of the data has been performed in a series of several steps. From step to step we derive one after each other the Fourier-amplitudes at the different frequency scales expected according to the models of the two test theories as described in chapter 2.
In the first step of the analysis we determine for every single rotation the amplitudes of the frequency modulation at twice the frequency ω_{rot} of the active rotation of the setup. As has been mentioned in chapter 4, the most severe systematic effect of known origin is expected to stem from modulations of the resonator tilt upon rotation of the setup. To be able to compensate for the effect of a varying tilt the sensitivity of the beat frequency to tilts of the setup has been determined before every measurement run in an automated way. This sensitivity coefficient is now used to decorrelate the tilt effect from the frequency data before we derive the modulation amplitudes from the frequency data. Therefore the tilt data is weighted with the corresponding sensitivity coefficient and is directly subtracted from the frequency data. Then for every single rotation i of the rotation table we perform a least squares fit of the equation

$$\nu(\theta) = \nu_{off} + a \cdot \theta + 2B\nu_0 \sin 2\theta + 2C\nu_0 \cos 2\theta + D\nu_0 \sin\theta + E\nu_0 \cos\theta \tag{5.4}$$

to the beat frequency data, yielding a series of drift and modulation amplitudes $\{a, B, C, D, E\}^i$.

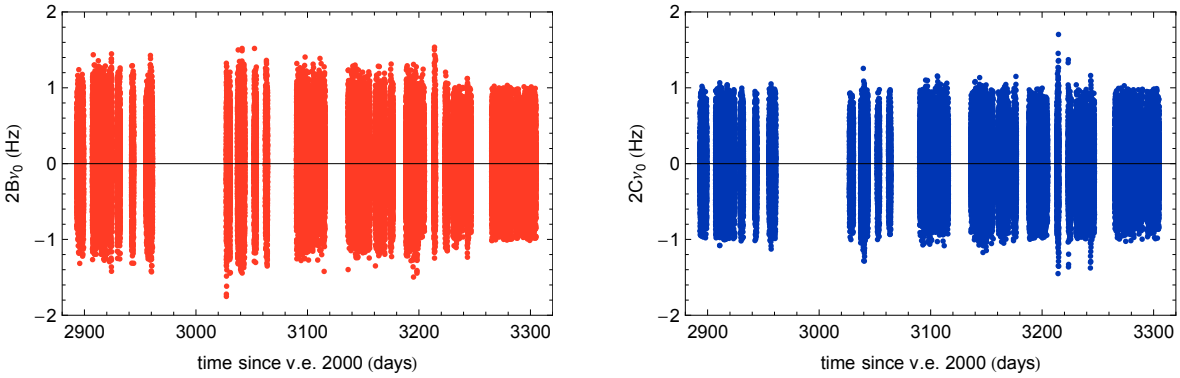

Figure 5.3.: *Time series of the determined modulation amplitudes $2B\nu_0$ and $2C\nu_0$ of the beat frequency upon active rotation of the setup. The series contains approximately 135,000 rotations. v.e. = vernal equinox*

Here the angle θ is the angle of resonator 1 with respect to the laboratory x-direction pointing in southern direction as defined in section 2.3.1. During this fitting step rotations which are clearly disturbed (e.g. jumps in tilt or similar), or where the error of the fit is too large, are omitted. To every set of these amplitudes we attribute a timestamp, which is the time in SI seconds passed since the y-axis of the laboratory system and the Y-axis of the SCCEF (compare section 2.3.1) were coaligned on the day of the vernal equinox in the year 2000[1]. In this way we derive for each single data file the two time series $2B(t)$ and $2C(t)$ as described in chapter 2.3.2, respectively 2.3.3.

Figure 5.3 shows the two time series of the amplitudes $2B^i\nu_0$ and $2C^i\nu_0$ of all the used rotations contained in the 46 datasets after decorrelation of the tilt, while figure 5.4 shows the corresponding histograms together with the fit of a Gaussian distribution to the determined bin values. For the amplitudes $2B^i\nu_0$ the standard deviation is approximately $\sigma = 0.42$ Hz ($\rightarrow$ full width at half maximum ≈ 1.2 Hz), while for the amplitudes $2C^i\nu_0$ the values are $\sigma = 0.34$ Hz (≈ 1 Hz). The center values for the fitted Gaussian distributions are $2\bar{B}\nu_0 = (0.01 \pm 0.001)$ Hz, respectively $2\bar{C}\nu_0 = (0.001 \pm 0.001)$ Hz, indicating a significant systematic effect present on the $2B$-amplitudes.

To be able to assess the effect of the decorrelation of the tilt induced systematic effects, we determine as well the modulation amplitudes for the original dataset. Thus the analysis following this first step can as well be performed for the original dataset without decorrelation of the tilt. For the undecorrelated data the histograms yield an almost identical width, but the center values are shifted. For the $2B\nu_0$-amplitudes the mean of the undecorrelated data is (-0.0036 ± 0.001) Hz, while for the amplitudes $2C\nu_0$ it is (0.0031 ± 0.001) Hz.

[1] the vernal equinox occured on march, 20^{th}, 07:36 UTC

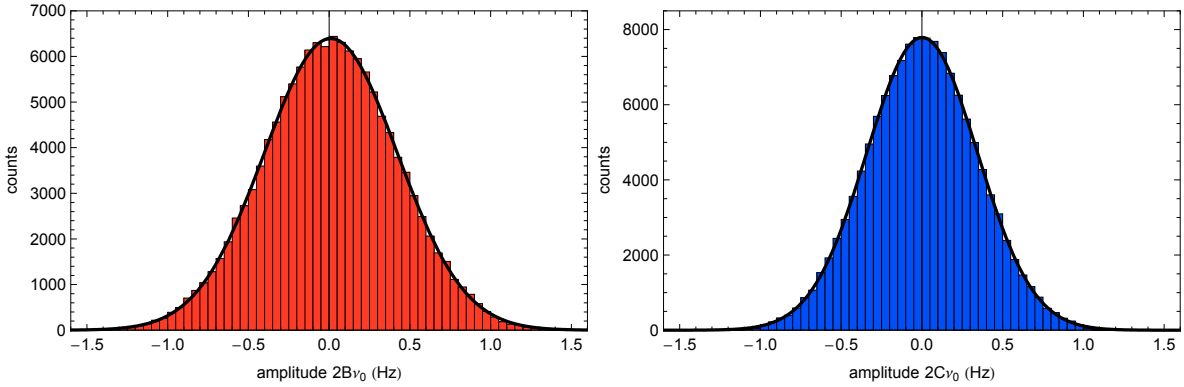

Figure 5.4.: *Histograms of the amplitudes $2B\nu_0$ and $2C\nu_0$. The width of the histograms is 0.84 Hz, respectively 0.7 Hz (1σ). The center values are 10 mHz and 1 mHz.*

As has been shown in chapter 4.4, the potential effect of longterm drifts on the determined amplitudes could, in a worst case scenario, be on the order of a few mHz ($\approx 2 \cdot 10^{-17}$ relative to ν_0). Thus in a second step the data of each data file is analyzed with respect to the influence of these longterm drifts of the frequency on the modulation amplitudes. To derive the actual influence of the drifts we have to filter the data using a lowpass filter. We use a moving average filter extending over 6 rotations (≈ 540 datapoints). This length of the filter is sufficient to completely supress the modulations on the timescale of a rotation and properly reproduces the behaviour of the longterm drifts (compare fig. 5.5). The obtained datasets can now be analyzed as has been done with the original ones yielding modulation amplitudes being determined by the varying drift of the beat frequency only. To determine the influence of the drifts on our final values we may subtract in a further step these amplitudes from the original ones and compare the final outcome of the further analysis.

The next step of the analysis consists in the determination of the modulations on the timescale of a sidereal day. According to the two test theories in case of an anisotropic speed of light modulations are expected to occur at a period of half a sidereal day and at a period of a sidereal day. As has been shown in chapter 2.3.2, the Standard Model Extension predicts a behaviour described by the equations

$$\begin{aligned} B(t) &= B_0(t) + B_1(t)\sin\omega_\oplus T_\oplus + B_2(t)\cos\omega_\oplus T_\oplus \\ &\quad + B_3(t)\sin 2\omega_\oplus T_\oplus + B_4(t)\cos 2\omega_\oplus T_\oplus \\ C(t) &= C_0(t) + C_1(t)\sin\omega_\oplus T_\oplus + C_2(t)\cos\omega_\oplus T_\oplus \\ &\quad + C_3(t)\sin 2\omega_\oplus T_\oplus + C_4(t)\cos 2\omega_\oplus T_\oplus. \end{aligned} \tag{5.5}$$

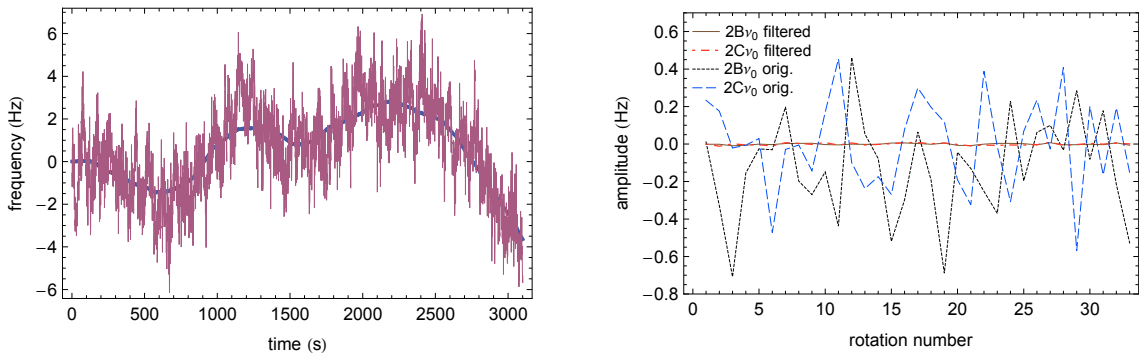

Figure 5.5.: *Effect of the low-pass filter on the raw data (left) and the fitted amplitudes at $2\omega_{rot}$ (right). Dashed: original amplitudes, solid: amplitudes of the low-pass filtered data. The rotation period is 90 s. Modulations on the timescale of a rotation are averaged out.*

The Robertson-Mansouri-Sexl test theory on the other hand models a possible deviation from an isotropic expansion of light via

$$\begin{aligned} 2B(t) &= (1/2-\beta+\delta)(v_{solar}^2/c_0^2)(\gamma_3(t)\cos\omega_\oplus T_\oplus + \gamma_4(t)\cos 2\omega_\oplus T_\oplus \\ &\quad +\sigma_3(t)\sin\omega_\oplus T_\oplus + \sigma_4(t)\sin 2\omega_\oplus T_\oplus) \\ 2C(t) &= (1/2-\beta+\delta)(v_{solar}^2/c_0^2)(\gamma_0(t)+\gamma_1(t)\cos\omega_\oplus T_\oplus + \gamma_2(t)\cos 2\omega_\oplus T_\oplus \\ &\quad +\sigma_1(t)\sin\omega_\oplus T_\oplus + \sigma_2(t)\sin 2\omega_\oplus T_\oplus). \end{aligned} \tag{5.6}$$

At this stage of the evaluation process both models are in principle identical, except the fact, that in the RMS model no constant offset is expected for the amplitudes $2B\nu_0$. However, such an offset is present in the data. To account for this fact we introduce an additional term b_{syst} into the fit function for the amplitudes $2B\nu_0$ to model this systematic offset. Doing so, at this stage of the evaluation the only difference between the two models is the multiplication with a constant factor.

Figures 5.6 and 5.7 show for all the 46 datasets the fitted amplitudes $B_0, ..., C_4$ of the SME model with their statistical errors as time series. As can be seen from the statistics of the single series' (compare table 5.1) they are influenced by small systematic effects. This influence is strongest for the amplitudes B_0 and C_0, which are determined via offsets in the series of the active rotation amplitudes. For all the series' the standard deviation of the series is about a factor of two bigger than the average statistical error of the single datapoints.

coefficient	weighted mean	mean of stat. errors $\bar{\sigma}_i$	st. dev. of series σ_{series}
B_0	$(18.1 \pm 2.0) \cdot 10^{-18}$	$1.6 \cdot 10^{-17}$	$4.2 \cdot 10^{-17}$
B_1	$(3.4 \pm 2.8) \cdot 10^{-18}$	$2.2 \cdot 10^{-17}$	$5.2 \cdot 10^{-17}$
B_2	$(3.0 \pm 2.8) \cdot 10^{-18}$	$2.2 \cdot 10^{-17}$	$4.5 \cdot 10^{-17}$
B_3	$(-5.0 \pm 2.8) \cdot 10^{-18}$	$2.2 \cdot 10^{-17}$	$5.5 \cdot 10^{-17}$
B_4	$(-2.8 \pm 2.8) \cdot 10^{-18}$	$2.2 \cdot 10^{-17}$	$4.4 \cdot 10^{-17}$
C_0	$(2.2 \pm 1.6) \cdot 10^{-18}$	$1.3 \cdot 10^{-17}$	$3.5 \cdot 10^{-17}$
C_1	$(1.6 \pm 2.3) \cdot 10^{-18}$	$1.8 \cdot 10^{-17}$	$3.2 \cdot 10^{-17}$
C_2	$(3.1 \pm 2.3) \cdot 10^{-18}$	$1.8 \cdot 10^{-17}$	$3.3 \cdot 10^{-17}$
C_3	$(2.1 \pm 2.3) \cdot 10^{-18}$	$1.8 \cdot 10^{-17}$	$3.9 \cdot 10^{-17}$
C_4	$(-0.3 \pm 2.3) \cdot 10^{-18}$	$1.8 \cdot 10^{-17}$	$2.8 \cdot 10^{-17}$

Table 5.1.: *Statistics of the time series' of the modulation amplitudes B_i, C_i for the 46 datasets used for evaluation after decorrelation of the tilt.*

5.3. Analysis in the Robertson-Mansouri-Sexl-Framework

As has already been mentioned above the time series for the sidereal modulations are eventually the same for the RMS and the SME theory. A multiplication of the amplitudes $B_0, ..., C_4$ of the SME with the factor

$$(\frac{1}{2} \cdot (v_{solar}^2/c_0^2))^{-1} \approx 1.3 \cdot 10^6$$

would directly yield the different sidereal amplitudes $\gamma_0, ..., \sigma_4$ of the RMS model, where the RMS parameter $(\beta - \delta - 1/2)$ has been immersed into the amplitudes. However, instead of the possibility of this multiplication we directly fitted the amplitudes.

The difference between the two test theories lies in the specific time dependence of the sidereal day coefficients, which vary over the course of a sidereal year. Within the RMS theory they depend on the laboratories velocity with respect to the Cosmic Microwave Background (CMB) and the orientation of the laboratory, respectively the orientation of the direction of light propagation with respect to this velocity vector. Just a single coefficient $(\beta - \delta - 1/2)$ describes a possible anisotropy of the speed of light within this model and determines, together with some geometrical factors as given in appendix B, the time dependence.
To determine the anisotropy coefficient of the RMS-theory we therefore simultaneously fit the given time dependence to all the time series' γ_i, σ_i. This fit yields for the data with the tilt being decorrelated

$$(\beta - \delta - 1/2) = (-1.6 \pm 6.0) \cdot 10^{-12}. \tag{5.7}$$

To check which influence the inclusion of the systematic offset b_{syst} into the fitting procedure has on the final result we repeat the fits without this offset. However, this fit yields

almost exactly the same value.
To estimate the systematic error associated with the measurement is difficult, since the parameter is determined via a combination of an offset of $2C\nu_0$ and via different Fourier amplitudes at sidereal frequencies. The sensitivity coefficients used for the decorrelation of residual tilt modulations exhibit fluctuations of $\approx 15\%$. Thus the decorrelation may introduce a systematic shift of the frequency modulation amplitudes proportional to the amplitudes of the residual tilt modulations, which are rather constant in amplitude. However, the shift differs for different datasets and can be assumed to average out partially for our long time series inversely proportional to the square root of the number of different measurement runs. We estimate the residual effect to be on the order of $\pm 1.3 \cdot 10^{-17}$ for the amplitudes of one dataset, which averages down to $1.9 \cdot 10^{-18}$ for the systematic error on the mean amplitude $2\bar{C}$ if one uses all our measurement runs. If the RMS parameter would be determined only via this offset, as described by the coefficient γ_0, then the systematic error would be given by the systematic error of the offset divided by $\gamma_0 \cdot (v_{solar}^2/c_0^2)$, resulting in an error of $4.9 \cdot 10^{-12}$. However, the RMS parameter is not determined by this offset alone, but as well via eight amplitudes of different sidereal modulations. Thus the influence of the offset shift is strongly reduced.
Alternatively one may compare the given value of $(\beta - \delta - 1/2)$ to the result obtained from an analysis of the dataset without decorrelation of the tilt and the dataset where additionally the drift has been subtracted. Conservatively we add a fraction of these differences and a fraction of the offset error obtaining an overall estimate for the systematic error of $1.2 \cdot 10^{-12}$.
Thus our final result for the Lorentz violation parameter $(\beta - \delta - 1/2)$ of the Robertson-Mansouri-Sexl test theory is

$$\boxed{(\beta - \delta - 1/2) = (-1.6 \pm 6.0 \pm 1.2) \cdot 10^{-12}.} \tag{5.8}$$

This corresponds to an upper limit (1σ) of

$$|\beta - \delta - 1/2|_{1\sigma} \leq |-1.6 - \sqrt{6.0^2 + 1.2^2}| \cdot 10^{-12} = 7.7 \cdot 10^{-12}. \tag{5.9}$$

Within the RMS framework this result yields an upper limit for a possible isotropy violation $\frac{1}{2}|\Delta c(\pi/2)/c|_{1\sigma} = \frac{1}{2} v_{solar}^2/c_0^2 \cdot (\beta - \delta - 1/2)$ (v_{solar} being the velocity of the solar system versus the cosmic microwave background, 370 km/s) of

$$\boxed{\tfrac{1}{2}|\Delta c(\pi/2)/c|_{1\sigma} \leq 6 \cdot 10^{-18},} \tag{5.10}$$

which is more than one order of magnitude tighter than previous results of our group [20] and other groups [21, 37].

coefficient	value (in 10^{-17})	upper limit (2σ, in 10^{-17})
$(\tilde{\kappa}_{e-})^{ZZ}$	$1.6 \pm 2.4 \pm 1.1 \pm 12$	≤ 26.2
$(\tilde{\kappa}_{e-})^{XY}$	$0.0 \pm 1.0 \pm 0.3$	≤ 2.1
$(\tilde{\kappa}_{e-})^{XZ}$	$0.4 \pm 1.5 \pm 0.1$	≤ 3.4
$(\tilde{\kappa}_{e-})^{YZ}$	$-0.6 \pm 1.4 \pm 0.5$	≤ 3.6
$(\tilde{\kappa}_{e-})^{XX} - (\tilde{\kappa}_{e-})^{YY}$	$0.8 \pm 2.0 \pm 0.3$	≤ 4.8
$\beta_{\oplus}(\tilde{\kappa}_{o+})^{XY}$	$1.5 \pm 1.5 \pm 0.2$	≤ 4.5
$\beta_{\oplus}(\tilde{\kappa}_{o+})^{XZ}$	$-0.1 \pm 1.0 \pm 0.2$	≤ 2.1
$\beta_{\oplus}(\tilde{\kappa}_{o+})^{YZ}$	$-0.1 \pm 1.0 \pm 0.4$	≤ 2.3

Table 5.2.: *Values for the different SME coefficients as derived from the shown time series. An upper 2σ-limit for the magnitude of the coefficients using the total uncertainty is given in the right column.*

5.4. Analysis in the Standard Model Extension Frame

Since our data extends over more than one year we are able to determine all of the 8 coefficients of the photonic sector of the SME, which are in principle accessible with cavity-based experiments. For the determination of values for the $\tilde{\kappa}$-matrices we make several assumptions/simplifications, namely:

- The values of the components of the matrices $(\tilde{\kappa}_{o-})$ and $(\tilde{\kappa}_{e+})$, which describe a birefringence of the vacuum, are well below the sensitivity of our current setup, so that they can be treated as being zero. This is supported by astrophysical observations.

- We treat our vacuum ($p \approx 1 \cdot 10^{-7}$ mbar) as being almost perfect and set $\epsilon = 1$.

With these justified simplifications the connection between the modulation of the beat frequency, as given by the timeseries $2B(t_i)$ and $2C(t_i)$, and the components of the $(\tilde{\kappa})$-matrices is given by equation 5.5 with the Fourier amplitudes $B_0, .., C_4$ being modulated at an annual[2] frequency as given in appendix C. All of these functions for the different time series contain different combinations of the components of the $(\tilde{\kappa}_{o+})$ matrix and a component of the $(\tilde{\kappa}_{e-})$ matrix. Thus, similar to the RMS case, we have to simultaneously fit the model to the ten time series of the modulation amplitudes at sidereal frequencies, yielding the coefficients of interest as displayed in table 5.2.

All the coefficients are determined on the order of $1 \cdot 10^{-17}$. The statistical errors (first error bar in table 5.2) of the fitted values are in a range of $1 \cdot 10^{-17}$ for the $\beta_{\oplus}(\tilde{\kappa}_{o+})$-coefficients and $(\tilde{\kappa}_{e-})^{XY}$ to $2.4 \cdot 10^{-17}$ for the coefficient $(\tilde{\kappa}_{e-})^{ZZ}$, which is as well most seriously

[2]The period of the modulation is the sidereal year!

coefficient	$\tilde{\kappa}_{e-}^{ZZ}$	$\tilde{\kappa}_{e-}^{XX-YY}$	$\tilde{\kappa}_{e-}^{XY}$	$\tilde{\kappa}_{e-}^{XZ}$	$\tilde{\kappa}_{e-}^{YZ}$	$\tilde{\kappa}_{o+}^{XY}$	$\tilde{\kappa}_{o+}^{XZ}$	$\tilde{\kappa}_{o+}^{YZ}$
$\tilde{\kappa}_{e-}^{ZZ}$	1							
$\tilde{\kappa}_{e-}^{XX-YY}$	-0.019	1						
$\tilde{\kappa}_{e-}^{XY}$	-0.020	0.000	1					
$\tilde{\kappa}_{e-}^{XZ}$	0.010	0.018	-0.009	1				
$\tilde{\kappa}_{e-}^{YZ}$	0.003	0.001	0.008	0.039	1			
$\beta_{\oplus}\tilde{\kappa}_{o+}^{XY}$	0.043	0.018	-0.035	**0.306**	**0.129**	1		
$\beta_{\oplus}\tilde{\kappa}_{o+}^{XZ}$	0.036	**0.121**	**-0.295**	0.049	-0.023	**0.123**	1	
$\beta_{\oplus}\tilde{\kappa}_{o+}^{YZ}$	-0.080	**0.295**	**0.122**	0.040	0.013	0.009	-0.001	1

Table 5.3.: *Correlation matrix for the fit of the SME coefficients to the complete dataset. As can be seen from the values correlations of up to 30% exist between several of the coefficients. For brevity of display the coefficient combination* $(\tilde{\kappa}_{e-})^{XX} - (\tilde{\kappa}_{e-})^{YY}$ *has been abbreviated as* $(\tilde{\kappa}_{e-})^{XX-YY}$*. Correlations above* 10% *have been highlighted.*

affected by systematical errors. A comparison of the determined values to the total uncertainties shows, that all the coefficients are compatible with zero within the 1σ uncertainty margins. A look into table 5.3 listing the correlations between the fitted coefficients shows, that for some coefficients correlations on a level of up to 30% exist (highlighted in the table).

The systematic errors on the values can be estimated using the sizes of the different effects listed in table 4.2. The biggest influence is to be expected for $(\tilde{\kappa}_{e-})^{ZZ}$, which is dominated by an offset in the amplitudes C^i, since it appears in the Fourier component C_0 and is not determined via an annual/sidereal modulation. Thus errors upon decorrelation of the tilt directly lead to a systematic error, which averages out only if one includes many different datasets in the evaluation. The contribution can be estimated as the effect for one dataset divided by the square root of the total number of different measurement runs. The estimated effect on $2C$ as derived earlier is $1.3 \cdot 10^{-17}$ for a single dataset. With 46 independent measurement runs this averages down to a level of $1.9 \cdot 10^{-18}$ yielding a systematic error on $(\tilde{\kappa}_{e-})^{ZZ} \approx 8C_0/(3sin^2\chi)$ due to the tilt decorrelation of $\approx \pm 6.7 \cdot 10^{-18}$.
As in the case of the analysis in the RMS framework one may compare the obtained values to the results of an evaluation of the data without having the tilt decorrelated and of the data after subtraction of the drift influence. Conservatively we add a part of this difference to the systematic errors, yielding the second error bar in table 5.2.
As has already been mentioned in chapter 4 one systematic effect exists of which the source could not be identified so far, but which is probably of thermal origin. The modulation amplitudes at the frequency of the rotation ω_{rot} exhibit an offset of ≈ 0.5 Hz for one component, respectively ≈ -0.2 Hz for the other (compare chapter 4). Furthermore this offset shows from time to time variations with a period of ≈ 2 hours.
The modulation amplitudes $2C\nu_0$ at twice the frequency of rotation show no significant

offset after decorrelation of the tilt, but the amplitudes $2B\nu_0$ show a small offset of 10 mHz. We can not exclude, that a systematic effect of the same size might be present on the amplitude $2C\nu_0$ as well, possibly masking a finite value of the coefficient $(\tilde{\kappa}_{e-})^{ZZ}$. Although we do not believe this to be the case, we conservatively add the value this offset would yield, $1.2 \cdot 10^{-16}$, as a systematic error to the error bars of $(\tilde{\kappa}_{e-})^{ZZ}$. All other coefficients are determined via combinations of the Fourier amplitudes at a sidereal and annual frequency and are thus widely insensitive to a possible offset on the modulation amplitudes. These are susceptible to modulations of these offsets. This is the case for our varying error due to the tilt decorrelation. However, it is difficult to estimate the systematic effect of these modulations on the fitted value of the coefficients, since these are primarily affected in a systematic way for modulations with a stable phase, which is not the case here. Thus, as already mentioned, we use part of the difference between the values determined with and without tilt decorrelation as an estimate for the systematic error, yielding the values as given in table 5.2.

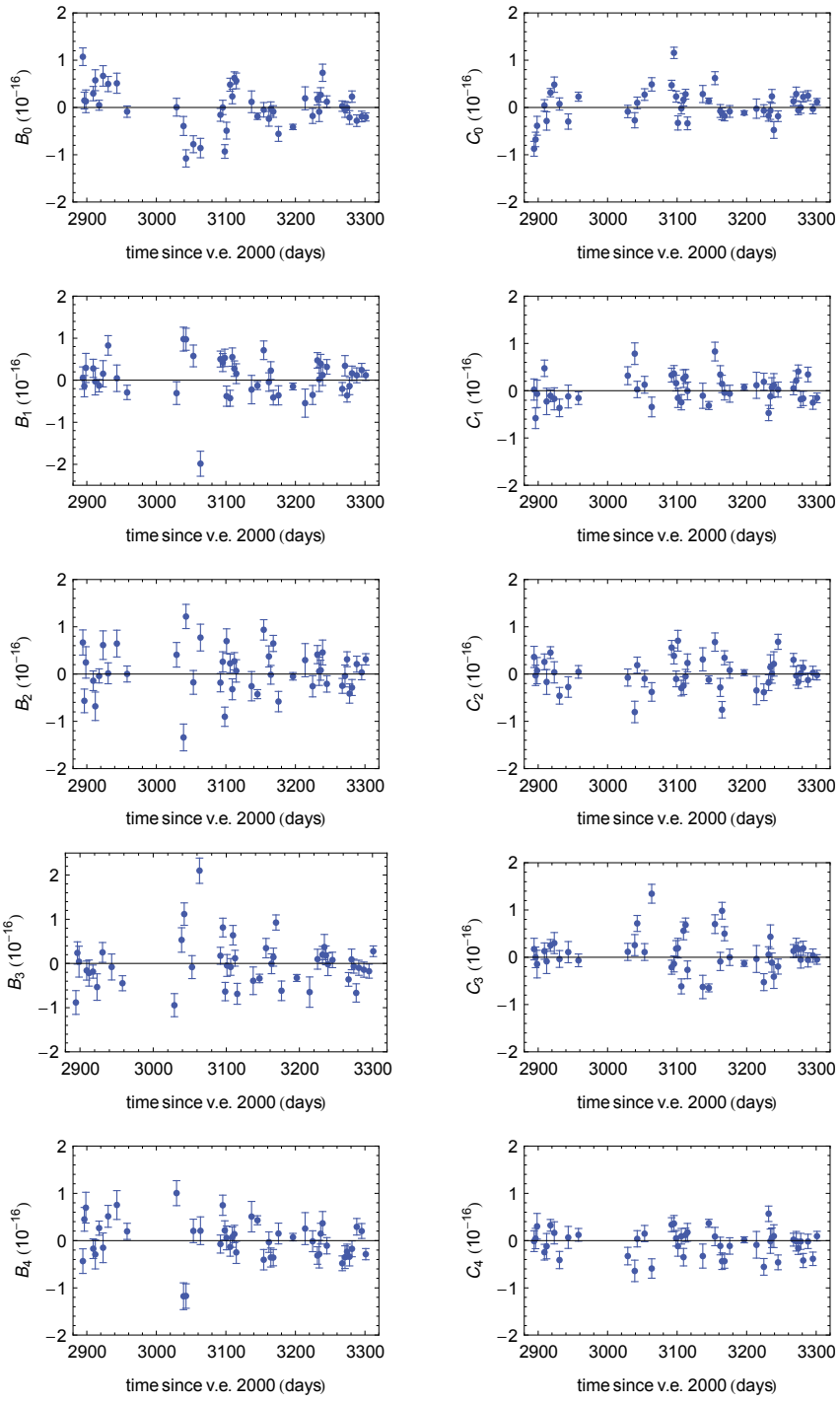

Figure 5.6.: *Overview of the modulation amplitudes B_i, C_i for the undecorrelated data. The values B_0, C_0 are offsets of the modulation amplitudes at twice the active rotation rate, while the others are amplitudes at sidereal frequencies.*

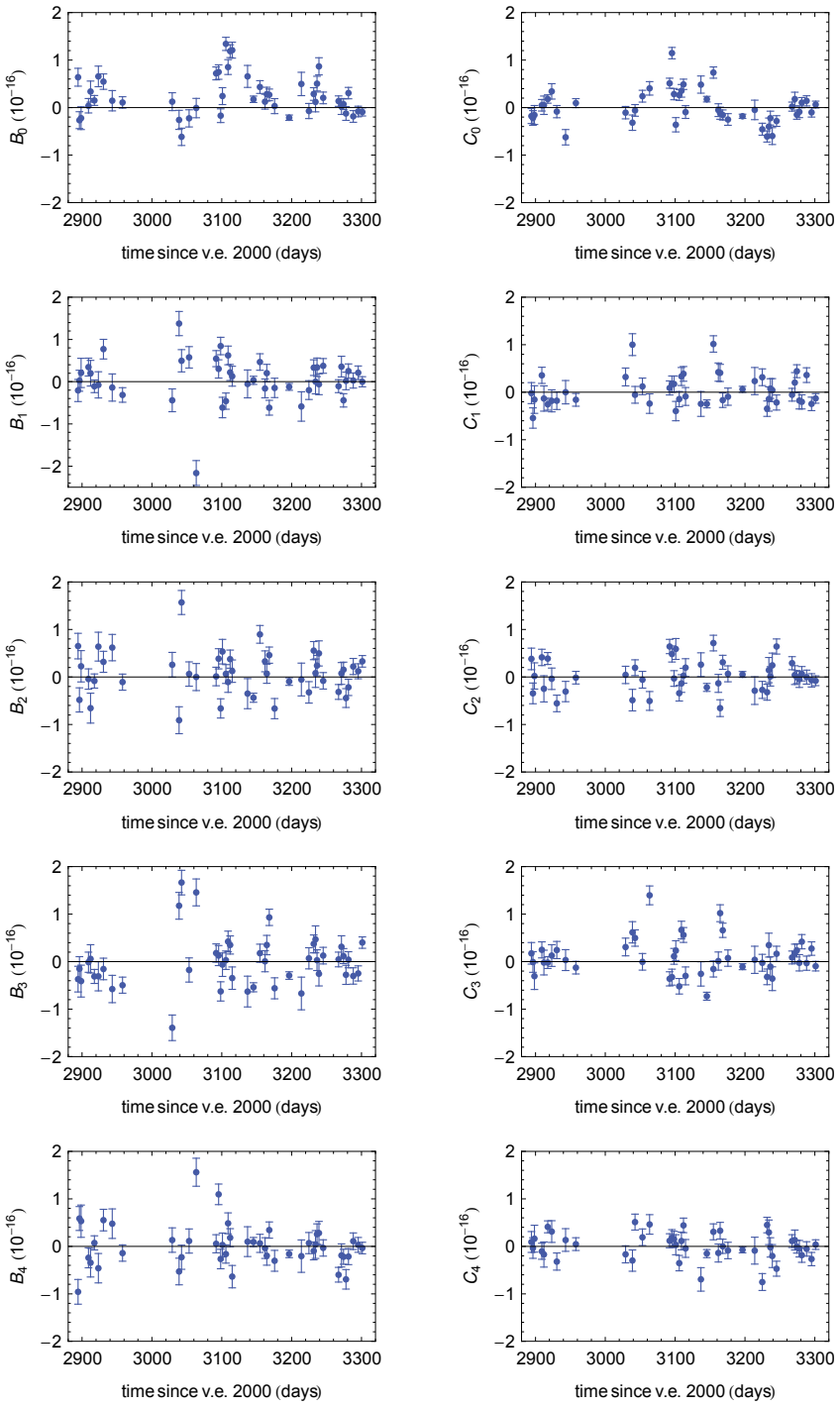

Figure 5.7.: *Overview over the different amplitudes B_i and C_i derived from the 46 datasets after decorrelation of the tilt.*

6. Conclusion and Outlook

During this work a highly sensitive apparatus has been developed for an improved test of the isotropy of space, interpreted in terms of the isotropy of the speed of light. We have collected data during a period of more than a year, thus allowing the determination of the eight coefficients of the Standard Model Extension theory as described in chapter 2, and the determination of the parameter $(\beta - \delta - 1/2)$ of the Robertson-Mansouri-Sexl test theory. The results of this work are consistent with an isotropic speed of light on a level of a few parts in 10^{-17} and no significant indication of a violation of Lorentz invariance has been found for photons.

The limits which could be set on the parameters of the two test theories are for all coefficients more stringent than previously reported results by more than one order of magnitude (see table 6.1 and fig. 6.1). This improvement has been achieved by the use of a monolithic high finesse ULE resonator structure, which allows for common mode rejection and reduces drift effects as compared to resonators made from fused silica. Furthermore the narrow line width as compared to previously used sapphire resonators allows more precise locking of the laser to the resonance frequency of the cavity, while the amount of frequency noise is reduced further by the use of an active vibration isolation.
Another reason for the improvement is the large amount of data comprising ≈ 135000 rotations which could be used for the analysis.

The sensitivity of the experiment is limited by the small residual systematic effects occuring at twice the frequency of rotation. Estimating the potential limit via the single rotation sensitivity, which is approximately 0.4 Hz (width of the histograms of $2B\nu_0, 2C\nu_0$, would yield a potential limit of 0.2 Hz$/\nu_0\sqrt{135000} \approx 2 \cdot 10^{-18}$ for the amplitudes C_0, B_0, corresponding to a potential limit for $(\tilde{\kappa}_{e-})^{ZZ}$ of $1.4 \cdot 10^{-17}$.

Thus, it is evident that for a further improvement of the experiment it is first of all obligatory to find the source of the very small residual systematic effect, which could not be found so far. Furthermore, the experiment should be moved to a location with a better stability of the environmental conditions, as e.g. would be the case in the basement of the university. As test measurements showed, a room in the basement would provide a very stable environment concerning tilt variations as the tilt of the floor varies by few μrad only over the course of several days. This would allow to remove the active stabilization system for the baseplate tilt, which due to its finite stiffness causes the constant residual tilt modulation of $\approx 0.2\mu$rad. In connection with a tilt sensor with higher resolution this might allow

parameter	This work	Herrmann et al. [21]	Stanwix et al. [37]	Müller et al. [74]
$(\tilde{\kappa}_{e-})^{ZZ}$	1.6 ± 12.3	-194 ± 518	143 ± 179	2230 ± 2900
$(\tilde{\kappa}_{e-})^{XX} - (\tilde{\kappa}_{e-})^{YY}$	0.8 ± 2.0	54 ± 48	-5 ± 47	-120 ± 160
$(\tilde{\kappa}_{e-})^{XY}$	0 ± 1.1	-31 ± 25	29 ± 23	77 ± 40
$(\tilde{\kappa}_{e-})^{XZ}$	0.4 ± 1.5	57 ± 49	-69 ± 22	-103 ± 39
$(\tilde{\kappa}_{e-})^{YZ}$	-0.6 ± 1.5	-15 ± 44	21 ± 21	9 ± 42
$(\tilde{\kappa}_{o+})^{XY}$	1.5 ± 1.5	-25 ± 51	-9 ± 26	17 ± 20
$(\tilde{\kappa}_{o+})^{XZ}$	-0.1 ± 1.0	-36 ± 27	-44 ± 25	-31 ± 23
$(\tilde{\kappa}_{o+})^{YZ}$	-0.1 ± 1.1	29 ± 28	-32 ± 23	-28 ± 22
$(\beta - \delta - 1/2)$	-1.6 ± 6.1	-210 ± 190	-94 ± 81	not given

Table 6.1.: *Comparison of the values determined within this work with values published by other groups. The components of the $(\tilde{\kappa}_{e-})$ matrix are in 10^{-17}, of the $(\tilde{\kappa}_{o+})$ matrix in 10^{-13}. The RMS parameter is given in 10^{-12}.*

to control the tilt even more precise than is possible at the moment. Together with the use of resonator geometries, which are by construction/design less susceptible to tilt variations and exhibit smaller tilt sensitivities this would allow to significantly reduce the systematic errors due to tilt modulations, respectively due to not precisely known sensitivities.

Another advantage of the transfer of the experiment to the basement is the increased temperature stability of the room. The test measurements showed, that almost no daily modulation of the ambient temperature exists for rooms deep enough in the basement. Thus, the realization of an extremely high temperature stability for the complete setup would be simplified quite a lot as compared to the present laboratory, which is influenced by the periodic irradiation by sunlight and the change of the ambient temperature.
The higher stability of the temperature of the experiment will as well allow for a stronger suppression of the drifts of the beat frequency, which on this level may already lead to serious systematic effects. For this purpose a new vacuum chamber has already been constructed, which allows for better control of the resonator temperature and should allow to strongly reduce residual drifts. Another advantageous feature of the new vacuum chamber is the possibility to use both of our resonator blocks for our measurements. So far only one block has been used. Thus, the amount of data could be increased by a factor of two.

However, for a strong improvement of the current values it would be as well necessary to considerably reduce the frequency noise. One possible measure is to implement vibration insensitive mounts for the resonators, which have already been described in literature (e.g. [73]). Ideally these would lead to smaller tilt sensitivities of the resonance frequencies as well. FEM simulations aiming in this direction are performed and should allow finding the optimum support system and suitable resonator geometries. Since our experiment is already equipped with an active vibration isolation system though, these measures alone will not

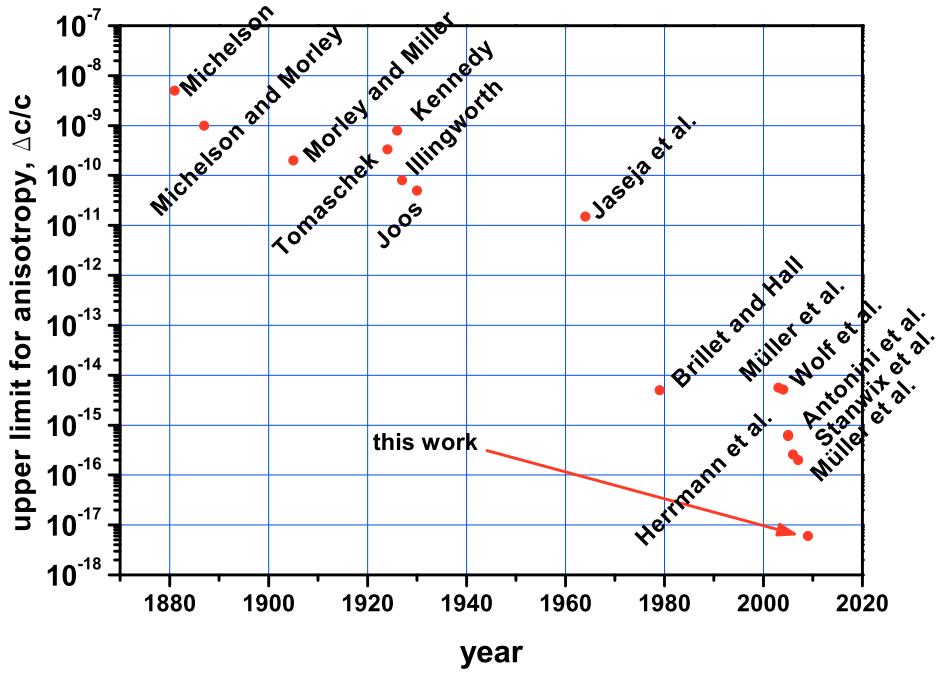

Figure 6.1.: *Improvement on the upper limit for a possible anisotropy of the speed of light over the course of time as derived from the RMS parameter.*

improve the frequency stability too much.
For a considerable reduction of frequency noise it is necessary to reduce the amount of thermal noise of the resonators, which means the construction of new resonators. The thermal noise can be reduced in two possible ways. One solution is to increase the spot size of the laser beams on the cavity mirrors. This means the use of longer resonator structures, which are in turn potentially more sensitive to tilt variations and vibrations. However, as mentioned above the use of FEM simulations might provide geometries with reduced sensitivities to tilts and vibrations. The other option is to return to cryogenic resonator structures, which inherently exhibit a lower thermal noise than resonators at room temperature. However, for this option to be realized it would be necessary to develop a cryogenic setup which is free of technical noise disturbing the measurement process.

A. Description of Frequency Stability

In the presented thesis a measure for the frequency stabiliy of oscillators in the time domain is used, the Allan deviation (or root Allan variance, RAV). A short introduction to measures of frequency stability, their definitions and connections to measures in the frequency domain will be given. For a detailled decsription of the subjet consult [75] or [76].
One wants to measure the frequency of the output of a frequency source (e.g. a quartz oscillator or the output signal of an optical clock), which can be described by

$$V(t) = [V_0 + \epsilon(t)] \cdot sin\left(2\pi\nu_0 t + \phi(t)\right), \tag{A.1}$$

where V_0 is the nominal peak output voltage, $\epsilon(t)$ is the amplitude deviation, ν_0 is the nominal frequency of the source and $\phi(t)$ is the phase deviation. The frequency of $V(t)$ is measured as a function of time, i.e. one has a time series of frequency data y_i, where every point has been taken with a gating time of τ_0 and a zero dead time between adjacent measurements is assumed. From this frequency measurement one wants to deduce information about the stability of the nominal frequency ν_0 of the oscillator. The fractional frequency deviation $y(t)$ is given by

$$y(t) = \frac{\nu(t) - \nu_0}{\nu_0} = \frac{1}{2\pi\nu_0}\frac{d\phi}{dt}. \tag{A.2}$$

The instability of most frequency sources can be modeled by a combination of different noise types (see A.1) having spectral densities of a power law form $S_y(f) \propto f^\alpha$, where f is the Fourier frequency of the noise component. Therefore one can write

$$S_y(f) = \sum_{\alpha=-2}^{\alpha=+2} h_\alpha f^\alpha. \tag{A.3}$$

Most often one wants to describe the instability not in the frequency domain using the noise spectral density, but in the time domain.
A first possibility would be just to calculate the classical variance of the dataset. As has been shown this is not useful [77], since only for the case of white noise ($\alpha = 0$, uncorrelated random noise) it is a stable measure. For other noise types it may depend on the length of the dataset and may be divergent (e.g. for flicker noise, $\alpha = -1$).
Instead one should use a K-sample variance (K$\in \mathbb{N}$) as a general measure for the frequency stability. The most general definition is given by

$$\sigma_y^2(K, m \cdot \tau_0) = \frac{1}{K-1}\sum_{k=1}^{K}\left(\bar{y}_k - \frac{1}{K}\sum_{j=1}^{K}\bar{y}_j\right)^2, \tag{A.4}$$

noise type	α	$S_y(f)$	$\sigma_y^2(\tau)$
white phase modulation	2	$h_2 f^2$	$\frac{3f_h h_2}{4\pi^2} \cdot \frac{1}{\tau^2}$
flicker phase modulation	1	$h_1 f$	$\frac{1.038+3\ln(2\pi f_h \tau)}{4\pi^2} \cdot \frac{1}{\tau^2}$
white frequency modulation	0	h_0	$\frac{1}{2} h_0 \cdot \frac{1}{\tau}$
flicker frequency modulation	-1	$h_{-1} f^{-1}$	$2\ln(2) h_{-1}$
random walk frequency modulation	-2	$h_{-2} f^{-2}$	$\frac{4\pi^2}{6} h_{-2} \tau$

Table A.1.: *Different commonly encountered noise types and the connection between the power law models and the Allan variance. f_h is an upper cutoff frequency given by the bandwidth of the measurement system.*

where the $\bar{y}_k$ are $\bar{y}_k = \frac{1}{m} \sum_{l=k\cdot m}^{(k+1)\cdot m-1} y_l$. So the original time series y_i is divided into intervals extending over a time $\tau = m \cdot \tau_0$ each and for every interval the average value is calculated yielding the $\bar{y}_k$.
Most commonly used and recommended by IEEE [78] is the so called **Allan variance**, which is an averaged 2-sample variance defined by

$$\sigma_y^2(\tau) = \frac{1}{2} \left\langle (\Delta y)^2 \right\rangle, \tag{A.5}$$

where the brackets denote an infinite time average and the Δ denotes a first finite difference of adjacent frequency measurements taken with a sampling time of τ. In practice for a discrete finite time series y_i it can be estimated by

$$\sigma_y^2(\tau_0) = \frac{1}{2(N-1)} \sum_{i=1}^{N-1} (y_{i+1} - y_i)^2, \tag{A.6}$$

where τ_0 is the sampling time for the frequency measurements. To calculate the dependance of $\sigma_y^2(\tau_0)$ on τ one can easily average as many adjacent values y_i as desired to get

$$\sigma_y^2(m\tau_0) = \frac{1}{2m^2(L-1)} \sum_{i=1}^{L} \left(\sum_{j=(i+1)\cdot m}^{(i+2)\cdot m-1} y_j - \sum_{j=i\cdot m}^{(i+1)\cdot m-1} y_j \right)^2, \tag{A.7}$$

where m is the number of measurements averaged for each new datapoint and $L \in \mathbb{N}$ is the biggest number fulfilling $(L+1)m < N$. This is the original 2-sample variance or Allan variance. It can be linked to the power law model of the spectral noise density using the transformation given in [79]:

$$\sigma_y^2(\tau) = 2 \int_0^\infty S_y(f) \frac{\sin^4(\pi\tau f)}{(\pi\tau f)^2} df. \tag{A.8}$$

Clearly this expression is divergent for some of the noise types in A.1.
However it is possible to get more information from the data using a different version of the Allan-Variance, the so called overlapping Allan variance, which is calculated according to

$$\sigma_y^2(\tau) = \frac{1}{2(N-2n+1)} \sum_{i=1}^{N-2n+1} \frac{1}{n} \cdot \left(\sum_{j=i+n}^{i+2n-1} y_j - \sum_{l=i}^{i+2n-1} y_l \right)^2 . \tag{A.9}$$

This version increases confidence for the calculated values due to higher numbers of datapoints for averaging, and it allows the overlapping Allan variance to be calculated for longer averaging times τ than is possible for the ordinary Allan variance.
Another measure for the frequency stability (or instability) of a frequency source is the so called **Hadamard variance**, a 3-sample variance defined by

$$H\sigma_y^2(\tau_0) = \frac{1}{6(N-1)} \sum_{k=1}^{N-2} (y_{k+2} - 2y_{k+1} + y_k)^2. \tag{A.10}$$

In the same way as for the Allan variance one can derive an equation to calculate the overlapping Hadamard variance for integration times $\tau = m \cdot \tau_0$

$$H\sigma_y^2(m\tau_0) = \frac{1}{6m^2(N-3m+1)} \sum_{j=1}^{N-3m+1} \left(\sum_{i=j}^{j+m-1} [y_{i+2m} - 2y_{i+m} + y_i] \right)^2 \tag{A.11}$$

One advantage of the Hadamard variance is the fact, that linear frequency drift does not affect the calculated value. Furthermore the Hadamard variance is still convergent for some noise types, for which the Allan variance is divergent.
Of course a lot of other measures for frequency stability exist with special fields of applications. For an overview see e.g. [80]

B. Full Expressions of the RMS Theory

For our analysis we neglected terms arising due to the modulation of the laboratories velocity relative to the cosmic microwave background. This is justifiable, since these terms are suppressed strongly in comparison to the terms containing only the velocity v_{solar} of the solar system relative to the CMB[1]. For completeness we derive in the following the full expressions for the modulation of the velocity by the orbital motion. However, we still neglect the modulation of the velocity due to the rotation of the earth and just consider the changing orientation of the resonators due to the rotation. The nomenclature is the same as in 2.3.3.

The velocities contributing to the velocity of the laboratory versus the cosmic microwave background (CMB) are the speed of the solar system versus the CMB [31]

$$\vec{v}_{solar} = v_{solar} \cdot \begin{pmatrix} \cos\Phi\cos\Theta \\ \sin\Phi\cos\Theta \\ -\sin\Theta \end{pmatrix}, \tag{B.1}$$

where the right ascension Φ and the declination Θ specify the direction within the sun centered equatorial frame, and the velocity of the earth (orbital motion), which is given by

$$\vec{v}_{orb} = v_{orb} \cdot \begin{pmatrix} \sin\Omega T \\ -\cos\Omega T\cos\eta \\ -\cos\Omega T\sin\eta \end{pmatrix} \tag{B.2}$$

within the SCCEF. The orientation of the two resonators in the laboratory frame is given by

$$\hat{e}_{1,lab}(t) = \begin{pmatrix} \cos\omega_{rot}t \\ \sin\omega_{rot}t \\ 0 \end{pmatrix}, \qquad \hat{e}_{2,lab}(t) = \begin{pmatrix} \sin\omega_{rot}t \\ -\cos\omega_{rot}t \\ 0 \end{pmatrix}. \tag{B.3}$$

Then in the SCCEF the orientation of the resonators is given by

$$\hat{e}_1(t) = \begin{pmatrix} \cos\chi\cos\omega_{\oplus}T_{\oplus}\cos\omega_{rot}t - \sin\omega_{\oplus}T_{\oplus}\sin\omega_{rot}t \\ \cos\chi\sin\omega_{\oplus}T_{\oplus}\cos\omega_{rot}t + \cos\omega_{\oplus}T_{\oplus}\sin\omega_{rot}t \\ -\sin\chi\cos\omega_{rot}t \end{pmatrix} \tag{B.4}$$

[1] The biggest term arising is a mixed term containing $v_{solar}\cdot v_{orb} = 0.08\cdot v_{solar}^2$

and

$$\hat{e}_2(t) = \begin{pmatrix} \cos\chi\cos\omega_\oplus T_\oplus \sin\omega_{rot}t + \sin\omega_\oplus T_\oplus \cos\omega_{rot}t \\ \cos\chi\sin\omega_\oplus T_\oplus \sin\omega_{rot}t - \cos\omega_\oplus T_\oplus \cos\omega_{rot}t \\ -\sin\chi\sin\omega_{rot}t \end{pmatrix}. \tag{B.5}$$

The relative shift of the resonance frequency is given by

$$\begin{aligned} \frac{\Delta\nu_1 - \Delta\nu_2}{\nu_0} &= -(\beta - \delta - 1/2)\frac{v^2}{c^2}[\sin^2\theta_1(t) - \sin^2\theta_2(t)] \\ &= -(\beta - \delta - 1/2)\cdot[|\vec{v}\times\hat{e}_1|^2 - |\vec{v}\times\hat{e}_2|^2]/c^2 \end{aligned} \tag{B.6}$$

Evaluation of this formula yields several terms which can be arranged according to

$$\frac{\Delta(\nu_1 - \nu_2)}{\nu} = 2B(t)\sin 2\theta(t) + 2C(t)\cos 2\theta(t)$$

with

$$\begin{aligned} 2B(t) &= (1/2 - \beta + \delta)(v_{solar}^2/c_0^2)(\gamma_3\cos\omega_\oplus T_\oplus + \gamma_4\cos 2\omega_\oplus T_\oplus + \sigma_3\sin\omega_\oplus T_\oplus \\ &\quad +\sigma_4\sin 2\omega_\oplus T_\oplus) \end{aligned}$$

$$\begin{aligned} 2C(t) &= (1/2 - \beta + \delta)(v_{solar}^2/c_0^2)(\gamma_0 + \gamma_1\cos\omega_\oplus T_\oplus + \gamma_2\cos 2\omega_\oplus T_\oplus \\ &\quad +\sigma_1\sin\omega_\oplus T_\oplus + \sigma_2\sin 2\omega_\oplus T_\oplus). \end{aligned}$$

Then the γ_i and σ_i coefficients are given by

$$\begin{aligned} \gamma_0 &= \frac{1}{4}\sin^2\chi(3\cos 2\Theta - 1) + \frac{v_{orb}}{v_{solar}}\cdot(\cos\Phi\cos\Theta\sin^2\chi\sin\Omega T - \\ &\quad [2\sin\Theta\sin\eta + \cos\Theta\cos\eta\sin\Phi]\sin^2\chi\cos\Omega T) \\ \gamma_1 &= -\frac{1}{2}\cos\Phi\sin 2\Theta\sin 2\chi + \frac{v_{orb}}{v_{solar}}\cdot(-\sin 2\chi\cos\Phi\cos\Theta\sin\eta\cos\Omega T \\ &\quad -\sin 2\chi\sin\Theta\sin\Omega T) + O(\frac{v_{orb}^2}{v_{solar}^2}) \end{aligned}$$

$$
\begin{aligned}
\gamma_2 &= -\frac{1}{2}\cos 2\Phi \cos^2\Theta(1+\cos^2\chi) - \frac{v_{orb}}{v_{solar}}\cdot(1+\cos^2\chi)\cdot[\cos\Theta\cos\eta\sin\Phi\cos\Omega T \\
&\quad + \cos\Phi\cos\Theta\sin\Omega T] + O(\frac{v_{orb}^2}{v_{solar}^2}) \\
\gamma_3 &= -\sin\Phi\sin\chi\sin 2\Theta + \frac{v_{orb}}{v_{solar}}\cdot(2\cos\eta\cos\Omega T\sin\Theta\sin\chi \\
&\quad -2\cos\Theta\cos\Omega T\sin\Phi\sin\chi\sin\eta) + O(\frac{v_{orb}^2}{v_{solar}^2}) \\
\gamma_4 &= -\sin 2\Phi\cos\chi\cos^2\Theta + \frac{v_{orb}}{v_{solar}}\cdot(2\cos\Phi\cos\Theta\cos\chi\cos\eta\cos\Omega T \\
&\quad -2\cos\Theta\cos\chi\sin\Phi\sin\Omega T) + O(\frac{v_{orb}^2}{v_{solar}^2})
\end{aligned}
$$

$$
\begin{aligned}
\sigma_1 &= -\frac{1}{2}\sin\Phi\sin 2\chi\sin 2\Theta + \frac{v_{orb}}{v_{solar}}\cdot(\sin 2\chi\cos\eta\sin\Theta\cos\Omega T \\
&\quad -\sin 2\chi\cos\Theta\sin\Phi\sin\eta\cos\Omega T) + O(\frac{v_{orb}^2}{v_{solar}^2}) \\
\sigma_2 &= -\frac{1}{2}\cdot(1+\cos^2\chi)\sin 2\Phi\cos^2\Theta + \frac{v_{orb}}{v_{solar}}(1+\cos^2\chi)\cdot(\cos\Phi\cos\eta\cos\Theta\cos\Omega T \\
&\quad -\cos\Theta\sin\Phi\sin\Omega T) \\
\sigma_3 &= \cos\Phi\sin 2\Theta\sin\chi + \frac{v_{orb}}{v_{solar}}\cdot(2\cos\Phi\cos\Theta\sin\eta\sin\chi\cos\Omega T \\
&\quad +2\sin\Theta\sin\chi\sin\Omega T) + O(\frac{v_{orb}^2}{v_{solar}^2}) \\
\sigma_4 &= \cos 2\Phi\cos^2\Theta\cos\chi + \frac{v_{orb}}{v_{solar}}\cdot(2\cos\Theta\cos\eta\cos\chi\sin\Phi\cos\Omega T \\
&\quad +2\cos\Phi\cos\Theta\cos\chi\sin\Omega T) + O(\frac{v_{orb}^2}{v_{solar}^2})
\end{aligned}
$$

C. SME Coefficients and Laboratory Frame Coefficients

As has been mentioned in chapter 2, we assume that the matrices $(\tilde{\kappa}_{o-})$ and $(\tilde{\kappa}_{e+})$ describing a possible birefringence of the vacuum are negligible compared to the sensitivity of our apparatus, which is supported by astrophysical observations. Thus they are considered to be zero. Furthermore we set $\epsilon = 1$, since we are working with vacuum conditions. Then the connection between the parameters of the SME and the modulation amplitudes measured in the laboratory is to first order in orbital boosts given by [50]

$$B_0 = -\frac{1}{2}\beta_L \sin\chi(\tilde{\kappa}_{o+})^{XY} \tag{C.1}$$

$$B_1 = \frac{1}{2}\sin\chi(\tilde{\kappa}_{e-})^{XZ} + \frac{1}{2}\beta_\oplus \sin\chi\Big[\sin\Omega_\oplus T(\tilde{\kappa}_{o+})^{XY} - \sin\eta\cos\Omega_\oplus T(\tilde{\kappa}_{o+})^{YZ}\Big] - \frac{1}{2}\beta_L\cos\chi(\tilde{\kappa}_{o+})^{XZ} \tag{C.2}$$

$$B_2 = -\frac{1}{2}\sin\chi(\tilde{\kappa}_{e-})^{YZ} - \frac{1}{2}\beta_\oplus \sin\chi\Big[-\cos\eta\cos\Omega_\oplus T(\tilde{\kappa}_{o+})^{XY} + \sin\eta\cos\Omega_\oplus T(\tilde{\kappa}_{o+})^{XZ}\Big] + \frac{1}{2}\beta_L\cos\chi(\tilde{\kappa}_{o+})^{YZ} \tag{C.3}$$

$$B_3 = -\frac{1}{4}\cos\chi\Big[(\tilde{\kappa}_{e-})^{XX} - (\tilde{\kappa}_{e-})^{YY}\Big] - \frac{1}{2}\beta_\oplus\cos\chi\Big[\sin\Omega_\oplus T(\tilde{\kappa}_{o+})^{YZ} - \cos\eta\cos\Omega_\oplus T(\tilde{\kappa}_{o+})^{XZ}\Big] \tag{C.4}$$

$$B_4 = \frac{1}{2}\cos\chi(\tilde{\kappa}_{e-})^{XY} - \frac{1}{2}\beta_\oplus\cos\chi\Big[\sin\Omega_\oplus T(\tilde{\kappa}_{o+})^{XZ} + \cos\eta\cos\Omega_\oplus T(\tilde{\kappa}_{o+})^{YZ}\Big] \tag{C.5}$$

$$C_0 = \frac{3}{8}\sin^2\chi(\tilde{\kappa}_{e-})^{ZZ} - \frac{1}{4}\beta_\oplus \sin^2\chi\Big[\sin\Omega_\oplus T(\tilde{\kappa}_{o+})^{YZ} + \cos\eta\cos\Omega_\oplus T(\tilde{\kappa}_{o+})^{XZ} + 2\sin\eta\cos\Omega_\oplus T(\tilde{\kappa}_{o+})^{XY}\Big] \tag{C.6}$$

$$C_1 = -\frac{1}{2}\sin\chi\cos\chi(\tilde{\kappa}_{e-})^{YZ} + \frac{1}{2}\beta_\oplus \sin\chi\cos\chi\Big[\cos\eta\cos\Omega_\oplus T(\tilde{\kappa}_{o+})^{XY} - \sin\eta\cos\Omega_\oplus T(\tilde{\kappa}_{o+})^{XZ}\Big] + \frac{1}{2}\cos(\tilde{\kappa}_{o+})^{YZ} \tag{C.7}$$

$$C_2 = -\frac{1}{2}\sin\chi\cos\chi(\tilde{\kappa}_{e-})^{XZ} - \frac{1}{2}\beta_\oplus \sin\chi\cos\chi\Big[\sin\Omega_\oplus T(\tilde{\kappa}_{o+})^{XY} - \sin\eta\cos\Omega_\oplus T(\tilde{\kappa}_{o+})^{YZ}\Big] + \frac{1}{2}(\tilde{\kappa}_{o+})^{XZ}$$

$$C_3 = \frac{1}{4}\left(1+\cos^2\chi\right)(\tilde{\kappa}_{e-})^{XY} - \frac{1}{4}\beta_\oplus\left(1+\cos^2\chi\right)\Big[\sin\Omega_\oplus T(\tilde{\kappa}_{o+})^{XZ} + \cos\eta\cos\Omega_\oplus T(\tilde{\kappa}_{o+})^{YZ}\Big] \tag{C.8}$$

$$C_4 = \frac{1}{8}\left(1+\cos^2\chi\right)\Big[(\tilde{\kappa}_{e-})^{XX} - (\tilde{\kappa}_{e-})^{YY}\Big] + \frac{1}{4}\beta_\oplus\left(1+\cos^2\chi\right)\Big[\sin\Omega_\oplus T(\tilde{\kappa}_{o+})^{YZ} - \cos\eta\cos\Omega_\oplus T(\tilde{\kappa}_{o+})^{XZ}\Big]. \tag{C.9}$$

Here we neglected terms of first order in the velocity of the laboratory β_L, since these are strongly suppressed (factor 15) compared to the terms of first order in $\beta_\oplus$.

Acknowledgements

"Begegnet uns jemand, der uns Dank schuldig ist, gleich fällt es uns ein.
Wie oft können wir jemand begegnen, dem wir Dank schuldig sind, ohne daran zu denken."
(Johann Wolfgang von Goethe)

Looking back over the time that has passed since the start of my research activity on this experiment many people and organisations come to my mind whom I have to thank.
Many thanks I owe to Prof. S. Schiller, who as my supervisor gave me the opportunity to work in this interesting and challenging field of fundamental physics. I am as well very thankful that he encouraged me to apply for a stipend, though I thought I would never have a chance to really obtain a fellowship, and for the support during the application to the Lindau Nobel meetings. Many thanks for all I learned from you.
Special thanks go to the Düsseldorf Entrepreneurs Foundation (Gründerstiftung), which granted a fellowship and financed a stipend for two years. I am very thankful for this financial support. Especially that members of the board of the foundation made it possible for me to participate in the Lindau Nobel Laureate meeting 2008 was a great honour. Here I want to thank specifically Prof. J. Uhlenbusch for making this possible. Thanks as well to the Wilhelm-und-Else-Heraeus foundation, which granted financial support for the participation and a fellowship.
Very thankful I am as well to Dr. Alexander Nevsky and Dr. Maxim Okhapkin, who contributed a lot of work during the time of the hardware development, especially with the servo system for the laser locks. From them I learned most of what I know about servo electronics and lasers. Forever I will keep in mind the nice Russian evenings, hopefully these will be repeated sooner or later and we don't lose contact. Болышое спасибо, Товарищи!
Gracie mille a dottore Piergiorgio Antonini, who helped me during the starting months and became a good friend. From him I got a first glance of the measurement system and the problems associated with the measurements. Life in Düsseldorf became a lot poorer after you left. I hope we'll stay in touch.
Very thankful I am as well to Ulf Bressel, who joined the institute shortly after me. Unforgotten are the evenings at dancing courses, but especially the friday evenings at badminton, where we could recover from frustrations of the week. Never forget about the Feuerzangenbowle when planing Xmas partys in future!

Thanks go as well to Claudia. You brought me back to life.
A lot of thanks go to all other members of the institute, who helped me one or the other time with development of equipment or who were eager to discuss different scientific or non-scientific topics.
Thanks as well to the workshops of the university, which were always eager to fulfill my demands and pushed up my order to the top of the waiting list when everything had to be done quick, and to the administration of the university.

Finally I want to thank all the members of my family, who always supported me.

Bibliography

[1] Albert Einstein. Zur Elektrodynamik bewegter Körper. *Annalen der Physik*, 17:891, 1905.

[2] A.A. Michelson and E.W. Morley. On the relative motion of the Earth and the luminiferous ether. *American Journal of Science*, III-34(203):333, Nov 1887.

[3] A. Einstein and A.D. Fokker. *Annalen der Physik*, 44:321, 1914.

[4] H.A. Lorentz. Electromagnetic phenomena in a system moving with any velocity smaller than that of light. *Proc. Amsterdam Acad.*, 6:809, 1904.

[5] H. Poincaré. L'état actuel et l'avenir de la physique mathématique. *Bull. Sci. Math.*, 28:302, 1904.

[6] Michio Kaku. *Strings, conformal fields and M-theory*. Springer, 1999.

[7] H. Nicolai, K. Peeters, and M. Zamaklar. Loop quantum gravity: an outside view. *Classical and Quantum Gravity*, 22(19):R193–R247, 2005.

[8] V.A. Kostelecký and S. Samuel. Spontaneous breaking of Lorentz symmetry in string theory. *Phys. Rev. D*, 39(2):683–685, Jan 1989.

[9] H.P. Robertson. Postulate versus Observation in the Special Theory of Relativity. *Rev. Mod. Phys.*, 21(3):378–382, Jul 1949.

[10] H.E. Ives and G.R. Stilwell. An experimental study of the rate of a moving atomic clock. *J. Opt. Soc. Am.*, 28:215–226, 1938.

[11] H.E. Ives and G.R. Stilwell. An experimental study of the rate of a moving atomic clock ii. *J. Opt. Soc. Am.*, 31:369, 1941.

[12] G. Saathoff, S. Karpuk, U. Eisenbarth, G. Huber, S. Krohn, R. Muñoz Horta, S. Reinhardt, D. Schwalm, A. Wolf, and G. Gwinner. Improved Test of Time Dilation in Special Relativity. *Phys. Rev. Lett.*, 91(19):190403, Nov 2003.

[13] S. Reinhardt et al. Test of relativistic time dilation with fast optical atomic clocks at different velocities. *Nature Physics*, 3, 2007.

[14] R.J. Kennedy and E.M. Thorndike. Experimental establishment of the relativity of time. *Phys. Rev.*, 42:400, 1932.

[15] C. Braxmaier, H. Müller, O. Pradl, J. Mlynek, A. Peters, and S. Schiller. Tests of Relativity Using a Cryogenic Optical Resonator. *Phys. Rev. Lett.*, 88(1):010401, Dec 2001.

[16] C. Lämmerzahl, H. Dittus, A. Peters, and S. Schiller. OPTIS: a satellite based test of special and general relativity. *Class. Quant. Grav.*, 18:2499, 2001.

[17] T.S. Jaseja, A. Javan, J. Murray, and C.H. Townes. Test of Special Relativity or of the Isotropy of Space by Use of Infrared Masers. *Phys. Rev.*, 133(5A):A1221–A1225, Mar 1964.

[18] A. Brillet and J. L. Hall. Improved Laser Test of the Isotropy of Space. *Phys. Rev. Lett.*, 42(9):549–552, Feb 1979.

[19] H. Müller, S. Herrmann, C. Braxmaier, S. Schiller, and A. Peters. Modern Michelson-Morley experiment using cryogenic optical resonators. *Phys. Rev. Lett.*, 91:020401, 2003.

[20] Piergiorgio Antonini. *Test of Lorentz Invariance Using Sapphire Optical Resonators*. PhD thesis, Heinrich-Heine-Universität, Düsseldorf, 2005.

[21] S. Herrmann, A. Senger, E. Kovalchuk, H. Müller, and A. Peters. Test of the Isotropy of the Speed of Light Using a Continuously Rotating Optical Resonator. *Phys. Rev. Lett.*, 95(15):150401, Oct 2005.

[22] Jürgen Ehlers and Claus Lämmerzahl, editors. *Special Relativity: Will it Survive the Next 101 Years?*, volume 702 of *Lecture Notes in Physics*. Springer, 2006.

[23] R. Mansouri and R.U. Sexl. A Test Theory of Special Relativity: i. Simultaneity and Clock Synchronization. *Gen. Rel. Grav.*, 8(7):497, 1977.

[24] M.D. Gabriel and M.P. Haugan. Testing the Einstein equivalence principle: Atomic clocks and local Lorentz invariance. *Phys. Rev. D*, 41(10):2943–2955, May 1990.

[25] M. Haugan and C.M. Will. Modern tests of special relativity. *Physics today*, May:69, 1987.

[26] D. Colladay and V.A. Kostelecký. Lorentz-violating extension of the standard model. *Phys. Rev. D*, 58(11):116002, Oct 1998.

[27] C.M. Will. *Theory and Experiment in Gravitational Physics (Revised Edition)*. Cambridge University Press, 1993.

[28] A.P. Lightman and D.L. Lee. Restricted Proof that the Weak Equivalence Principle Implies the Einstein Equivalence Principle. *Phys. Rev. D*, 8(2):364–376, Jul 1973.

[29] C. Lämmerzahl, A. Macías, and H. Müller. Lorentz invariance violation and charge (non)conservation: A general theoretical frame for extensions of the Maxwell equations. *Phys. Rev. D*, 71(2):025007, Jan 2005.

[30] David Mattingly. Modern Tests of Lorentz Invariance. *Living Reviews in Relativity*, 8(5), 2005.

[31] C.H. Lineweaver et al. The dipole observed in the *COBE*dmr 4 year data. *Astroph. J.*, 470:38, 1996.

[32] R. Mansouri and R.U. Sexl. A Test Theory of Special Relativity: ii. First Order Tests. *Gen. Rel. Grav.*, 8(7):515, 1977.

[33] R. Mansouri and R.U. Sexl. A Test Theory of Special Relativity: iii. Second-Order Tests. *Gen. Rel. Grav.*, 8(10):809, 1977.

[34] R.J. Kennedy and E.M. Thorndike. Experimental Establishment of the Relativity of Time. *Phys. Rev.*, 42(3):400–418, Nov 1932.

[35] A. A. Penzias and R. W. Wilson. A Measurement of Excess Antenna Temperature at 4080 mc/s. *Astrophysical Journal*, 142:419, 1965.

[36] P. Antonini, M. Okhapkin, E. Göklü, and S. Schiller. Test of constancy of speed of light with rotating cryogenic optical resonators. *Phys. Rev. A*, 71:050101, 2005.

[37] P.L. Stanwix, M.E. Tobar, P. Wolf, C.R. Locke, and E.N. Ivanov. Improved test of Lorentz invariance in electrodynamics using rotating cryogenic sapphire oscillators. *Physical Review D (Particles, Fields, Gravitation, and Cosmology)*, 74(8):081101, 2006.

[38] D. Hils and J.L. Hall. Improved Kennedy-Thorndike experiment to test special relativity. *Phys. Rev. Lett.*, 64(15):1697–1700, Apr 1990.

[39] P. Wolf, M.E. Tobar, S. Bize, A. Clairon, A.N. Luiten, and G. Santarelli. Whispering Gallery Resonators and Tests of Lorentz Invariance. *General Relativity and Gravitation*, 36:2351, 2004.

[40] R. Grieser et al. A test of special relativity with stored lithium ions. *Applied Physics B*, 59:127, 1994.

[41] Peter Wolf and Gérard Petit. Satellite test of special relativity using the global positioning system. *Phys. Rev. A*, 56(6):4405–4409, Dec 1997.

[42] G.C. Branco and V.A. Kostelecký. CP violation in supersymmetric models. *Phys. Rev. D*, 39(7):2075–2078, Apr 1989.

[43] V.A. Kostelecký and R. Potting. CPT and strings. *Nuclear Physics B*, 359(2-3):545 – 570, 1991.

[44] V.A. Kostelecký. Gravity, Lorentz violation, and the standard model. *Phys. Rev. D*, 69(10):105009, May 2004.

[45] Robert Bluhm. *Special Relativity: Will it survive another 101 years?*, volume 702 of *Lecture Notes in Physics*, chapter *Overview of the SME*, page 191. Springer, 2006.

[46] R. Jackiw and V.A. Kostelecký. Radiatively Induced Lorentz and CPT Violation in Electrodynamics. *Phys. Rev. Lett.*, 82(18):3572–3575, May 1999.

[47] S.M. Carroll, G.B. Field, and R. Jackiw. Limits on a Lorentz- and parity-violating modification of electrodynamics. *Phys. Rev. D*, 41(4):1231–1240, Feb 1990.

[48] M. Goldhaber and V. Trimble. Limits on the Chirality of Interstellar and Intergalactic Space. *J. Astrophys. Astr.*, 17:17, 1996.

[49] S.M. Carroll and G.B. Field. Is There Evidence for Cosmic Anisotropy in the Polarization of Distant Radio Sources? *Phys. Rev. Lett.*, 79(13):2394–2397, Sep 1997.

[50] V.A. Kostelecký and M. Mewes. Signals for Lorentz violation in electrodynamics. *Physical Review D*, 66(5):056005, 2002.

[51] V.A. Kostelecký and M. Mewes. Cosmological Constraints on Lorentz Violation in Electrodynamics. *Phys. Rev. Lett.*, 87(25):251304, Nov 2001.

[52] P. Kenneth Seidelmann, editor. *Explanatory Supplement to the Astronomical Almanac*. University Science Books, 2006.

[53] Stefan Ulrich Seel. *Kryogene Optische Resonatoren*. PhD thesis, Universität Konstanz, 1996.

[54] Rainer Kassing, editor. *Bergmann/Schäfer, Lehrbuch der Experimentalphysik, Band 3 - Festkörper*. deGruyter, 2005.

[55] H.B. Callen and R.F. Greene. On a theorem of irreversible thermodynamics. *Phys. Rev.*, 86, 1952.

[56] K. Numata, A. Kemery, and J. Camp. Thermal-noise limit in frequency stabilization of lasers with rigid cavities. *Phys. Rev. Lett.*, 93:250602–1, 2004.

[57] Thomas J. Kane and Robert L. Byer. Monolithic, unidirectional single-mode nd:yag ring laser. *Opt. Lett.*, 10(2):65–67, 1985.

[58] D. Jacob, M. Vallet, F. Bretenaker, A. Le Floch, and M. Oger. Supermirror phase anisotropy measurement. *Opt. Lett.*, 20(7):671–673, 1995.

[59] F. Brandi et al. Measurement of the phase anisotropy of very high reflectivity interferential mirrors. *Appl. Phys. B*, 65:351–355, 1997.

[60] T. Day, E.K. Gustafson, and R.L. Byer. Sub-hertz relative frequency stabilization of two-diode laser-pumped Nd:YAG lasers locked to a Fabry-Perot interferometer. *IEEE J. Quantum Electron.*, 28:1106, 1992.

[61] A.L. Schawlow and C.H. Townes. Infrared and optical masers. *Phys. Rev.*, 112(6):1940–1949, Dec 1958.

[62] R. V. Pound. Electronic frequency stabilization of microwave oscillators. *Review of Scientific Instruments*, 17(11):490–505, 1946.

[63] R.W.P. Drever et al. Laser phase and frequency stabilisation using an optical resonator. *Applied Physics B*, 31:97–105, 1983.

[64] Hans-A. Bachor and Timothy C. Ralph. *A Guide to Experiments in Quantum Optics*. Wiley-VCH, 2004.

[65] Eric D. Black. An introduction to pound-drever-hall laser frequency stabilization. *Am. J. Phy.*, 69(1):79, 2001.

[66] Ch. Salomon, D. Hils, and J. L. Hall. Laser stabilization at the millihertz level. *J. Opt. Soc. Am. B*, 5:1576, 1988.

[67] B. C. Young, F. C. Cruz, W. M. Itano, and J. C. Bergquist. Visible lasers with subhertz linewidths. *Phys. Rev. Lett.*, 82(19):3799–3802, May 1999.

[68] Ch. Eisele, M. Okhapkin, A.Yu. Nevsky, and S. Schiller. A crossed optical cavities apparatus for a precision test of the isotropy of light propagation. *Optics Communications*, 281:1189, 2008.

[69] H. Lutz and W. Wendt. *Taschenbuch der Regelungstechnik*. Verlag Harri Deutsch, 2007.

[70] D.B. Newell et al. An ultra-low-noise, low-frequency, six degrees of freedom active vibration isolator. *Rev. Sci. Instrum.*, 68:3211, 1997.

[71] J.C. Bergquist, W.M. Itano, and D.J. Wineland. Laser stabilization to a single ion. pages 359–376. North Holland, 1994.

[72] D. Muster and R. Plunkett. *Isolation of vibrations*, chapter 13, pages 406–433. McGraw-Hill, 1971.

[73] T. Nazarova, F. Riehle, and U. Sterr. Vibration-insensitive reference cavity for an ultra-narrow-linewidth laser. *Applied Physics B*, 83, 2006.

[74] H. Müller, P.L. Stanwix, M.E. Tobar, E. Ivanov, P. Wolf, S. Herrmann, A. Senger, E. Kovalchuk, and A. Peters. Tests of Relativity by Complementary Rotating Michelson-Morley Experiments. *Physical Review Letters*, 99(5):050401, 2007.

[75] D.B. Sullivan, D.W. Allan, D.A. Howe, and F.L. Walls. Characterization of Clocks and Oscillators. Technical Report NIST/TN-1337, NIST, march 1990.

[76] M. Roberts, P. Taylor, and P. Gill. Laser Linewidth at the Sub-Hertz Level. Technical Report CLM 8, NPL, 1999.

[77] D.W. Allan. Should the classical variance be used as a basic measure in standard metrology? *IEEE Trans. Instr. Meas.*, IM-36:646, 1987.

[78] J. A. Barnes et al. Characterization of frequency stability. *IEEE Trans. Instrum. Meas.*, IM-20:105–120, 1971.

[79] J. Rutman. Characterization of phase and frequency instabilities in precision frequency sources. *Proc. IEEE*, 66:1048–1075, 1978.

[80] William Riley. *Handbook of Frequency Stability Analysis*. Hamilton Technical Services, 2007.

Erklärung

Die hier vorgelegte Dissertation habe ich eigenständig und ohne unerlaubte Hilfe angefertigt. Die Dissertation wurde in der vorgelegten oder in ähnlicher Form noch bei keiner anderen Institution eingereicht. Ich habe bisher keine erfolglosen Promotionsversuche unternommen.

Düsseldorf, den 05.11.2009

(Christian Eisele)